190
10-2-81

37462

①

MASTER

UCRL-50016-81-1

Dr 3025

Mechanical Engineering Department Technical Review

Scientific Editor: R. B. Carr

General Editor: R. M. Denney

January 1, 1981

Lawrence Livermore National Laboratory

UCRL-50016-81-1
Distribution Category UC-38

Mechanical Engineering Department Technical Review

Scientific Editor: R. B. Carr

General Editor: R. M. Denney

Manuscript date: January 1, 1981

DISCLAIMER

LAWRENCE LIVERMORE LABORATORY
University of California • Livermore, California • 94550

Available from: National Technical Information Service • U.S. Department of Commerce
5285 Port Royal Road • Springfield, VA 22161 • $9.00 per copy • (Microfiche $3.50)

PREFACE

The Mechanical Engineering Department Technical Review is published to 1) inform readers of various technical activities within the Department, 2) promote exchange of ideas, and 3) give credit to personnel who are achieving the results.

The report is in two parts: technical achievements and publication abstracts. The first is divided into eight sections, one for each division in the Department.

These technical achievement articles are summaries of ME work. For additional details on a subject, please contact the individual(s) listed at the end of each article. Inasmuch as most projects are the result of the cooperative efforts of many individuals, the article contact(s) may refer you to another individual who can best answer your question.

The second part of the quarterly Technical Review contains the titles and abstracts of laboratory reports authored or coauthored by Mechanical Engineering personnel since the previous issue.

The ME Technical Review Committee members include:

R. B. Carr, Chairman, Department Office
E. W. McCauley, Nuclear Test Engineering Division
[illegible] W. Ravenscroft, Nuclear Explosives Engineering Division
J. H. Pitts, Energy Systems Engineering Division
A. Casamajor, Research Engineering Division
C. W. Clausen, Weapons Engineering Division
C. A. Cordill, Materials Engineering Division
J. D. Lee, Magnetic Fusion Engineering Division
H. H. Hump[illegible] Materials Fabrication Division
R. M. Denney, General Editor

CONTENTS

Nuclear Test Engineering Division

Nuclear Explosives Engineering Division

Weapons Engineering Division

Energy Systems Engineering Division

Research Engineering Division

Materials Engineering Division

Magnetic Fusion Engineering Division

Materials Fabrication Division

NUCLEAR TEST ENGINEERING DIVISION

The Nuclear Test Engineering Division (NTED) provides mechanical engineering and technical expertise to prepare and field nuclear tests and to conduct analytical and experimental studies involving nuclear safety in general and seismic response of reactors in particular. The Division also provides mechanical engineering services for spill effects testing at China Lake and NTS under the Liquefied Gaseous Fuels Program.

Nuclear Testing

Our nuclear testing activities and responsibilities involve the design, structural evaluation, fabrication, and proof testing of diagnostic and device canisters that position radiation detectors and protect nuclear explosives in an underground environment. We emphasize efforts to improve data quality and field operations, optimize cost effectiveness, and maximize safety. We synthesize, procure, and certify the arming and firing systems. The underground diagnostic systems we provide require development and fielding of mechanical equipment and the designing of downhole emplacement systems. We develop containment systems to meet zero-detectable radioactivity release requirements. In addition, our advanced development projects include the development of new diagnostic techniques and field engineering concepts designed to optimize stemming plans and procedures, and development of appropriate design and analysis methods.

Reimbursable Programs for the U.S. NRC

The safety of nuclear power plants and associated facilities is the major concern of the Nuclear Regulatory Commission (NRC). We are responsible for providing sound technical data on which NRC can base licensing decisions and assessment tools to protect public health and safety. In this multidisciplinary effort over the past 6 years we have been engaged in more than 60 separate NRC reimbursable contracts. In our work most of the facilities of the nuclear fuel cycle have been considered from the structural integrity viewpoint, including fuel processing and fabrication, accident analysis (particularly containment systems), interim waste storage, and spent fuel reprocessing. Our work can be grouped into three categories: seismic engineering, applied mechanics, and systems engineering and risk estimation.

A general goal we have is to establish LLNL as a national and international center of seismic excellence. We are currently NRC's lead laboratory concerning seismic safety.

(For further information, contact R. J. Wasley, Ext. 2-9966.)

New Cable Downhole System Proposed for NTS

A new downhole cable emplacement system is now under study and development by the Nuclear Test Engineering Division for underground testing of nuclear devices at the Nevada Test Site (NTS). In the proposed innovative approach to nuclear explosive emplacement and stemming, cables would be supported from the surface without downhole attachments to the emplacement pipe.

Under current test procedure, approximately 150 electronic cables are attached at frequent intervals to the emplacement casing as the nuclear device and associated diagnostic equipment are lowered into a predrilled hole. These cables extend up the length of the hole and out onto the ground surface where they are connected to recording instrumentation. Special materials and procedures are then used to backfill the hole in what is called the stemming operation.

The new system will support the free-hanging weight of the cables from the surface with no attachment to the emplacement casing. Additional loading imposed on the cables during the stemming operation will be automatically released by allowing the cables to be drawn into the hole.

The new support system will consist of an electronically controlled tensioner for each cable. A central control computer will be programmed with the required tension versus depth of burial for each type of cable. Before each nuclear explosive emplacement, the computer operator will provide data on the depth of burial and type of cable in each tensioner. The computer will then monitor the performance of each tensioner.

A feasibility study and a search for qualified manufacturers has been completed, with a request *for quotation released for a 10-cable prototype* system to be fully tested in FY 81. Upon success of the prototype system, a contract will be released to procure a 150-unit system in FY 82.

Implementation of this system will make approximately 4000 man-days available for redirected *effort of technical support personnel for additional* test program work, a saving of about $2 million per year.

(For further information, contact D. J. Ruffner, Ext. 2-1754.)

A Breakthrough: Low-Energy X-Ray Diagnostics on the Tandem Mirror Experiment

In a significant breakthrough for magnetic fusion, the x-ray spectrum has been measured accurately for the first time in the Tandem Mirror Experiment (TMX). This achievement is ascribed to the Double Reflection X-ray Spectrometer (DREXS) in its initial application following completion of design, development, and testing in mid-1980.

Mechanically, DREXS was created by Nuclear Test Engineering Division personnel using physics criteria proposed by L-Division's X-ray Measurements Group, and with the support of the Electronics Engineering Department. The result of this close team effort is a highly unique and flexible instrument. As an exploratory tool, DREXS has extraordinary capability to positively identify and measure x rays in the presence of large and varying types of backgrounds. DREXS has almost unlimited *application possibilities for a variety of* x-ray sources.

Measurements of soft x rays emitted by pulsed sources, such as in TMX, are among the most difficult in physics, particularly for subkilovolt energies. Previous attempts to measure magnetic fusion x rays from TMX in other ways were not successful because of the presence of intense UV, charged particle, and neutron backgrounds. With DREXS, however, the neutron and gamma backgrounds were easily isolated and the x rays *were measured. DREXS can* measure pulsed or constant x-ray source spectra from approximately 0.5 to 8.0 keV, even in the presence of intense backgrounds.

DREX has these unique features:

- The x-ray response is determined by mirror angles.
- It has high efficiency (approx 80%).
- The highly directional measurement is convenient for spatial resolution studies.

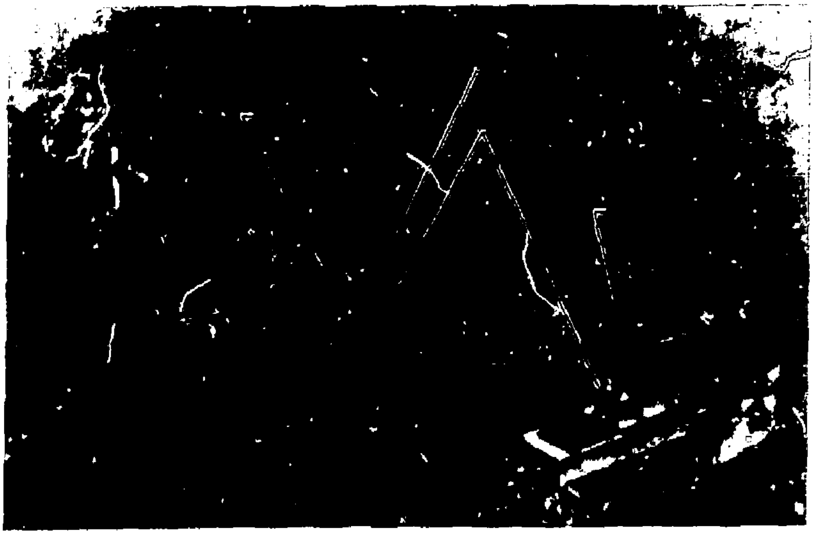

FIG. 1. The Double Reflection X-Ray Spectrometer (DREXS).

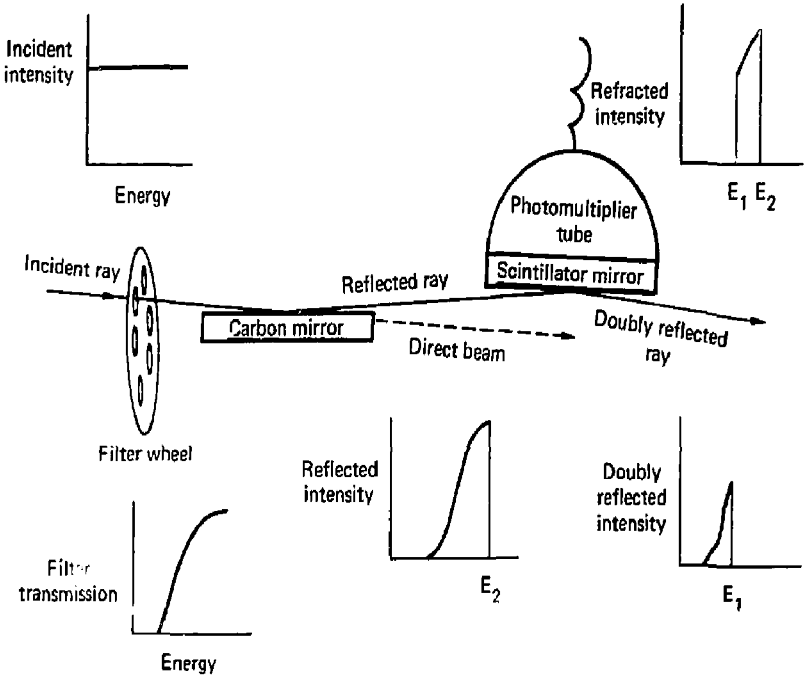

FIG. 2. **A schematic illustration of the spectrometer and its response to a flat incident spectrum at key points within the instrument.**

- It not only measures any x rays (0.5 to 8.0 keV) present, but also decisively identifies them as x rays.
- It has strong background discrimination and measurement.

DREXS is easy to use and requires no advance knowledge of the spectrum to be measured. Additionally, DREXS is lightweight and portable.

A cutaway view of DREXS is shown in Fig. 1, and a schematic illustration of the instrument in operation is presented in Fig. 2. The DREXS concept and theory are described in Ref. 1.

Operation

Incoming x rays accepted by the collimator-slit system pass through a selected filter and thin light barrier to the surface of a highly polished carbon mirror at a grazing-incidence angle. The slit system restricts x rays to the mirror-detector surfaces. X-ray spectra having energies below a particular energy corresponding to the critical angle will be almost totally reflected. The reflectivity for x rays above this energy drops abruptly to nearly zero. X rays are reflected by the carbon mirror out of the direct beam where background is low, and are intercepted by the flat polished surface of a plastic scintillator, optically bonded to a photomultiplier tube. Adjusting the scintillator mirror reflection angle slightly greater than the carbon mirror angle refracts a narrow selectable energy band out of the incident spectrum into the scintillator to produce light, resulting in electrical current from the photomultiplier tube. The desired bandwidth to be measured is controlled by appropriate angular adjustment of the carbon mirror (upper energy cut) and scintillator mirror (lower energy cut). A filter selected from an internal, 8-position filter wheel may be used to reduce any contribution from the low-energy tail. The limit of resolution is set by the sharpness of the upper and lower band edges, which is about 0.1 keV.

The carbon mirror and detector are mounted on separate rotation stages. The detector rotation stage rides on a translation stage to maintain proper

$\theta - 2\theta$ geometry for various settings of the carbon mirror angle. In addition, this translation stage can serve to move the detector in and out of the x-ray beam for purposes of background determinations. The rotation stages, translation stage, and filter wheel are remotely controlled, manually operated. Future plans are to use microprocessors for automated control.

Mechanical

Because of our intention to use DREXS at many different source facilities, some of the design choices were compromises required for maximum versatility. The package was made as small and light as possible for easy handling and shipping, and yet sturdy enough to maintain the extremely precise alignment of internal components. Approximate dimensions of the overall package are 10 by 18 in. by 5 ft. It weighs 150 lb

We chose a 2-ft spacing between the x-ray slits to permit ample neutron and gamma collimation, which is slightly oversized relative to the x-ray slits in this region. We also chose 2-ft spacing between the carbon mirror and detector to minimize the effects of scattering from the carbon mirror and to enable the scintillator mirror to be positioned outside the direct beam of gammas and neutrons, even with the carbon mirror set at very grazing angles. High-flux, permanent magnets were mounted immediately behind the carbon mirror to prevent charged particles, particularly electrons, from reaching the scintillator detector.

For descriptive purposes, the spectrometer may be broken into three parts, each having its own function. First is the front end that conditions the incoming beam. Second is the rail assembly that measures that conditioned beam. Third is the housing that ties the front end and rail assembly into one unit and provides a vacuum environment.

The front end (Fig. 3) contains x-ray defining slits, a neutron and gamma collimator, x-ray filters, and a vacuum light barrier. Unique parts of the front end are a remotely controlled, 8-position filter wheel directly rotated by a Klinger RD57 stepper

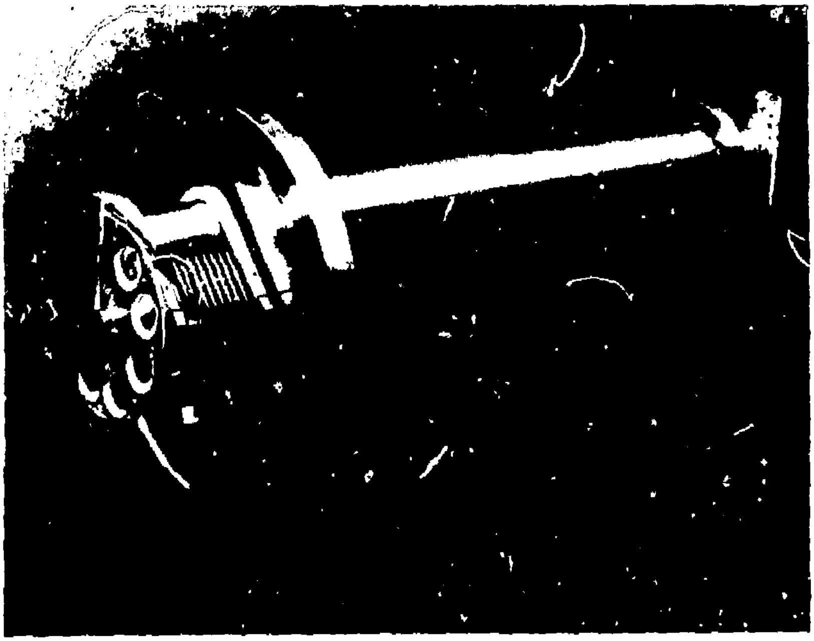

FIG. 3. Front end assembly showing filter wheel and four-position slit assemblies. A copper gamma/neutron collimator fits snugly inside the tubing between the slits.

motor and a pair of 4-position x-ray slits. Desired slit size can be selected externally by positioning two vacuum feedthroughs.

To precisely position the two mirrors for the double reflection of the x rays, the rail assembly (Fig. 4) incorporates three remotely controlled Klinger stages. Both of the mirrors are mounted on rotation stages and can be set to ±0.01° of desired angle. The second mirror with its rotation stage is mounted on a translation stage that moves it to the precise location for intercepting the reflected x rays off the first mirror.

The housing (Fig. 5) is of lightweight construction and has an external strongarm that provides alignment stability between the front end and the rail assembly.

Figure 6 shows DREXS mounted on the TMX.

DREXS has unlimited uses as an exploratory tool for many facilities. Because we now know that DREXS tells a user exactly what he needs to do a job, we foresee significant contributions by DREXS in investigations of low-energy x-ray sources. Once DREXS measures the x-ray spectrum, the information could be used to design a multichannel spectrometer especially suited for that particular facility.

(For further information, contact R. Crabb, Ext. 2-1281, G. A. Burginyon, Ext. 2-1060, J. P. Stoering, Ext. 2-1076, or M. E. McGee, Ext. 2-1253.)

In Situ, Transient Measurement of Relative Permeability Under Study

Relative permeability is an empirical parameter. Its value is used to predict simultaneous flow of immiscible fluids in a porous medium. Local *relative permeability of a porous medium* is determined in the laboratory from core samples. Field

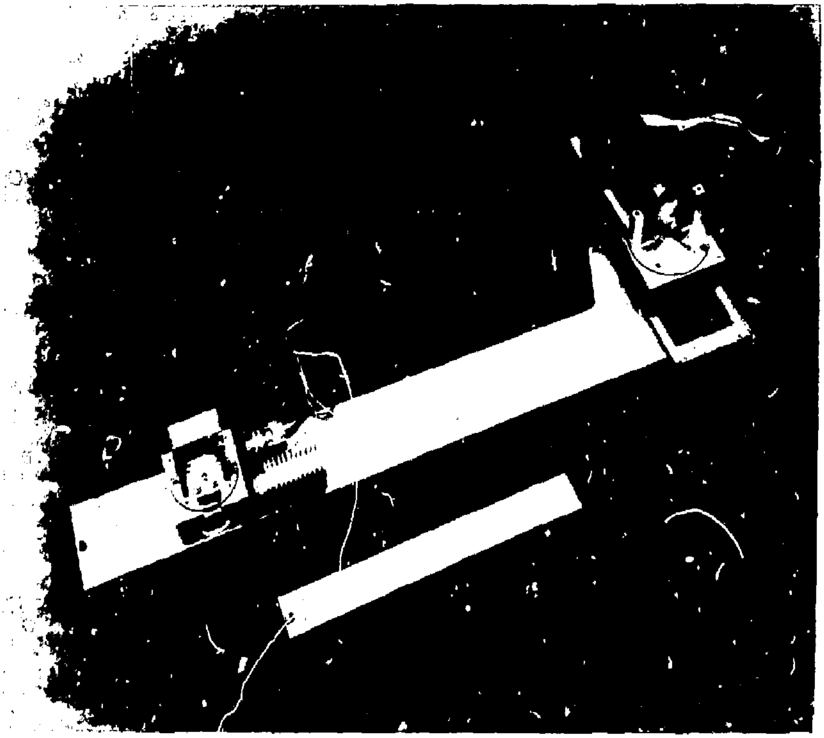

FIG. 4. The rail assembly incorporates three electronically controlled positioners that precisely position the two mirrors for the double reflection of the x rays.

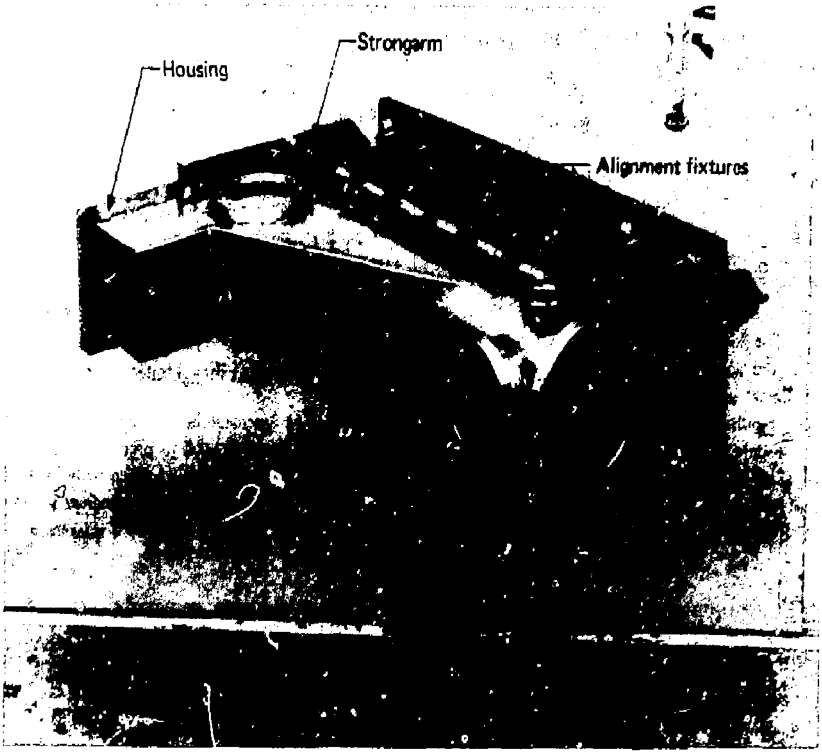

FIG. 5. The housing, strongarm, and three-axis alignment fixtures.

determinations are restricted to global values estimated to match measured reservoir output.

The mechanical nature of coring produces disturbed samples. Because relative permeability is usually not measured in the field or with the field core, laboratory determinations are made with cores cut from the disturbed sample that, of necessity, has been handled several more times after removal from its natural environment. Specifically, the field core is carefully removed from the coring tool, stored for transportation, to the laboratory, jostled during transportation, removed from the vehicle for storage in the laboratory, removed from storage to prepare samples, and finally mounted in the test fixture before measurements can be made. The necessity for multiple handling increases the probability of additional alterations of the structure of the test core from its original state. Measurements may be made in a field laboratory, but this method only removes two of the possible disturbances.

By contrast, *in situ* measurement is subjected only to disturbances during preparation of the porous medium and during mounting of the measuring instrument. However, measurements are difficult to interpret, especially if the medium is heterogeneous and/or layered. A study has been initiated to develop an *in situ* method applicable to the determination of relative permeability of geological formations and to delimit attainable accuracy with the method. This will be a combined analytical/experimental study of two-phase immiscible fluid flow in a porous medium.

The relative permeability will be calculated from measured pressure history by computer simulation. Experiments will be conducted in a controlled laboratory environment. Various mixes of sand consolidated in a 6-ft-diam by 8-ft-high tank

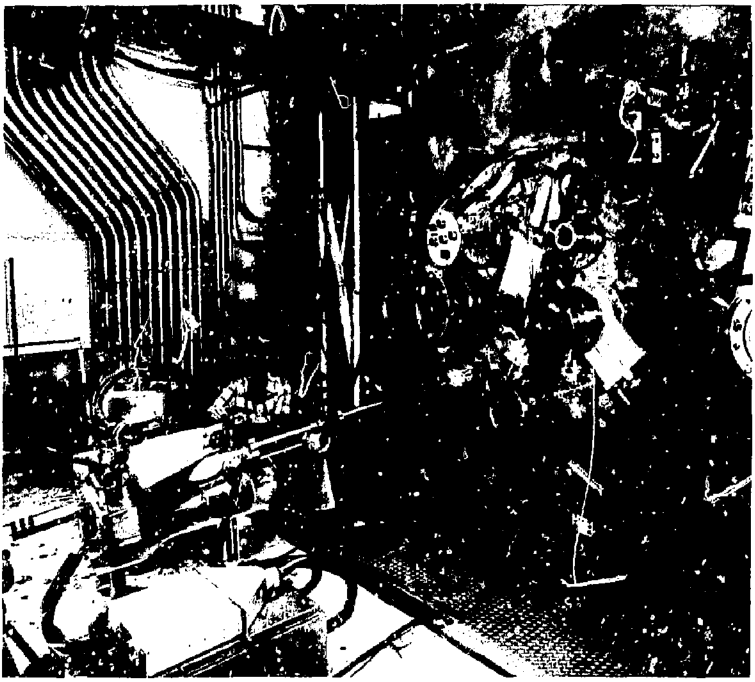

FIG. 6. **Richard Crabb makes slit adjustments to DREXS, which is connected to the east end of the Tandem Mirror Experiment (TMX) at right.**

will be the porous media. Known quantities of fluid will be injected into the sand bed for a predetermined period by means of a specially designed instrument; this instrument will also contain pressure transducers.

(For further information, contact W. Lai, Ext. 2-0324.)

Seismic Safety Margins Research Program Started

The Seismic Safety Margins Research Program (SSMRP) is a multiyear comprehensive research program to develop improved methodology for seismic analysis and design (Fig. 7). This summary concerns the Best Estimate method versus the Evaluation Method investigation conducted as part of the SSMRP.

The objectives of the SSMRP are to:

- Estimate the degree of conservatism or unconservatism in the Nuclear Regulatory Commission's seismic safety requirements of the Standard Review Plan (SRP) required on all new plants.
- Develop improved requirements and methods for safety assessment.

The approach toward achieving program objectives is to develop a probabilistic methodology that more realistically estimates the behavior of nuclear power plants during an earthquake. This methodology will be tested against experimental data whenever possible.

Program Overview

For some time there has been a strong motivation to reexamine the traditional process of seismic analysis in a system context. This motivation arises

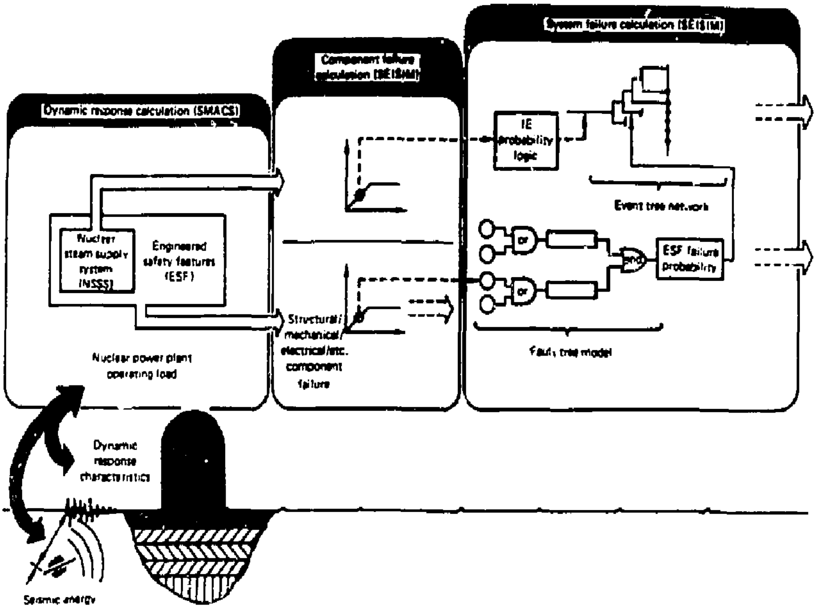

FIG. 7. An abbreviated representation of the primary elements and areas of interest in the Seismic Safety Margins Research Program shows conceptually how they are broken down for analysis.

principally from a widely held belief that conservatisms compound in current practice. That is, at each stage, conservatisms are introduced to account for uncertainties, and these conservatisms compound from one stage to the next. Presently, only minimal compensations for compounding are made in each stage because the conservatisms are not quantified. The result may be an overly conservative seismic design, which, in addition to adding cost, could also be unconservative on a systems basis.

A methodology to examine the current seismic analysis and design process of nuclear power plants in a system context has been developed in the SSMRP. Clearly, examining the total plant, including the functional capabilities of operating and safety systems and their interdependence, is the most complete manner of addressing the various issues—this examination is the SSMRP approach. Figure 8 depicts the Seismic Methodology Chain (SMC) and its relationship to the SSMRP system analysis model. The SMC is separated from the SSMRP system analysis model by a segmented line to emphasize that, in the SSMRP, the analysis is performed in two parts. The systems analysis (below the dashed line) represents reactor systems using event-tree/fault-tree model and also employs a computational procedure to compute the probability of failure of structures, components, and systems, the probability of radioactive release (risk), and variations in these probabilities due to uncertainties in the SMC and other models. (The LLNL-developed SEISIM code is used for these computations.) However, with SSMRP methodology it is possible to perform analyses considering only the four elements of the SMC:

- Seismic input.
- Soil-structure interaction.
- Major structure response.
- Subsystem response, for example, for piping subsystems.

The subsystem response is applied in a coupled or "system" fashion (the LLNL-developed SMACS code is used for these computations), independently of the calculation of probabilities of failure or release. The quantities of interest are then response parameters and their statistics; for example, in-structure response spectra, displacements,

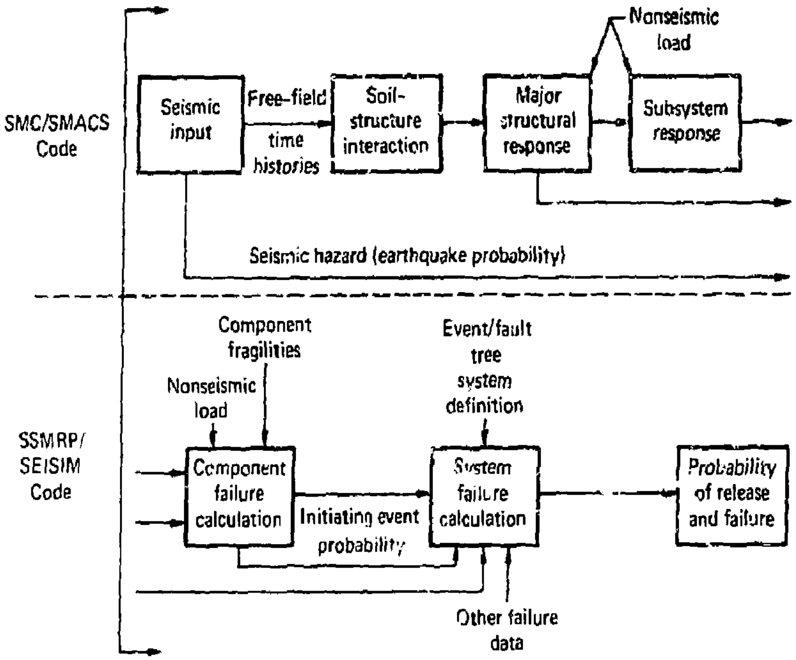

FIG. 8. Key elements of a seismic analysis calculational procedure for nuclear power plants.

velocities, accelerations, and forces, rather than probabilities of failure or radioactive release.

Best Estimate Method Versus Evaluation Method Concept

In the Best Estimate method versus Evaluation Method procedure the systematic evaluation of the seismic analysis and design of a nuclear power plant is simplified to encompass only the four links of the SMC (see Fig. 9).

The objective of this process is to compare two seismic analysis procedures. One comparison could be between a Best Estimate (BE) method and an Evaluation Method (EM) for seismic (S) analysis and design. However, comparisons are not limited to BE versus EM; any two methodologies may be compared. Examples include any combination of best estimate, design methodologies used for older plants, proposed new techniques, erroneous methods of analysis, and so forth. We emphasize three key points in the BE-EM concept:

- The methodology comparison should include as many links of the SMC as possible and appropriate.
- The basis of comparison will be probabilistic, that is, mean versus mean, mean versus mean-plus-one-standard deviation, and so forth.
- The plurality of the term BE-EM is quite suggestive of the state of the art, in that a single validated BE method does not yet exist. Therefore, many different BE-EM comparisons are possible.

Conclusions

We conclude that the BE-EM concept can provide valuable insights on seismic analysis and design for nuclear power plants and, when fully implemented, will provide good estimates of certain aspects of the calculational portion of seismic "conservatisms or margins." Work is presently under way to develop the scope of more comprehensive research efforts.

Further information on the BE-EM study can be found in a detailed technical report.[3]

(For further information, contact R. D. Bailey, Ext. 2-0321.)

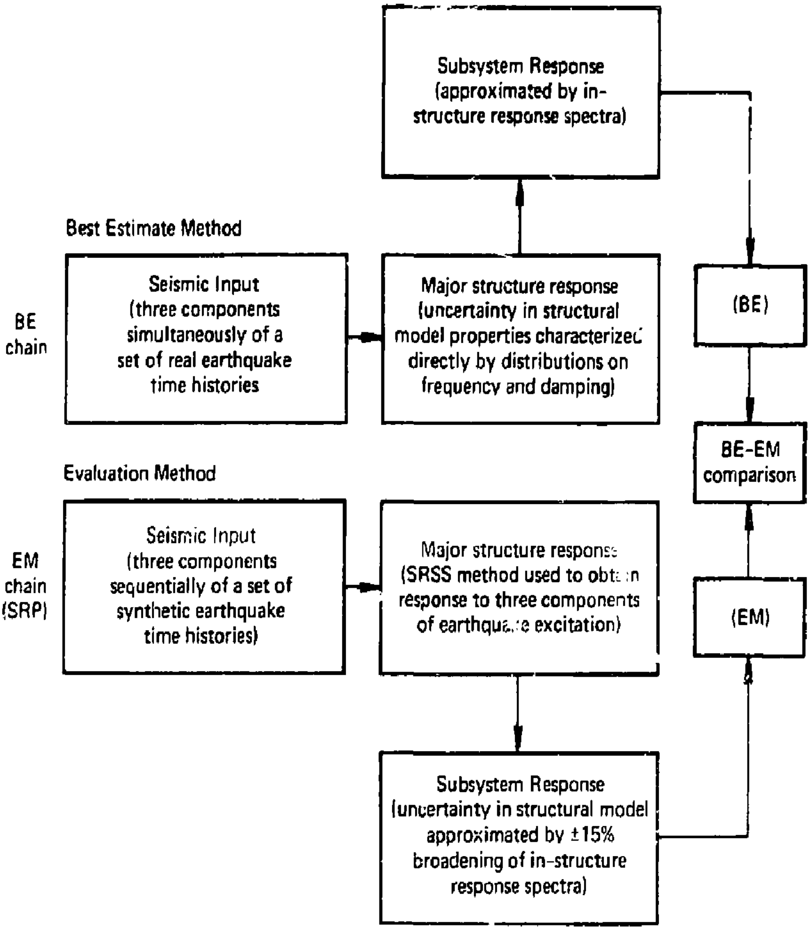

FIG. 9. Overview of the Best Estimate versus Evaluation Method used to develop summary results.

Physical Model of Chugging Phenomena During the Loss-of-Coolant Accident in a Nuclear Power Reactor

Using the results of large-scale multivent tests conducted by the GKSS Research Center in West Germany, we have developed a physical model of chugging. A unique combination of accurate digital and cinematic data has allowed a detailed, quantified correlation between the dynamic physical variables and the associated two-phase thermohydraulic phenomena occurring during lean suppression (chugging) phases of the loss-of-coolant accident (LOCA) in a boiling water reactor pressure-suppression system (PSS).

Although the principle of pressure-suppression system function is simple, the resultant transient phenomena exhibit complex components that give rise to significant impulsive loading in the wetwell. These components are difficult to quantify but are important to safe design.

Past studies have identified numerous pressure-suppression phenomena that accompany the quasi-steady-state pressure and temperature rise in the PSS wetwell during a hypothetical LOCA. The transition from initiation of break flow to completion of blowdown is accomplished in three consecutive stages as shown in the plot of pool bottom pressure in Fig. 10. These stages are as follows:

- Clearing of the initial water leg in the vent pipes by steam-driven wetwell air, resulting in a single strong impulsive loading cycle on the pool boundary, coupled with a strong pool swell as the noncondensible drywell air creates a large subpool bubble at each vent exit followed by an *air-rich flow* period.
- An extended period of quasi-steady-state steam condensation, termed *condensation oscillation* (CO), which is periodic and accompanied by regular pressure variations on the pool boundaries.
- Lean suppression or *chugging*, which occurs under conditions of low air content and depleted steam flow and which gives rise to strong, impulsive pressure transients of variable magnitude. Because of the strong and cyclic nature of this *chugging stage, its quantification is of considerable* importance to safe containment design.

A multivent test facility, located at the GKSS *Laboratory near Hamburg*, West Germany, was placed in operation in February 1979. It provides a three-pipe full-scale vent system (see Fig. 11) modeling main features of both the West German KWU and the United States G.E. MK II BWR pressure-suppression systems. The time-correlated measurements system consists of 128 low speed (25 Hz) and 60 pulse code modulation (1.7 kHz) measurement channels, three 50-Hz television cameras that view both the water surface regions and vent pipe outlets in the wetwell, and a high speed (1000 fps) 16-mm camera that observes a single vent pipe outlet.

Model Development

The work reported here is based on the study of *several GKSS multivent tests and is quantified by* the results of a particular test (M2) conducted at defined standard initial conditions. This work is based on results from a currently active test program and, therefore, is of a preliminary nature and is expected to be expanded.

The GKSS test results to date consistently indicate a strong coupling among dynamic events throughout the entire experimental facility. Thus, if the event time of the chug in Fig. 12 is compared to a sequence of chug events (Fig. 13), a corresponding *similar dynamic event can be located at the same* time even though the pool bottom transducers are respectively located directly beneath a vent pipe and in one corner of the wetwell. This coupling is further illustrated by the close correspondence of the

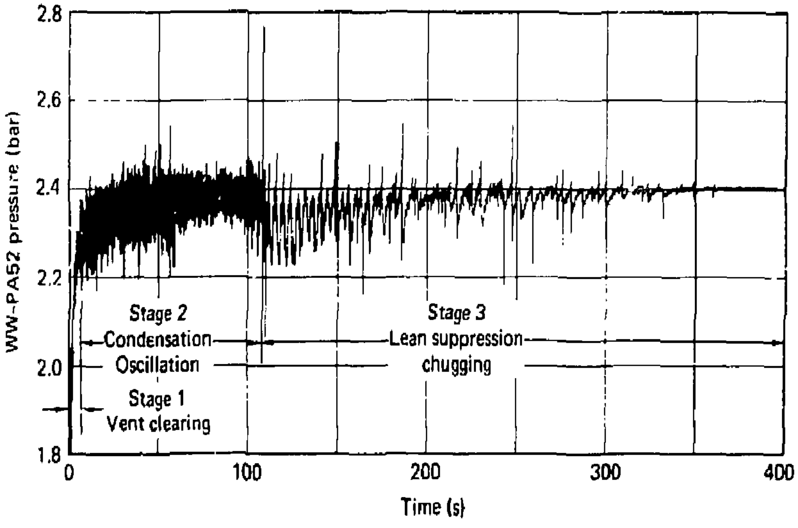

FIG. 10. Stages of response during the LOCA simulation.

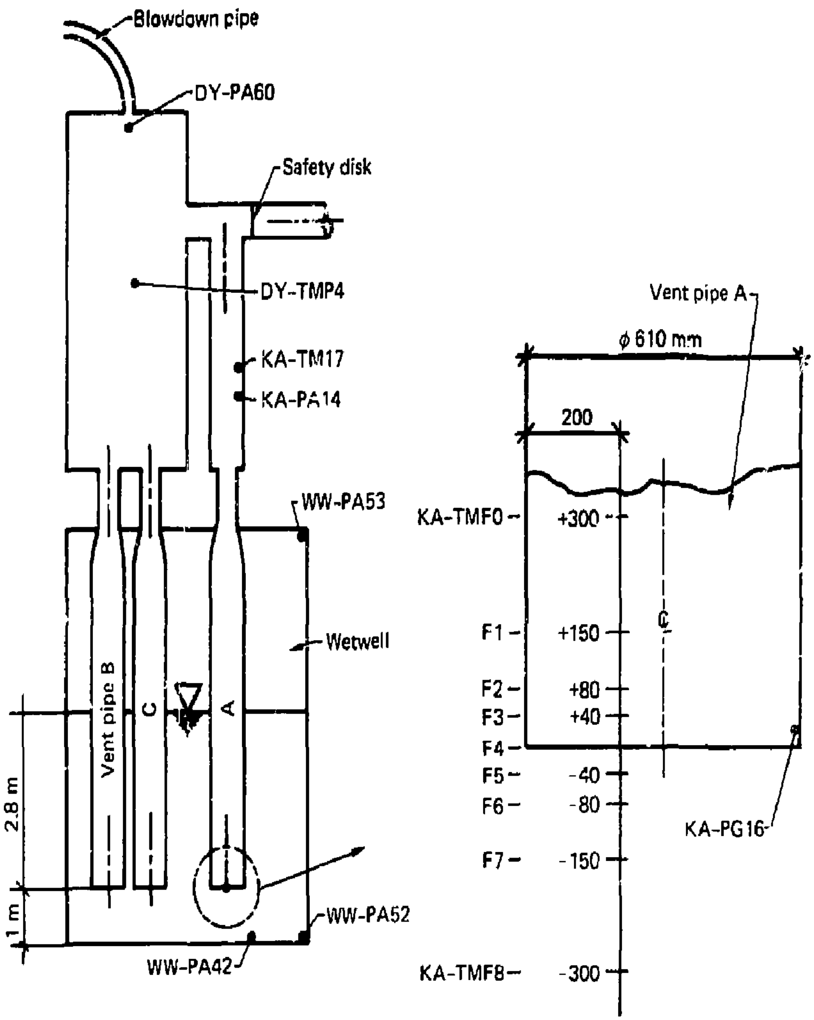

FIG. 11. Schematic of GKSS multivent test facility and selected transducer locations.

pressure behavior in the drywell with that observed in the wetwell.

This coupling of dynamic events is important for a number of reasons:

- It implies that the behavior of the three vent pipes is synchronous. Therefore, the dynamic character of transducer measurements and visual observations made at any vent pipe may be considered qualitatively representative of the behavior at all three vent pipes.
- It implies that the chugging *process* is not significantly dependent on the facility. The previously discussed correlation between pool bottom transducers in Figs. 12 and 13 aids in illustrating this point. Despite the fact that one transducer is located in a corner of the wetwell

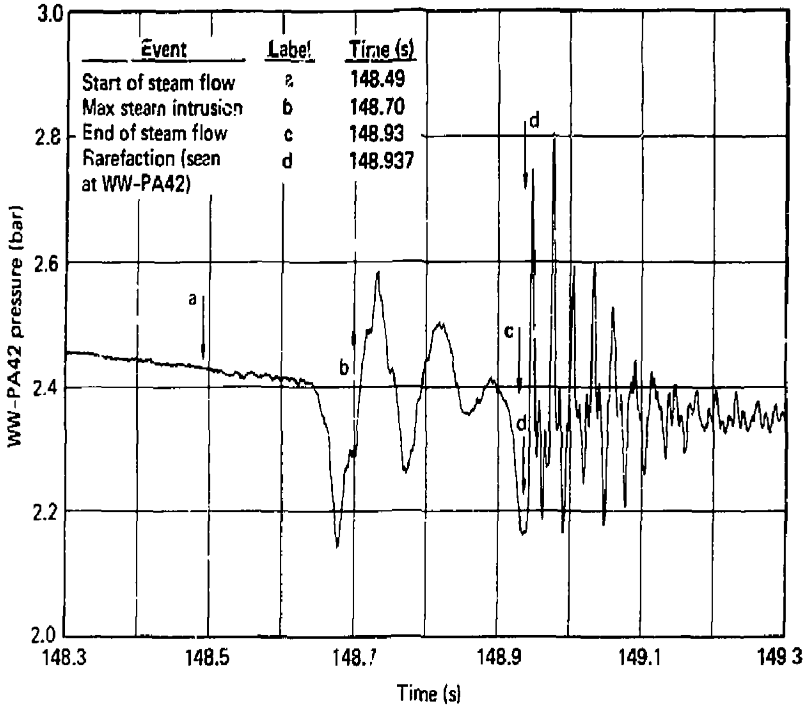

FIG. 12. Detail of lean suppression condensation event correlates the below-vent pressure response with observed steam flow.

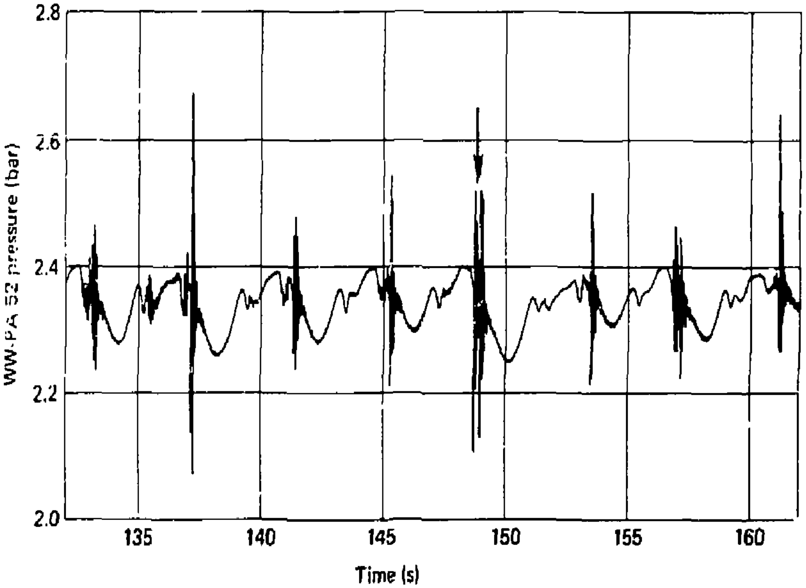

FIG. 13. Typical chug-mode pressure response in wetwell corner.

(where structural influences on the pressure measurements could be expected to be greatest) and the other directly beneath a vent pipe, both show essentially the same dynamic behavior.

- It implies that a pool bottom transducer directly beneath a vent pipe (e.g., WW-PA42) may be used with confidence to correlate numerical data with visual observations at the vent exit.

Data Selected for Correlation. As shown schematically in Fig. 11, the data selected to study the correlation of dynamic events in the GKSS tests covers measurements made from the drywell to the wetwell, i.e., from "source" to "sink." In this manner, coupled input and output conditions can be used to verify analytical models.

Discussion of Results

In the GKSS-PSS tests to date, we have observed a consistent and close coupling of events throughout the drywell, wetwell, and vent pipes as well as a strong correlation between physical and high-speed visual data obtained from the tests. Using these results, we provide a model of the lean suppression process with these features:

- The lean suppression (chugging) events evidence a strong positive pressure peak followed by a high-frequency ringdown characteristic of the natural frequency of the submerged wetwell fluid/structure system.
- This ringdown is preceded by a strong, facility-independent rarefaction that is correlated to the formation and rapid collapse of the steam ring that forms in the vent exit at the end of steam flow.
- A period of lower frequency oscillations precedes the chug rarefaction and corresponds to the acoustic frequency of the particular vent pipe.
- Evidence collected from temperature transducers and high-speed film suggests the steam plume, which penetrates into the pool prior to chug initiation, is partially hollow, thereby allowing a momentary chilling transient to trigger or initiate the acoustic wave. The collapse of such a hollow-core plume could conceivably give rise to the steam ring formed inside the vent exit.

Of particular interest in our observations is that the collapse of the steam ring, which initiates the strongest hydrodynamic loads, occurs well *after* the time of maximum steam penetration into the pool. This observation argues against the more traditional concept of a steam "bubble" at the vent exit.

This initial investigation of the GKSS-PSS multivent tests has documented the consistent correlation between physical and visual data observed and provides a new and useful basis for further development of advanced computer models to address the lean suppression process in a LOCA. Further work is in progress.

(For further information, contact E. W. McCauley, Ext. 2-9947, or G. S. Holman, Ext. 2-9946.)

Study Completed for Hydrogen Monitoring Systems in Reactor Safety Assessment

Monitoring for the presence of hydrogen in the secondary containment vessel of a nuclear power plant during postulated accidents is a recognized requirement to mitigate potential explosions. Commercially available and laboratory-proved methods were surveyed for the Nuclear Regulatory Commission. The primary objective of this study was to identify commercial sources for hydrogen-monitoring devices and to recommend a suitable system for automatic remote monitoring in the secondary containment vessel of a nuclear power plant during a postulated fault condition.

Although more than 20 proved methods are discussed, only five detector types have been marketed and judged suitable for consideration. Even fewer have been qualified for monitoring in nuclear power plants. The five available types group into the following classes:

- Combustion.
- Solid state.
- Electrochemical.
- Thermal conductivity.
- Absorption.

All of the available types are adequate for early-warning systems.

The five classes of commercial detectors require proof-testing when subjected to an atmosphere containing four components—air, steam, hydrogen, and radioactive noncondensibles—that would be released during the postulated conditions. Twelve percent hydrogen by volume is the maximum concentration to be quantified for initiation of the mitigation procedure. Electrochemical detectors, thermal conductivity analyzers, and absorption detectors can sense to and beyond this concentration. Catalytic combustion detectors can quantify up to approximately 7% hydrogen and may change calibration when exposed to nuclear radiation; oxygen is also required for combustion detectors so that mitigation procedures that reduce the oxygen content will interfere with their operation. The upper limit for solid-state detectors is about 10%, but their calibration may change when subjected to nuclear radiation and/or moisture. Electrochemical detectors are subject to "drowning" in a moist atmosphere and may change calibration when exposed to nuclear radiation. Wire-filament-type thermal conductivity analyzers seem best suited for the postulated conditions. However, thermal conductivity analyzers detect by comparison test with a reference gas. The logical reference gas is air, so that the hydrogen must be sensed in a mixture containing steam and radioactive noncondensibles; specificity of the detector under these conditions must be investigated. A detector with high specificity can accurately measure concentration in the presence of diluents.

The following actions are recommended as a result of this study.

Detection Device

- Investigate the effect of nuclear radiation and steam on the performance characteristics of catalytic combustion, solid state, and electrochemical detectors.
- Investigate the effect of steam on the performance characteristics of metallic filament thermal conductivity detectors.
- Investigate the effect of temperature on the performance characteristics of the absorption detector

Sensor or Sniffer Array

- Survey nuclear power plants to establish classes of secondary containment vessel geometries.
- Survey array geometries used to monitor hydrogen leaks in space simulation chambers and off-shore oil platforms.
- Develop a computer model to predict hydrogen concentration with the secondary containment vessel.
- Verify computer predictions with experiments using detector arrays under simulated conditions.

(For further information, contact W. Lai, Ext. 2-0324.)

Thermal Effects of Annular Air Gaps Surrounding an Emplaced Nuclear Waste Canister in Deep Geologic Storage

Containing and isolating nuclear waste material from man and his environment until its radioactivity has decayed to a harmless level is the aim of nuclear waste management. Commensurate with this, programs sponsored by the Nuclear Regulatory Commission are designed to develop and organize knowledge pertaining to the dynamics associated with the management and ultimate disposal of waste materials. The knowledge gained through such programs must form the basis for written guidelines and regulations for use in licensing other organizations/agencies to dispose of nuclear waste in such a manner that the health and safety of the public is assured.

This report documents findings determined through a three-dimensional numerical analysis of the thermal effects of an air gap around a nuclear waste canister emplaced in a deep geologic repository. Particular emphasis is placed on quantitative assessment of the temperature of a waste canister in response to variations of several parameters, which are:

- The surface properties of the gap.
- The size of the annular air gap.
- The presence/absence of a sleeve.
- The canister and areal initial thermal power levels.

Physical Characteristics of the Conceptual Repository

Most of this analysis addresses a repository mined in bedded salt. However, basalt was also modeled so that some determination of host rock and air gap interaction could be quantified. The thermal sources were modeled to have the characteristics of spent fuel aged from 3 to 10 yr before emplacement.

A conceptual model of a spent fuel nuclear waste repository is illustrated in Fig. 14. It consists of a series of long parallel corridors mined in a layer of rock. The size of the corridors will ultimately be determined by the final design of waste handling equipment. The modeling analysis performed here assumes a cross section of 18 by 18 ft (5.49 by 5.49 m). Waste canisters are emplaced in drilled holes equally spaced 17.3 ft (5.27 m) apart along the floor centerline. The rooms were modeled 88 ft (26.82 m) center-to-center. Following emplacement, a plug is inserted atop the canister and the cavity above the plug is filled to floor level. The top of the canister is 10 ft (3.05 m) below the floor level.

Unit Cell and Host Rock Properties

The assumption of simultaneous emplacement of the waste canisters in a uniformly spaced horizontal plane leads to the modeling simplicity of a unit cell containing one waste canister.

Figure 15 illustrates the unit cell, which is identical to that employed by Altenbach[3] and Davis.[4] For the purpose of analyzing the air gap effects, the time period of interest was 0 to 2 yr because peaking of the canister temperature occurred within that modeled time frame.

Numerical Modeling Results

In the absence of specific regulatory direction, it is possible that wide variations will occur in surface properties of the waste canister as well as the size of air gaps surrounding the canister. The potential effects of such variations are detailed in this summary.

Effect of Air Gap Size. The sensitivity of the waste canister temperature to air gap size was evaluated by using the three-dimensional TRUMP numerical code Time-dependent temperature distributions for air gaps of various widths were determined.

The size of the air gap has a dramatic effect on the temperature response of the waste canister, especially when the initial thermal power generation rate is high. The peak canister temperature is plotted in Fig. 16 as a function of gap size for the same three different initial power levels. The trend is the same regardless of the magnitude of the power level: as the gap size increases from zero gap, the temperature rapidly approaches a peak at the critical width of approximately 1 in. (2.5 cm) in all cases. Beyond this width, larger gaps produce lower temperatures.

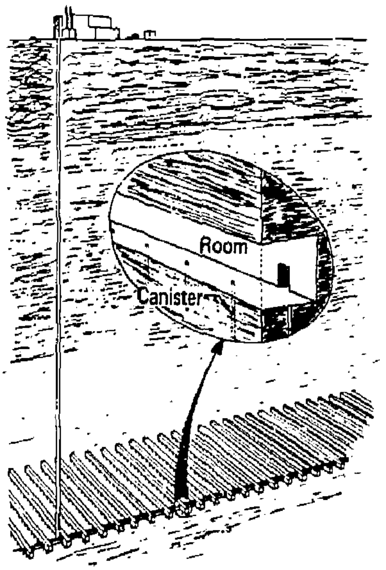

FIG. 14. Conceptual model of a nuclear high-level waste repository in salt.

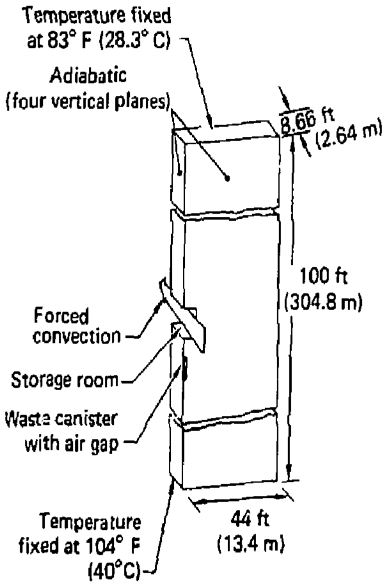

FIG. 15. Quarter-symmetry three-dimensional unit cell utilized in air gap analysis.

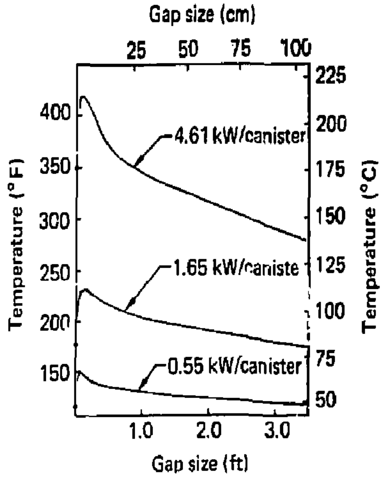

FIG. 16. **Larger thermal power levels produce conditions that result in greater canister temperature sensitivity to air gap size. The emissivities of the gap surface were modeled as *0.9*.**

Effects of Surface Emissivity. *The* thermal resistance to radiation heat exchange between two diffuse surfaces is given by

$$R_{rad} = \frac{1-\epsilon_1}{\epsilon_1 A_1} + \frac{1}{A_1 F_{12}} + \frac{1-\epsilon_2}{\epsilon_2 A_2} \; , \tag{1}$$

where ϵ is the surface's spectral emissivity, A is surface area, and F_{12} corresponds to the view factor between surfaces 1 and 2. The first and last terms are surface resistances and the middle term is a space resistance which is a function only of the heat exchange system. The canister surface and the host rock surface (or drill hole surface) comprise the two surfaces of primary interest. It is possible that these *heat exchange surfaces could have an emissivity* as low as 0.1.[5] A comparison through Eq. (1) shows that the radiation heat exchange resistance will be more than one order of magnitude greater if the emissivity is 0.1 instead of 0.8.

Interactive effects on the canister surface's peak temperature of initial power generation rate and surface emissivities are illustrated in Fig. 17. The repository geometry was identically modeled for all three power levels (in each case the gap size was 3 in.). The emissivity is more influential at higher power levels.

Influence of a Sleeve on the Temperature Response of the Canister. A steel sleeve placed in the radial middle of a 6-in. (15.2 cm) annular air space will cause a dramatic temperature increase in the canister surface. The magnitude of the increase is highly sensitive to the surface emissivities.

The responses indicate that insertion of a sleeve into a 6-in. (15.2 cm) air gap will result in the surface temperature of the canister peaking more than 80°F (44.4°C) higher than it would without a sleeve (all surfaces were modeled with $\epsilon = 0.4$). Similarly, *the canister surface temperature will* peak 40°F (22.2°C) higher when all surface emissivities are 0.9. Both cases had thermal sources of 1.65 kW/canister initial power.

The cause of such a dramatic increase in temperature of the canister is explained by considering Eq. (1), which defines the resistance of a single air gap. The insertion of a sleeve partitions one 6-in. (15.2 cm) air gap into two 3-in. (7.6 cm) air gaps. The heat rejection path from the canister surface to the host rock is, consequently, through two series resistances instead of a single air space resistance. The end result is that of approximately doubling the *thermal radiation resistance across the 6-in.* (15.2 cm) space. A similar doubling effect on the convection heat transfer resistance also occurs.

Influence of Host Rock Property. The magnitude of air gap effects depends greatly on host rock properties—particularly on thermal conductivity. The scope of this current *effort addressed*

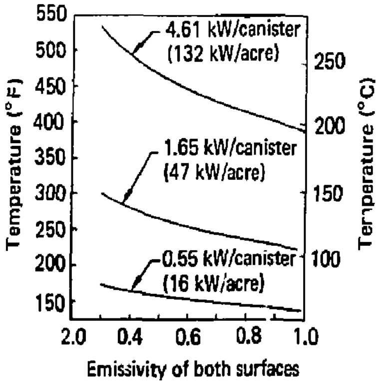

FIG. 17. **The surface emissivity affects the canister temperature at all power levels, but has the greatest influence at higher levels. The gap size for this case is 3 in. (7.6 cm).**

only bedded salt in detail; however, one specific case involving basalt was modeled to illustrate how much more important air gap effects are if repository sites are chosen in media less conductive than bedded salt.

The peak canister surface temperature is plotted as a function of air gap sizes for basalt and salt in Fig. 18. Compared with salt, the temperature drops dramatically in basalt with increasing air gap sizes. The power level for this comparison is relatively low (1.65 kW/canister or 47 kW/acre). Effects at higher power levels would be even more dramatic.

Regulatory Considerations

NRC guidelines should require the licensee to ensure that his proposed design will prevent the canister surface temperature from exceeding a specified maximum. In light of modeling results presented in this report the guidelines should require assurance on the part of the licensee that air gaps and gap surface properties have been considered in design detail. To achieve a thermally desirable emplacement package design, several characteristics should be considered. Gap sizes on the order of 1 in. (2.54 cm) should be avoided. It is recommended that the spectral emissivity for the canister surface be in the range of 0.8 or greater. As a consequence of the negative thermal effects shown to result from a retaining sleeve, it is recommended that the use of a loosely inserted sleeve should be precluded in the absence of outweighing advantages to structural or retrievability considerations. All of these results become more important if the initial thermal generation rate is high.

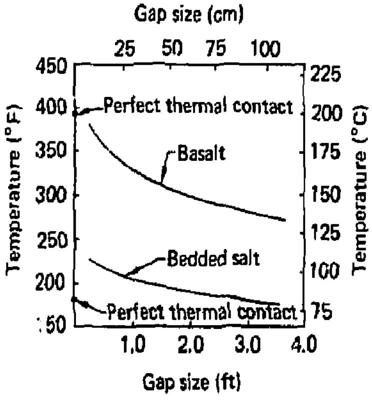

FIG. 18. Effect of air gap size is much more significant if the repository host rock is a poor thermal conductor like basalt. Plotted here are results for both salt and basalt over a range of gap sizes. Surface emissivities were set at 0.9.

(For further information, contact W. E. Lowry, Ext. 2-0270, or H. Cheung, Ext. 2-9952.)

Three-Dimensional Thermal Analysis of a Baseline Spent-Fuel Repository

The Lawrence Livermore National Laboratory is under contract to the U.S. Nuclear Regulatory Commission to provide "Technical Support in the Development of Nuclear Waste Management Criteria." In the Waste Management Program, we are concerned with the performance of spent fuel emplaced in a geologic repository. An important element of spent-fuel performance is the thermal behavior of the spent fuel, package, and nearby geologic medium. This summary describes a three-dimensional thermal model of a spent-fuel repository, and presents preliminary results from the analysis of a baseline repository in salt.[6]

The purpose of our thermal modeling is to calculate the time-dependent near-field temperatures in the repository. This temperature field is essential to predict performance of the waste form and package. The information is used directly as input to other performance models, such as structural response, brine migration, package corrosion, and waste form dissolution.

A baseline design incorporates previous thermal modeling experience and Office of Waste Isolation recommendations for areal thermal loading in specifying the waste form properties, package details, and emplacement configuration (Fig. 19). The base case in this thermal analysis considers one 10-yr-old, pressurized water reactor spent-fuel assembly emplaced to yield a 36 kW/acre (8.9 W/m^2) loading. A unit cell model in an infinite array is used to simplify the problem and provide upper-bound temperatures. Boundary conditions are imposed that allow simulations to 1000 yr. The TRUMP finite-difference heat transfer code was used for the analysis.

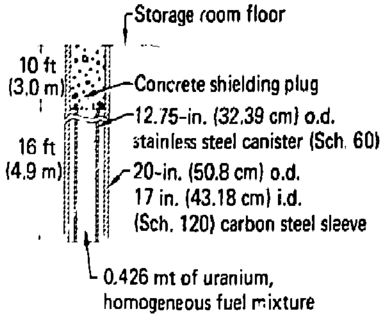

FIG. 19. Emplacement package details modeled as the baseline design.

The model was used to study three areas of concern:

- Thermal response of the canister with and without an annular air gap between the canister and sleeve.
- Comparison of ventilated vs nonventilated storage room conditions.
- Room cooldown responses, with ventilation following an unventilated state, for retrieval operation.

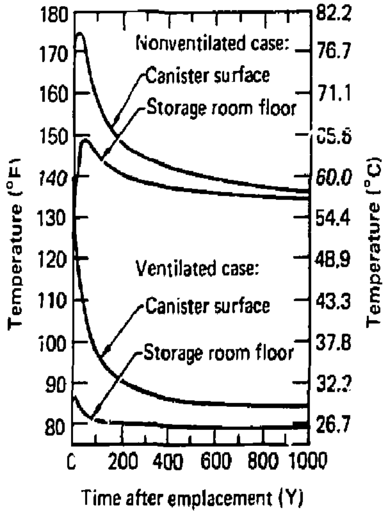

FIG. 20. Canister surface and storage room floor temperature histories for both ventilated (with 79°F air at 10 000 cfm) and unventilated cases.

The analysis focused on the thermal responses of the canister surface, emplacement package components, the near and very near field emplacement medium and both the air and surfaces of the emplacement room. Graphical results provide time/temperature responses and temperature distributions for selected locations. Samples of the results are shown in Figs. 20 and 21.

Summary and Conclusions

The three-dimensional thermal model was used to analyze a low-power spent-fuel emplacement. Detail was included to represent a complicated emplacement package, and boundary conditions allowed for 1000-yr simulations.

Significant conclusions can be drawn from this analysis:

- Annular air gaps surrounding an emplaced *spent-fuel canister increase the canister surface temperature* significantly over that expected from a perfect thermal contact case. Although the maximum temperature difference is only 10°F (5.6°C) in this low-power situation, special attention should be given to gap design for higher areal power loading levels, and lower emplacement media conductivities than bedded salt.
- Ventilation at low-power levels has an immediate cooling effect on the canister and effectively maintains the room surfaces at the temperature of the ventilation air.

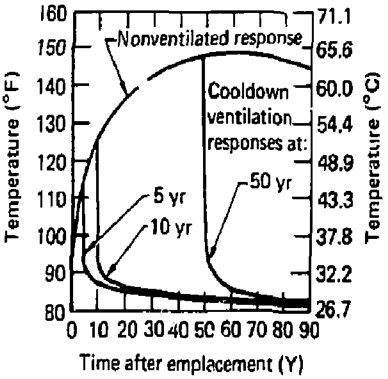

FIG. 21. Storage room floor temperature histories representing cooldown (10 000 cfm of air) from an unventilated state at 5, 10, and 50 yr.

- Emplacement room cooldown simulations showed the time required to reduce the floor temperature to 100°F (38°C) from an unventilated state to be on the order of 2 wk to 6 mo, depending on the time ventilation is initiated. These time requirements could inhibit immediate retrieval operations.

(For further information, contact T. J. Altenbach, Ext. 2-1285.)

Dense Gas Dispersion in the Presence of Two-Dimensional Obstacles

An activity is in progress to numerically and experimentally study the dispersion of a denser-than-air gas in the vicinity of a two-dimensional obstacle in the atmosphere. The term obstacle is used because it may represent a building on land or a transport ship on water. This study is motivated by the need to ascertain what effect the obstacle and the flow field that results from its presence will have on the dispersal of massive quantities of contaminant gases. Such dispersal could result from large spills of hydrocarbon fuels (such as LNG) and industrial gases (such as chlorine and ammonia) that produce negatively buoyant clouds. The study is restricted to a two-dimensional isothermal idealization, addressing the effect of the obstacle on the mixing process and prediction of concentration levels in the vicinity of the obstacle.

Development of a two-dimensional computer model to predict the effect of the obstacle on the velocity field and dispersal of the cloud is nearing completion. The fully viscous Navier-Stokes equations are solved by treating the flow field as variable density, but incompressible from the standpoint of pressure coupling. An Alternating Direction Implicit (ADI) technique is applied to the continuity and momentum equations. The pressure appears in an elliptic equation that is solved by a direct method. The effects of turbulence are modeled by way of the Eddy viscosity hypothesis. The effective turbulent viscosity is taken as a function of the local turbulent kinetic energy and the local turbulent dissipation function, which is a representative time scale of the rate of turbulent decay. Transport equations, containing source and sink terms, are used to calculate the turbulent kinetic energy and the turbulent dissipation function. These are solved by using the ADI technique.

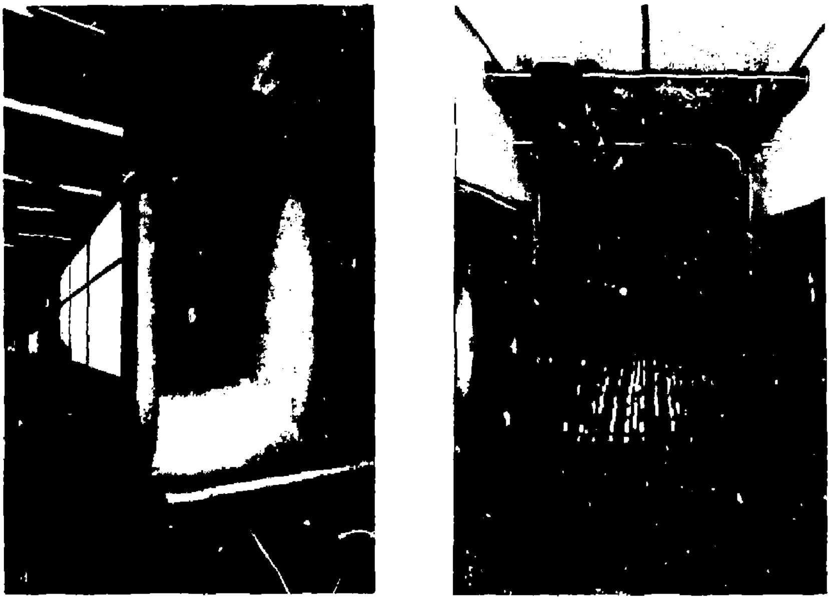

FIG. 22. The tunnel exterior (a) viewed from the entrance section, and the interior (b) view toward the entrance, showing roughness elements designed to generate a thick turbulent boundary layer.

A low-speed, open-circuit atmospheric wind tunnel has been constructed in cooperation with the University of California at Davis to provide data to verify the numerical model. The tunnel (Fig. 22) is 21.3-m long and 1.2-m wide by 1.7-m high at the test section. It was specifically designed to generate turbulent boundary layers as thick as 0.9 m, with peak velocities in the range of 0.3 to 3.0 m/s. Hot wire anemometry techniques are presently being used to determine the velocity distribution and turbulence spectrum of the tunnel flow to ensure that a good simulation of the atmospheric surface layer is being used for upstream conditions when the two-dimensional obstacle is placed in the flow stream. Carbon dioxide will be used as the contaminant gas. An aspirating hot wire probe, which uses a choked orifice immediately downstream of the wire to make the velocity at the sensor dependent on gas composition, will be used to determine spatial and temporal distributions of the contaminant gas. A novel feature of the tunnel is a three-axis probe-positioning unit that allows the probes to be placed anywhere within the 2.4-m-long test section.

(For further information, contact S. B. Sutton, Ext. 2-0322.)

A One-Dimensional Numerical Fluid Dynamics Model of the Spreading of Liquefied Gaseous Fuel Over Water

The use of liquefied gaseous fuels (LGF) as an energy source is increasing in the United States. Transporting and storing these fuels safely is very important because of the possible severe consequences of an accidental spill. Lawrence Livermore National Laboratory is investigating the possible consequences for the Department of Energy.

The fuels of interest, such as natural gas, are gaseous at normal ambient temperature and pressures, and when condensed into a liquid are immiscible with water and less dense than water. Consequently, an accidental spillage on water results in a rapidly spreading liquid pool of evaporating fuel on the water surface. As the liquid fuel vaporizes it spreads, creating a cloud of gaseous fuel. If the vapor cloud is ignited, several different combustion phenomena could occur such as a pool fire, a propagating flame through the cloud, or an explosion This report deals with the modeling of the liquid-pool-spread phase of a spill.

The pool-spread model assumes the liquid pool is cylindrically symmetric and it is based on the one-dimensional conservation equations of mass and momentum. A computer code, LNGTRANS, has been written that solves the conservation equations by using a numerical finite-difference method. The code calculates pool height and velocity as a function of radius from the center of the spill and time after the spill starts.

Types of Spills Modeled

Two types of LGF spills are modeled, an instantaneous spill and a continuous spill of arbitrary duration. The instantaneous spill starts with a stationary volume of liquid fuel on the water surface. As time goes on, the initial volume of fuel spreads over the water surface because of the force of gravity until all of the liquid has evaporated. In the continuous-spill mode there is a constant source of liquid fuel within a specified radius and for a specified duration. The liquid pool spreads out over the water surface until the source is turned off or until a steady state is reached between the source and evaporation from the pool. When the source is turned off, the remaining fuel dissipates just as it would in an instantaneous spill.

The model is based on the one-dimensional conservation equations of mass and momentum. Phenomena included in the model are as follows:

- Sources

  (a) Mass. In the continuous-spill mode, liquid fuel is continually injected into the pool at a constant velocity W. The mass flow rate is then given by $\pi.\rho.w.r_0^2$, where ρ is the liquid fuel density and r_0 is the source radius.

  (b) Momentum. Again in the continuous-spill mode, the injected fuel can enter the source region of the pool with a constant radial velocity U_b greater than or equal to zero.

- Evaporation

  The liquid fuel is assumed to evaporate from the pool with a constant regression velocity V. The evaporative mass flux is therefore $\rho.V$. The evaporating liquid leaves the pool with a horizontal velocity U_t, which is proportional to the local pool velocity U. Generally, $U_t = U$.

- Shear

  The shear force τ at the fuel-water interface is assumed to be proportional to the square of the local pool velocity, U.

Conservation of Mass and Momentum Equations

Conservation of mass is expressed in terms of the liquid pool height and is given by

$$\frac{\partial(rh)}{\partial t} + \frac{\partial(u\,rh)}{\partial r} + (v - w)\,r = 0\,, \qquad (2)$$

where $h = h(r,t)$ is the pool height and $u = u(r,t)$ is the horizontal pool velocity at the radius r and time t. The momentum equation is

$$\frac{\partial u}{\partial t} + \frac{\partial}{\partial r}\left(\frac{u^2}{2} + \delta g h\right) + \frac{\tau}{\rho h} + \frac{w}{h}(u - u_b)$$

$$+ \frac{v}{h}(u_t - u) = 0\,, \qquad (3)$$

where g is the acceleration of gravity, $\delta = 1 - \rho/\rho_s$, and ρ_s is the density of the surface liquid (water). Incorporated in Eq. (3) is the relationship for average hydrostatic pressure P given by

$$P = \frac{1}{2}\rho g h \qquad (4)$$

Finite-Differencing Scheme

The conservation equations are solved numerically in the code LNGTRANS using a finite-difference approach. The conservation of mass equation, Eq. (2), is first written in the form

$$\frac{\partial H}{\partial t} + \frac{\partial uH}{\partial r} + (v - w)r = 0\,. \qquad (5)$$

where $H = rh$. Then, using a second upwind differencing method,[7] the following difference equation is obtained and used in the code:

$$H_m^{n+1} = H_m^n - \frac{\Delta t}{\Delta r}\left(U_R\alpha_R - U_L\alpha_L + \Delta t W\right)\,. \quad (6)$$

where $W = (w - v)(m - 1)\Delta r$ for $m \leq M$ for continuous spills, $W = -v(m - 1)\Delta r$ for $m > M$ for continuous spills, and $W = -v(m - 1)\Delta r$ for instantaneous spills.

$$U_R = \frac{1}{2}(u_{m+1}^n + u_m^n)$$

$$U_L = \frac{1}{2}(u_m^n + u_{m-1}^n)$$

$$\alpha_R = H_m^n$$

$$\alpha_L = H_{m-1}^n$$

n = time increment index

m = spatial increment index.

The spatial increment index M corresponds to the source radius in the continuous spill option.

A second upwind differencing method is also used to difference the momentum equation, Eq. (2), to give

$$u_m^{n+1} = u_m^n - \frac{\Delta t}{\Delta r}\left(\frac{U_R}{2}u_m^n - \frac{U_L}{2}u_{m-1}^n\right)$$

$$- \delta g\frac{\Delta t}{\Delta r}\left(h_m^n - h_{m-1}^n\right) - \frac{\Delta t}{h_m^n}\Big(\text{CSHEAR}\,(u_m^n)^2 \qquad (7)$$

$$+ (C1 - 1)v\,u_m^n + w(u_m^n - u_b)\Big)\,.$$

where the shear term τ/ρ is represented as

$$\frac{\tau}{\rho} = \text{CSHEAR}\,(u_m^n)^2 \qquad (8)$$

with CSHEAR equal to a constant and the horizontal velocity of the evaporating liquid is given as

$$u_t = C1\ (u_m^n)\ . \qquad (9)$$

where C1 is a constant generally taken to be 1.

Calculational Results

The scenario for a continuous spill involves a constant source of liquid fuel within a specified radius. As time proceeds, the liquid pool radius expands and the pool thickness increases, with the height greatest at the center of the source. The spreading of the pool results in a leading wave in the shape of an annular ring traveling away from the spill source. As steady-state conditions are approached, the pool height and velocity approach

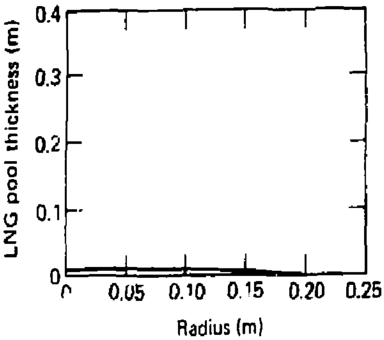

FIG. 23. Plot of LNG pool thickness vs radius after a time equal to one time step.

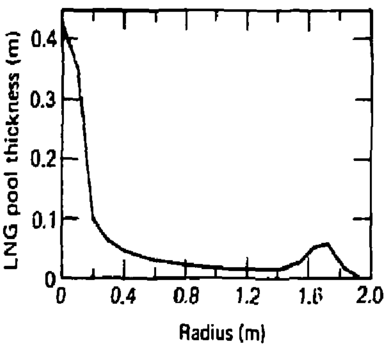

FIG. 24. Plot of LNG pool thickness vs radius 1.6 s after start of spill.

their steady-state values and the leading wave separates from the rest of the pool and travels on a distance until it evaporates.

Results for a continuous spill at a volumetric *spill rate of 15 m^3/min, and a spill source radius r_0* of 0.1524 m are given in Figs. 23 through 28. Figure 23 shows the spill profile after one time step; Figs. 24 and 25 show the height and velocity profile before steady-state conditions are reached; Fig. 26 shows the profile one time step before the leading edge wave separates; Fig. 27 shows the profile of the leading edge wave after it has separated and formed an annulus. The center region of the continuous spill remains essentially unchanged from that shown in Fig. 26 after the separation of the leading wave; Fig. 28 shows the annulus as it is approaching almost complete evaporation.

For further information contact W. Stein, Ext. 2-0323, or D. L. Ermak, Ext. 3-0146.)

Sensor Tower Array Designed for LNG Dispersion Tests

To obtain iso-concentration contours, weather effects, and mixing parameters of natural gas in air after an intentional liquid natural gas spill, an array of towers was instrumented and placed generally downwind of the point at which the spill was made. Twenty weather towers (Fig. 29) distributed both upwind and downwind of the spill point at the Naval Weapons Center, China Lake, Calif., were

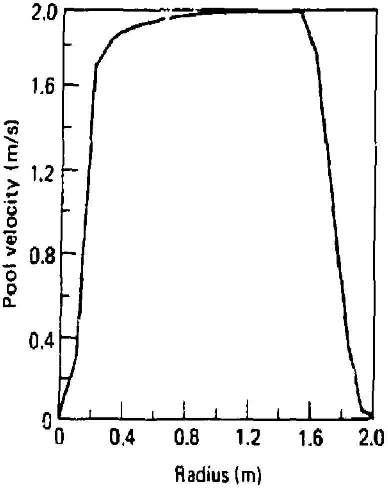

FIG. 25. Plot of pool velocity vs radius 1.6 s after start of spill.

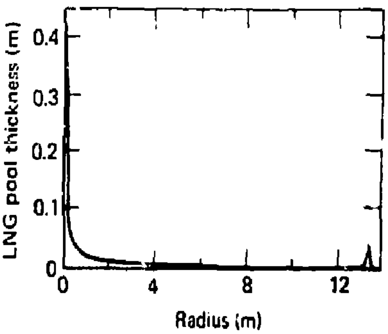

FIG. 26. Plot of LNG pool thickness vs radius 13 s after start of spill.

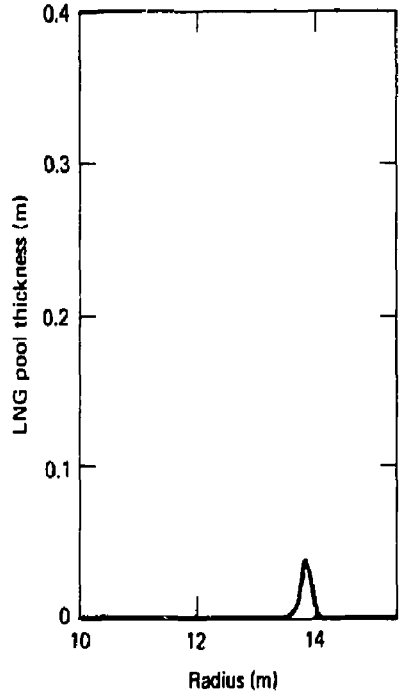

FIG. 27. Plot of LNG pool thickness vs radius for the annulus that has separated from the main pool at 13.6 s after start of spill.

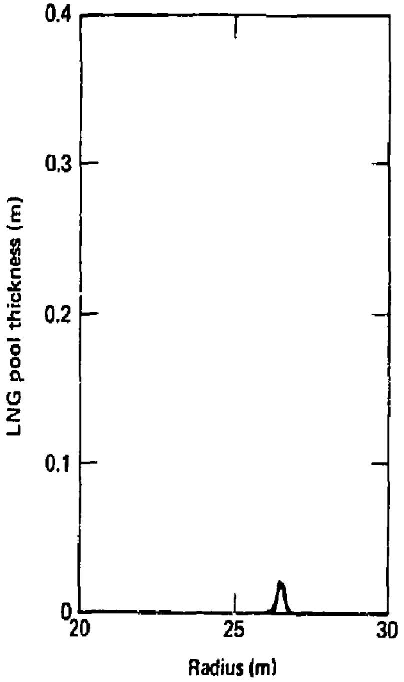

FIG. 28. Plot of LNG pool thickness vs radius for the annulus that has separated from the main pool at 26.2 s after start of spill.

instrumented to determine the wind-field history approximately 2 m above ground level. Wind-field history is a vectoral representation of wind speed and horizontal direction over a given area and for a given time. One tower placed upwind from the spill point was equipped with bivane anemometers, which measure wind speed and wind direction vertically as well as horizontally, at 1-, 3-, and 8-m levels above ground. Thirty towers equipped with gas-sensing detectors and thermocouples at 1-, 3-, and 8-m levels above ground were placed in four rings downwind, the farthest 800 m from the spill point, with an arc length of approximately 40 deg. Five of the 30 towers were also equipped with the bivane anemometers to measure turbulence; these towers were placed near the centerline of the array (Fig. 30). All towers were equipped with antennas to receive commands and transmit data to a recording station approximately 1300 m from the spill point.

FIG. 29. One of the weather towers.

The centerline of the tower array was set up in the direction of the prevailing winds and through the spill point. If the wind for a specific test should be significantly different, towers with instruments and ancillary equipment had to be relocated easily and rapidly to accommodate the wind shift. For the weather towers, a 5-ft-tall commercial snap-out tripod with an antenna mast was used.

FIG. 30. Turbulence tower and spill pond.

For the gas and turbulence towers, a 30-ft-tall free-standing tower with aluminum tubing in a triangular pattern was selected. Besides being lightweight, it was hinged at the base and could be lowered into the near-horizontal position for maintenance and field calibration of the various instruments. The normal foundation for these towers is reinforced concrete with the hinge points projecting above ground. This, however, would negate the rapid portability requirement unless many additional foundations were cast before the tests. A three-armed base was designed with a factory-furnished roof mount used to attach the tower to its base. This in turn was anchored to the ground with earth anchors. An earth anchor is a rod with one or more circular plates formed into a helix and welded to the rod; the rod is literally screwed into the ground. Wind, of all the external forces that might be applied to the towers, would subject the towers, bases, and earth anchors to the highest stresses. The turbulence towers, which have the largest area of exposure, were analyzed to determine maximum stresses of the various components of the tower assembly, including the earth anchors. The calculated load for the earth anchor was 600 lb, which is based on a wind load of 20-lb/sq ft exposed area as specified by the Uniform Building Code. Because the load capacity of an earth anchor depends on soil conditions and because soil conditions at this particular site vary from mud to sand to hardpan, a proof test was devised not only to pull test the anchor, but also the tower and base. A pull test, which was equal to one and one half times a concentrated load at the top of the tower that would apply the same moment at the base of tower as the total wind load, was applied opposite each anchor. As far as the anchors were concerned, this test proved to be invaluable. If after a pull test an anchor had a permanent vertical displacement of more than 1/4 in., it was replaced with either a larger size anchor or different style anchor. With experience, the technicians could predict which anchors would fail during the pull test.

(For further information, contact W. Wakeman, Ext. 2-1227, D. V. Chakedis, Ext. 2-6623, G. M. Bianchini, Ext. 2-6623, B. C. Borman, Ext. 2-6623, R. E. Blocker, Ext. 2-9207, A. D. Rudd, Ext. 2-1729, or W. C. O'Neal, Ext. 2-8369.

References

1. G. A. Burginyon, J. P. Stoering, and R. W. Hill, *J. Appl. Phys.* 49(2), 513 (1978).
2. S. E. Bumpus, J. J. Johnson, and P. D. Smith, *Best Estimate Method vs Evaluation Method: A Comparison of Two Techniques in Evaluating Seismic Analysis and Design*, Lawrence Livermore National Laboratory, Livermore, CA, Rept. UCRL-52746, NUREG/CR-1489, May 1980.
3. T. J. Altenbach, *Three-Dimensional Analysis of a High Level Waste Repository*, Lawrence Livermore National Laboratory, Livermore, CA, Rept. UCID-17984 (1979).
4. B. W. Davis, *Convection and Thermal Radiation Analytical Models Applicable to a Nuclear Waste Repository Room*, Lawrence Livermore National Laboratory, Livermore, CA, Rept. UCID-18103 (1979).
5. B. V. Karlekar and R. M. Desmond, *Engineering Heat Transfer* (West Publishing Company, St. Paul, MN, 1977).
6. T. J. Altenbach and W. E. Lowry, *Advanced Three-Dimensional Thermal Modeling of a Baseline Spent Fuel Repository*, Lawrence Livermore National Laboratory, Livermore, CA, Rept. UCID-18660 (1980).
7. P. J. Roache, *Computational Fluid Dynamics* (Hermosa Publishers, Albuquerque, NM, 1976), p. 73.

NUCLEAR EXPLOSIVES ENGINEERING DIVISION

Our major mission is to support the Laboratory's Nuclear Explosives Program (NEP) in developing operational nuclear weapons systems for the U.S. stockpile. We also support the Nonnuclear Ordnance Program, Organic Materials Division, and H (Physics) Division. We perform studies and develop hardware for Y-Program, Nuclear Regulatory Commission (NRC), Z-Division, and the Defense Nuclear Agency (DNA).

NEED's project teams are dedicated to specific engineering areas: conceptual nuclear design, strategic systems, development and production/liaison for nuclear weapons systems, advanced fission and fusion systems, hydrodiagnostics development, and maintenance and upgrade of the Site 300 test facilities. Our Applied Mechanics Group supports Laboratory programs with calculational expertise in solid mechanics and transport phenomena, and the Auxiliary Systems Group supports Laboratory programs with expertise in high-pressure gas technology.

(For further information, contact R. A. Corallo, Ext. 2-8301.)

Joint Program Under Way to Test Railgun Technology

Lawrence Livermore National Laboratory and Los Alamos National Laboratory are engaged in a joint program to demonstrate railgun technology and the application of the LANL Magnetic Flux Compression Generator (MFCG). The first stage of the program, which culminated in a three-shot test series last year, was started in June 1979 to demonstrate the joint capabilities of the laboratories to design and fabricate an arc-driven small-bore railgun to be used with an explosives-driven MFCG.

The first series of tests were conducted in November 1979, a second series in April 1980, and the final series in July 1980. A total of eight guns were tested. This included seven small-bore (12.7 mm) guns and one large-bore (50.0 mm) gun. Two lengths of small-bore guns were tested (both 1-m guns), designated 1A and 1C, and five 2-m guns, designated 2A through 2E. The large-bore gun, designated 50-1, was 0.3-m long. Polycarbonate projectiles were used with both the small- and large-bore guns. The results of these tests are summarized in Table 1.

The test series were very successful. Small-bore projectiles were launched intact at about 5.5 km/s. Small-bore projectiles were accelerated to 10.0 km/s; however, these high-velocity projectiles were still being accelerated and broke up when they exited the muzzle of the gun. The 50-mm projectile was launched and radiographed at 350 m/s. Although this is not a particularly high velocity, the

TABLE 1. Summary of results of LLNL-LANL railgun experiments.

Experiment	1A	1C	2A	2B	2C	2D	2E	50-1
Accelerator length (m)	0.9	0.9	1.8	1.8	1.8	1.8	1.8	0.27
Initial current (kA)	285	~450	440	~640	640	625	625	630
Peak current (kA)	575	~800	~800	~970	965	1200	~1250	1950
Peak acceleration (Mg)	~1.7	~3.4	~3.4	~5.0	~5.0	~7.7	~8.4	0.22
Peak stress/ elastic limit	4.8	~9.3	~9.3	~14	~14	~21	~23	2.1
Launch velocity (km/s)	2.8	5.6	5.4	~9.9	~9.9	~10.1	~10.1	0.35
Projectile integrity	Total	Half	Total	?	?	?	?	Total

mass of the projectile (165 g) makes this a significant launching for an electromagnetic accelerator.

Another joint LLNL/LANL program funded by the Defense Advanced Research Projects Agency (DARPA) and Army Armament Research and Development Command (ARRADCOM) was started recently to investigate the application of electromagnetic launcher technology to an air defense mission.

Results of the three-shot test series were presented at the DARPA/ARRADCOM-sponsored Conference on Electromagnetic Guns and Launchers held in November 1980 in San Diego.

(For further information, contact A. L. Brooks, Ext. 2-7916.)

Surface Analysis Tool Being Developed for Laser Equation of State

Laser equation-of-state targets, whether using Shiva, Argus, or Janus as the shock source, have required different technologies for target construction than previous equation-of-state (EOS) work. Specifically, we have been asked to provide milled profiles that have surface finishes on the order of less than 300 nm peak-to-peak. Typically, these are ion milled (sputtered) trenches of 5 to 18 μm (Fig. 1) in depth on a 25-to-75-μm-thick substrate. With the introduction of microcircuit technologies, such as ion milling, secondary ion plating, and photolithography, it has become necessary to continuously monitor the target fabrication during each phase. Our present task is to develop various wet or dry etching and coating techniques that will yield appropriate edge acuity, mask registration, and theoretical coating densities.

This monitoring, qualification, and measurement had previously been accomplished by various scanning electron microscope (SEM) technologies outside the immediate process area, which posed severe delays and are sources of contamination. We have now acquired an SEM that will fulfill our rudimentary requirements and give us future flexibility. The unique feature is a 230-mm-diam top loading chamber (Fig. 2) that is needed for our large 100-mm-diam target arrays at approximately 90° tilt. The new capability is further enhanced by various video options, including scan rotate, dual magnification, and homomorphic processing (Fig. 3). We will also have an alphanumeric graphics generator for photomicrographic picture editing. These capabilities will be invaluable in assisting us to develop the various processes dictated by the materials introduced in the target design.

(For further information, contact G. J. Devine, Ext. 2-9649.)

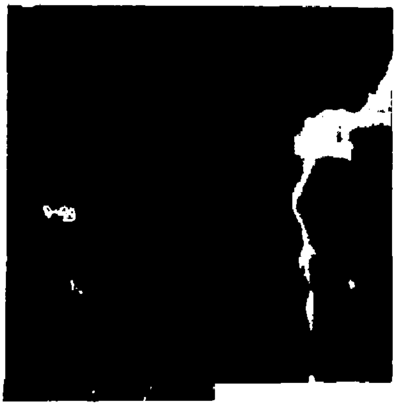

FIG. 1. A photomicrograph of particle contaminate. Views from left to right are Y modulation, derivative processor, and standard SEM scan.

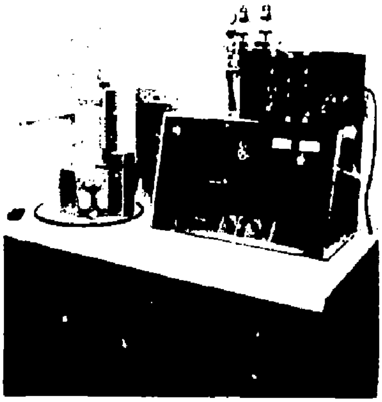

FIG. 2. The SEMCO Nanolab 7 SEM with top-loading 230-mm-diam chamber for the inspection of 100-mm-diam laser EOS target arrays.

FIG. 3. Ion-milled Shiva EOS target.

Airfield-Attack Submunition Under Development

The NONO (Nonnuclear Ordnance) I Group of the Nuclear Explosives Engineering Division has recently been given the task of weaponizing the Velocity Augmented Munition-93 mm (VAM-93) submunition. The VAM-93 is a three-stage conventional warhead planned for use against airfields. Approximately 60 of the nonnuclear submunitions would be carried on a cruise-type missile and dispersed in rows across an airstrip.

The VAM-93 consists of a forward shaped charge that detonates on contact with the runway, softening it for later penetration by the main charge. Simultaneously with the firing of the forward shaped charge, a velocity augmentor in the rear of the submunition fires, driving the main charge through the rubblized cavity in the crater. After the main charge has penetrated, it is detonated, forming a cavity up to 8 ft in diameter in the runway. This sequence of operations is shown in Fig. 4.

Nuclear Explosives Engineering Division has engineering responsibility for the overall submunition, and Nuclear Energy Systems Division is developing the fuzing for the submunition, which will consist of a conventional low-energy fuze or a high-energy slapper-type unit. The system integrator for the overall missile will be General

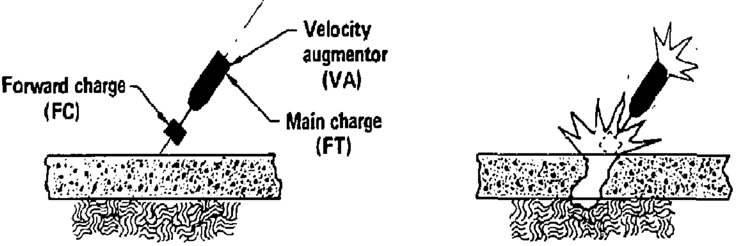

FC and VA simultaneously detonate

FT detonates

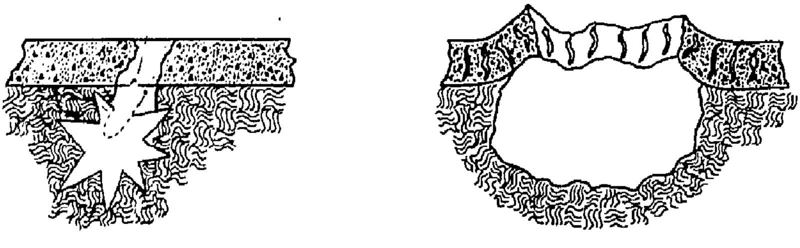

After

FIG. 4. Velocity Augmented Munition-93 detonation sequence.

Dynamics, with overall project direction coming from the Joint Cruise Missile Project Office. Initial application will be with the medium range air-to-surface missile (MRASM).

The velocity-augmented submunition concept is also being studied for other applications, such as a self-burying demolition munition, a foxhole digger, and a shoulder-launched urban attack munition.

(For further information, contact R. S. Varosh, Ext. 2-7749.)

An Experimental Determination of Fusion-Zone Energy Transport During Arc Welding

A large body of empiricism has demonstrated the overriding importance of weldpool motion of fusion-zone size and the important dependence of weld quality on weldpool thermal-hydraulics during electron beam (EB) and gas-tungsten-arc (GTA) welding. The weldpool fluid motion erodes the fusion boundary and controls weld penetration and constitutional supercooling (this latter parameter governs solidified grain structure).

An experimental apparatus is being designed to quantify the effects of weldpool fluid motion on thermal conductance at the solid-liquid fusion boundary. The apparatus is designed for GTA welding, but the methodology can be extended to include EB or laser welding. A high-melting-point, high-electrical-conductivity molybdenum hemispherical shell contains a low-melting-point, low-electrical-conductivity specimen material (bismuth or lead or a tin alloy of these). Both shell and specimen act as the anode of the arc, with the cathode symmetrically positioned above the surface of the specimen. The convex surface of the molybdenum shell is impingement-cooled by gas jets issuing from the holes of a perforated, surrounding stainless-steel hemispherical shell. Heat flux and temperature measurements are taken at six locations on the molybdenum shell and are extrapolated back to the fusion boundary using a procedure previously applied by Landram[1] as given by the inverse solution of Burggraf.[2]

The essential features of this apparatus are twofold: (1) Heating and cooling rates can be independently varied, and (2) The instrumentation provides a means to obtain the fusion-zone (liquid-side) thermal conductance. Consequently, in the steady state the Lorentz-induced fluid motion can be controlled and its effect on fusion-zone thermal conductance can be measured and compared to the diffusional limit (Nusselt number = 2). The experiment can also be operated in a transient mode by suddenly terminating arc power and comparing solidified grain structure to instantaneous supercooling.

To enhance weld quality, an experiment is being designed to obtain a better understanding of weldpool fluid motion as it controls penetration and grain structure.

(For further information, contact C. S. Landram, Ext. 2-8569, or J. G. Moore, Ext. 2-8715.)

The Three-Dimensional Code PELE3D

A three-dimensional incompressible flow code has been written using the technology developed for the two-dimensional code PELE-IC. (PELE-IC was originally developed to model pressure-suppressant experiments for the General Electric Mark I Reactor.) At the current stage of development, the code has the following features:

- Plane and curvilinear coordinates.
- Regular and proportional zoning.
- Rigid obstacles can be specified along portions of grid lines.
- Variable time step.
- Restart capability.
- Coupled to a curved rigid structure in the vertical plane.
- Free-surface capability.
- Bubble dynamics.
- Up to eight downcomer pipes with three different zoning choices.
- Time history plots.
- Three-dimensional graphics.
- Applied external pressure sources.
- Compressible ullage.

The code is operational on the CRAY computer and runs relatively fast using 0.03 ms for each cell-cycle iteration. Most of our successful test runs have averaged slightly over two iterations per cycle so that an estimate for predictions of runtime would be approximately 0.06 ms per cell-cycle. We have noticed that the three-dimensional code generally

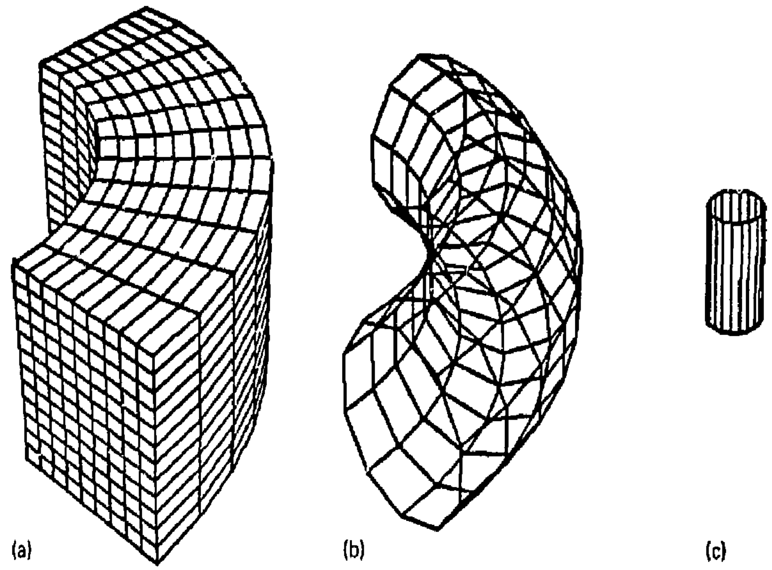

FIG. 5. Components of the zoning for the 90° sector of the LLNL 1/5-scale pressure-suppressant experiment.

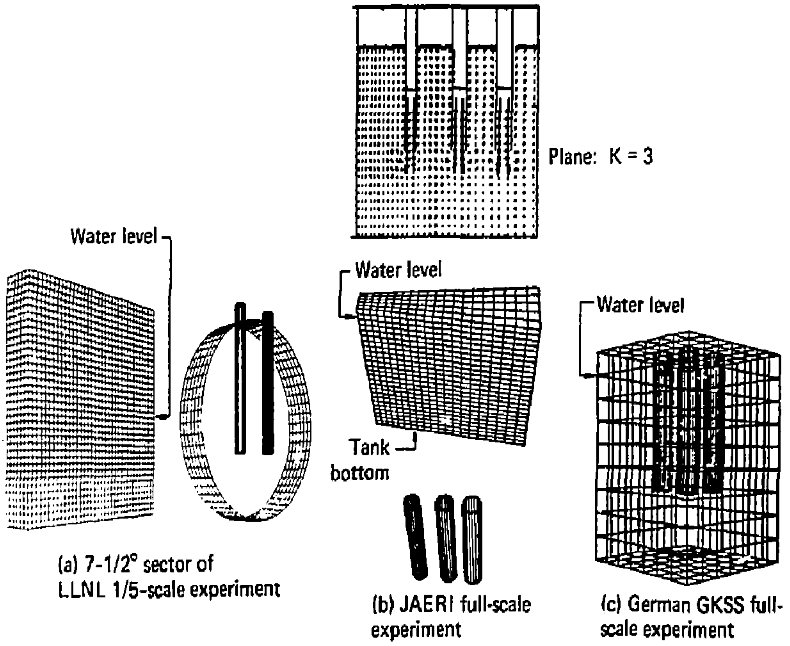

(a) 7-1/2° sector of LLNL 1/5-scale experiment

(b) JAERI full-scale experiment

(c) German GKSS full-scale experiment

FIG. 6. Zoning for the test problems.

converges faster than the two-dimensional code because of the extra degrees of freedom.

The code has been used for scoping calculations of the LLNL 1/5-scale Mark I Pressure-Suppressant Experiments, the West German full-scale GKSS wetwell experiment, and the Japanese JAERI full-scale experiment.

Figure 5 shows the components of the zoning for the LLNL 1/5-scale geometry. The curvilinear Eulerian fluid region is zoned as in 5(a). Within the region, a curved rigid structure is defined as shown in 5(b). And finally, individual downcomer pipes as shown in 5(c) are specified at the appropriate locations in the grid. The water level is specified and the driving pressure from the drywell is applied to the water surface in the downcomer pipes. Figure 6 shows the zoning for the three experiments currently being investigated with the PELE3D code.

(For further information, contact W. H. McMaster, Ext. 2-7251.)

References

1. C. S. Landram, *ASME J. Heat Transfer* 96(3), 425 (1974).
2. O. R. Burggraf, *ASME J. Heat Transfer* 86(3), 373 (1964).

WEAPONS ENGINEERING DIVISION

Weapons Engineering Division (WED) is responsible for engineering activities supporting nuclear weapons development, production, and maintenance of a major portion of the national stockpile. In providing these services, the Division keeps abreast of new developments in safety, weapon control, and guaranteed weapon life extension.

Our activities include new weapon development, environmental testing, weapons control and enhanced safety, initiation systems development, engineering technology, and special materials procurement. Production work involves communicating product definition and design intent to the DOE contractors responsible for component fabrication and assembly. In addition, active monitoring of the stockpile requires a large effort in disassembly surveillance of stockpile weapons to ensure that design requirements have indeed been met and to monitor physical changes that may eventually limit the useful life of a weapon.

The Special Materials (SM) office purchases goods and services from integrated contractors, military commands, and other governmental agencies for all LLNL programs. This office is also responsible for coordinating Laboratory guidance on weapon development activities by the integrated contractors, purchasing special isotopes used in a variety of programs, and providing the DOE with a forecast and management plan on nuclear material usage.

(For further information, contact R. E. Clough, Ext. 2-8721.)

Dynamic Response of the GLCM Conventional Bomb Shelter

The W84 warhead is a viable candidate for weapon systems other than the Ground Launched Cruise Missile (GLCM). We therefore plan to design the W84 warhead package to meet the stockpile-to-target-sequence (STS) environments of other applicable weapon systems. One such candidate system is the Submarine Launched Cruise Missile (SLCM). During a depth charge attack, this system has a rather severe shock environment. Consequently, we are designing the W84 to withstand this shock level.

Presently, a question of major concern is whether this SLCM STS contains the worst-case shock environment to which the system will be subjected. Higher acceleration levels may actually occur in the conventional bomb shelter. However, this preliminary worst-case analysis indicates that shock levels present in the GLCM shelter are less than those for SLCM.

Background

Initially, the feasibility of performing this calculation from first principles was investigated. Two approaches were possible. Early-time calculations could be performed with an Eulerian hydrodynamic code for the high explosive detonation and resultant cratering phenomena in the soil. Such a code could then be coupled to a Lagrangian structural code to capture the late-time dynamic response of the shelter. This procedure, however, would require a rather extensive code development effort. The calculation could also be performed solely with a Lagrangian code using a rezoner when necessary. Neither of these approaches appeared to be very practical. Both would require extensive parameter studies with material properties to establish any confidence in the results. In addition, the uncertainties and relatively large spread of experimental data strongly suggest that such approaches are not warranted. Another approach is to use an empirical equation to estimate the loading of the roof from the high explosive blast.

Only two-dimensional codes are available for the first two methods. The empirical approach for loading the roof was chosen since the three-dimensional aspects of the problem could be captured using the nonlinear dynamic finite element code DYNA3D[1]

Analysis

The U.S. Army Engineer Waterways Experiment Station at Vicksburg, Miss., has developed empirical equations to estimate free-field stresses and ground shock resulting from bombs detonating on or within a burster slab.[2] Upon reflection off the roof, the free-field pressure wave typically doubles. To simulate a spherical wave propagating from the high explosive charge, separate load curves with the appropriate arrival times were generated for each element on the roof.

An equation of state for the soil, which is *in situ* deep sand, was obtained from Coltharp.[2] A pressure-volumetric strain curve was used for the deep sand as well as for the reinforced concrete of the shelter. The model also includes a deviatoric yield function that is described in terms of the second invariant.

Model Verification

A small-scale high explosive test from the Dice Throw Event[3] conducted by the waterways experiment station was used to verify modeling techniques. The shelter and soil were zoned from the roof down, and the structure was loaded as previously described. Good agreement was obtained with the experimental results.

A short parameter study was performed to further substantiate the results. Rise times of 20 μs, 1 ms, and 3.5 ms were used for the pressure pulse. Since the response time of the structure is in the millisecond regime, no appreciable difference was observed. Therefore the slower rise times for the pressure pulse were used in subsequent calculations, saving more than a factor of 2 in computational time. To determine the possible effect of a pressure wave reflecting off the bottom surface of the finite-element mesh and perturbing the solution, the amount of soil zoned under the floor was doubled in height. Again, no appreciable difference was found.

GLCM Shelter Results

The GLCM shelter is buried 2.13 m beneath a 1.52-m-thick concrete burster slab which is just below the surface of the ground. The threat is that of an overhead burst of a conventional 1,000-kg general purpose bomb which would partially penetrate the burster slab. Approximately 454 kg of TNT-equivalent high explosive is present in such a bomb.

A magnified deformed shape of the mesh is presented in Fig. 1. Because of symmetry, only half the structure necessitated zoning. Displacements were magnified by two in order to more clearly show the location of the high explosive charge.

It appears unlikely that acceleration levels greater than that for the SLCM will occur in the conventional shelter for GLCM. As the floor rapidly accelerates downward, the weapon system will accelerate downward at 1 g with separation from the floor occurring. Maximum accelerations occur when the floor rebounds and meets the weapon system. This rebound acceleration is an order of magnitude below those for SLCM.

Recommendations

The recommendation derived from the study is that the worst-case shock environment will be that of SLCM. This preliminary worst-case analysis indicates that the shock levels present in the GLCM shelter are less than those for SLCM. An exhaustive parameter study was not warranted for this calculational effort at this time. This technique needs experimental normalization.

The numerous assumptions one must make to obtain a solution will always tend to undermine the results from a purely analytical approach. On the other hand, there is a large amount of scatter in experimental data also. Hence, it would be wise to pursue both avenues vigorously to obtain shock environments with any degree of confidence.

Therefore, the importance of scaled field tests performed by experienced personnel, such as those available at the waterways experiment station, cannot be overemphasized. Once good experimental results are obtained, this calculational technique can be normalized. Subsequently, an extensive parameter study can follow to increase our confidence in the shock environment.

(For further information, contact C. W. Clausen, Ext. 2-8881.)

Detonation Blast Wave Effect on Enhanced Safety Vaults

Accidental detonation of a missile motor is one of a number of potential accident environments for a nuclear weapon. To minimize or prevent plutonium dispersal in the event of such an accident, the Weapons Engineering Division has an Enhanced Safety program to improve nuclear weapon design. Under this program, WED's Special Projects and Analysis Group prepared an enhanced safety design test as an add-on to a solid propellant detonation test undertaken by the Air Force Rocket Propulsion Laboratory (AFRPL) at Edwards AFB in California.

In its test the Air Force detonated 6,772 lb of solid propellant in an upper-stage missile motor; the energy release was estimated to be equivalent to about 10 000 lb of TNT. The purpose of the add-on experiment was to evaluate a TATB-based insensitive high explosive in the detonation environment. Additionally, this experiment made possible the evaluation of four enhanced safety vaults. The vaults represented several different safety designs in which the plutonium would be stored separately from the high explosive.

The Special Projects and Analysis Group's analytic effort was confined to posttest calculations. We tried to develop an analytic methodology that produced calculated deformed shapes similar to those of the test. The objective was to develop an analytic technique that can be used as a design tool capable of calculationally testing proposed designs before future experiments. One major difficulty in developing a methodology with a high confidence level was that only one design survived the test. Our technique does result in good agreement with the one surviving design; however, additional tests will be required to determine its validity.

Analysis

Our first approach to the problem was to zone both the vault and the high explosive (HE) and use the high explosive burn option in DYNA2D. The results from this approach were never satisfactory. Early in the calculations, the high explosive elements become tangled, terminating the problem.

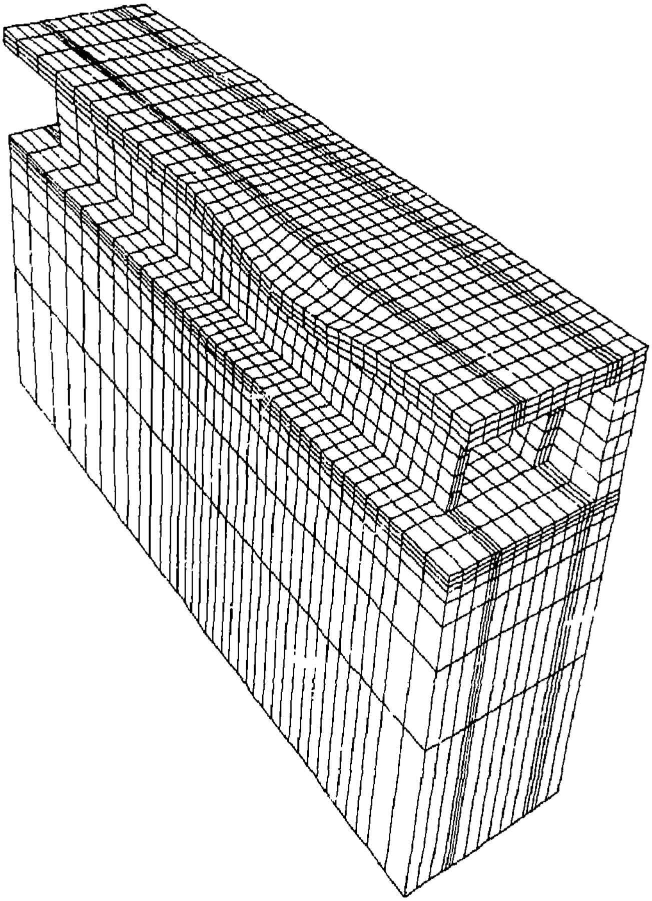

FIG. 1. An empirical relation is used to estimate the blast loading of the underground structure. Calculations indicate that acceleration levels in the GLCM shelter are less than those in the SLCM STS.

The rezoning capabilities of DYNA2D enabled the calculation to run longer, but never provided sufficient treatment of the shock wave passing by the vault.

Decoupling the high explosive blast from the actual mechanical response of the vault proved far more productive. A method has been developed for calculating a pressure-versus-time profile for locations in the proximity of an HE detonation. A closed-form solution of the normal reflected pressure pulse has been derived. Assuming a plastic collision of HE gas with the vault but no gas collisions, the amount of momentum imparted to the target by each gas particle equals the amount of momentum carried by the particles. Thus the reflected pressure is dependent on the amount of momentum delivered per unit area per unit time or

$$P_r = \frac{d(MV)}{A\,dt} = \frac{dI_r}{dt}\ , \tag{1}$$

This pressure is equal to the density times the velocity of the material reaching the target point at that time. The time-varying density can be expressed in terms of the initial density ρ_0, the initial radius of the explosive charge r_0, the maximum velocity V_m, the time t, and the distance to the target r. The reflected pressure becomes

$$P_r = \left[\rho_0\left(\frac{r_0}{r_0 + V_m t}\right)^3\right]\left[V_m\left(\frac{r}{r_0 + V_m t}\right)\right]^2\ . \tag{2}$$

V_m can be calculated from conversion of HE chemical energy to kinetic energy of all primary materials (Σm) as

$$V_m = \sqrt{\frac{2\,E_{HE}}{(\Sigma m)}}\ .$$

The time the pressure acts on the target t' is

$$t' = t - t_0\ , \tag{3}$$

where t_0 is the time to reach the target or

$$t_0 = \frac{r - r_0}{V_m}\ . \tag{3a}$$

The impulse can be obtained by integrating the pressure as a function of time.

Results

The pressure-time profile that results from the aforementioned calculation is presented in Fig. 2. This pressure-time profile is subsequently used as input for DYNA2D to calculate the vault's mechanical response. For the calculation of this experiment, we assumed the pressure wave of Fig. 1 impacted the end of the vault as a plane wave. The model was completely filled with lead to mock the lead shot/silastic matrix that filled the tested vaults. The calculated deformed shape for the 3/8-in.-thick titanium vault can be seen in Fig. 3. Note the good agreement between the calculated shape and the measured shape. Additionally, the calculated maximum plastic strain was 20%, which indicates a prediction of survival. The titanium vault did survive the test.

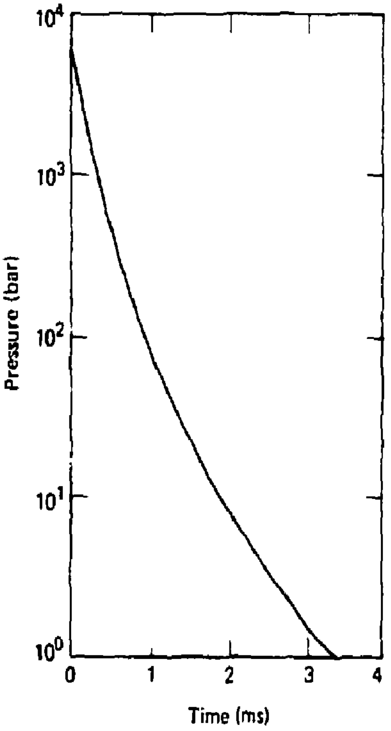

FIG. 2. We decouple the mechanical response of the vault from the actual shock-wave formation. Based on the experimental parameters, a pressure-time profile is calculated and used as input to DYNA2D.

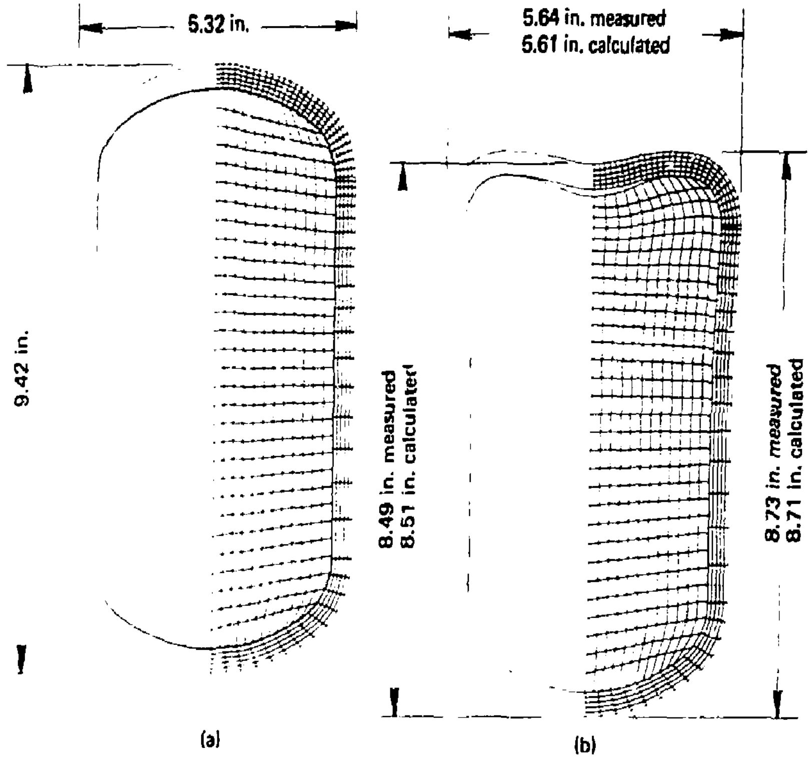

FIG. 3. Applying the pressure-time profile to the model of the 3/8-in.-thick pure titanium vault (a) produces a deformed shape (b) which is in good agreement with the actual deformed shape after the detonation.

We also applied the pressure-time profile to a model of the 1/4-in.-thick stainless steel vault. Calculations indicate greater deformations than for the titanium vaults. The calculated maximum plastic strain was 25%, which might lead one to believe that the vault should have survived. In fact, the vault did not survive but failed at the weld region located midway between the ends.

In conclusion, we have formulated a methodology that does produce good agreement with the deformed shapes and does show the relative strength between the two vaults just discussed. However, we are still trying to improve our model of the weld area and will need additional experience to fully test our methodology.

(For further information, contact R. A. Bailey, Ext. 2-8512, or G. B. Min, Ext. 2-6813.)

References

1. J. O. Hallquist, *Preliminary User's Manuals for DYNA3D and DYNAP (Nonlinear Dynamic Analysis of Solids in Three Dimensions)*, Lawrence Livermore National Laboratory, Livermore, CA, Rept. UCID-17268, Rev. I (1979).
2. Personal communication with David Coltharp, U.S. Army Corps of Engineers Waterways Experiment Station, Vicksburg, MS.
3. R. S. Cummins and G. E. Albritton, *Federal Republic of Germany, Structures Test Program, Dice Throw Event, Report 5, Small-Scale High-Explosive Tests*, Technical Report N-77-2, U.S. Army Corps of Engineers Waterways Experiment Station, Vicksburg, MS (1979).

ENERGY SYSTEMS ENGINEERING DIVISION

We provide mechanical engineering support to the Laser (Y) Program in two major categories: laser fusion (LF) and laser isotope separation (LIS). The LF effort is directed in the short term at understanding the basic physics problems associated with using high power lasers to implode small fusion targets; the long term goal is to develop the fusion process to provide an unlimited source of power. In the LIS program the unique properties of coherent laser light are used to selectively photoionize atoms of a given isotope in a material containing several different isotopes. The ionized atoms can then be separated and enriched through the use of extractor-collectors. A long-term goal is to demonstrate cost-effective enrichment of ^{235}U at rates applicable to commercial production plant requirements.

The tasks associated with each area are varied and challenging, encompassing essentially all disciplines of advanced technology. In this issue we highlight three accomplishments that help to illustrate the type of work performed by the Division.

- The January 24, 1980, earthquake damaged the Shiva laser. Experiments performed with Shiva are particularly important to the LF program, so repair of this laser was one of our highest priority items. Many components are unusual in that they require special care and alignment. For example, the optics must be dust free to prevent excessive absorption at high energy laser light, and must be aligned to ensure that the full 20-cm-diam beam can be focused to a spot 100-μm-diam or less We worked as members of a team of physicists, and electronics and mechanical engineering personnel to assess the damage, set a schedule for repair, and complete all work at a total cost of less than $100,000. A full schedule of experiments was resumed after only 3-1/2 weeks. The rapid recovery illustrated the ease with which our multidisciplinary project teams responded

- An important part of any Shiva experiment is the diagnostics which permits better theoretical and experimental understanding of the physical phenomena. We developed an x-ray backlighting diagnostic system that for the first time permits satisfactory measurement of target hydrodynamic behavior. Photographs of the targets are taken at a magnification of 22X and have a time resolution of 15 ps. A photograph shows a 600-μm-diam gold disk as it explodes following energy deposition from the Shiva laser.

- Tunable dye lasers are used in the LIS program for development of large-scale processes to enrich uranium. The lasers must be held at a precise temperature in order to establish a wavelength that optimizes efficiency. An integrated dye flow system was developed that maintains the temperature within ±0.05°C and pumps the necessary mixture of dye through the laser optical cell. The system operates routinely with minimal maintenance. Wavelength drifts are so small that they can be servo-controlled with automated subsystems attached to the individual lasers.

(For further information, contact J. E. Keller, Jr., or J. R. Haubler, both at Ext. 2-7582.)

Rapid Recovery Achieved for Shiva Laser Following Earthquake

On January 24, 1980, the Shiva laser system was damaged by an earthquake whose epicenter was about 20 km (12 mi) from the LLNL. The peak magnitude was 5.5 on the Richter scale. The first shock was followed by 5.2 and 4.8 shocks. The duration of the three distinct shocks was almost 30 s. Shiva has withstood shocks of similar magnitude in the past, but the combination of shocks and the longer duration created damage not experienced previously.

The Shiva laser and target frames were accelerated horizontally to approximately 0.5 g. This acceleration caused the laser frame to move an estimated 1/2 in. during the shocks. However, the laser frame returned to within 1/16 in. of its original position and its primary anchor was intact. The target frame rotated and tipped during the shocks. This combination of movements loaded the twenty 3/4-in. tie-down bolts nonuniformly, causing all to fail in a combination of shear and tension (see Figs. 1 and 2). Two of the roller bearings under the frame were damaged. The target frame moved 0.4 in. west and rotated counter-clockwise 0.75 in. as measured at the f/14 spatial filter input.

(Both space frames are large optical benches and very stiff. Each is anchored to the floor at a

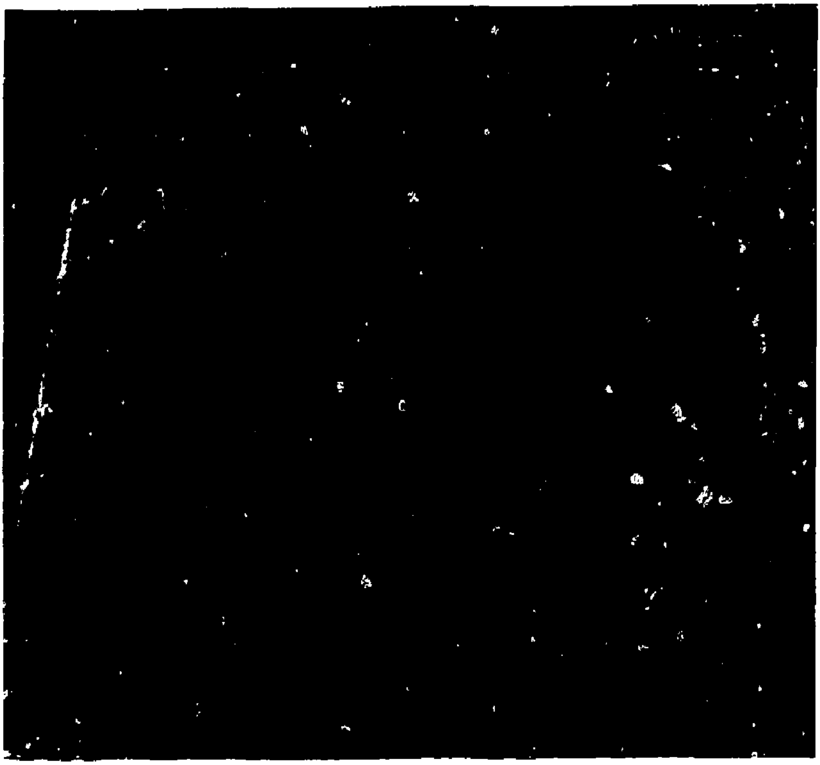

FIG. 1. Shiva target frame model shows the location of the seismic mount at the frame center. New buttress anchors will restrict rotation and tipping of the frame.

FIG. 2. Two of the 20 bolts that failed from a combination of shear and tension.

single seismic anchor point. The remaining resting points are on roller bearings which allow the frame to move laterally in all directions. This prevents distortions due to thermal variation which would result in misalignment of the laser.)

The computer-type floor around the laser frame was dislocated and several of the floor support posts failed. This damage prevented the use of the 4000-lb personnel carriers (flying tigers) during the early stages of damage investigation and laser realignment. The floor was safe for personnel, thus permitting work on the lower four beam lines.

A fire sprinkler pipe was ruptured beneath the laser frame by the frame movement. The release of a large amount of water caused the capacitor bank, which is located below the laser, to become flooded. Movement of the capacitors on their insulators caused the insulating sheets to crack. The flooding and cracked insulators required the capacitor bank to be dried out and the insulating sheets to be replaced. Repairing flood damage became a pacing item in restoring full operation.

There were no injuries to personnel and damage to the building was superficial. All emergency electrical power to the building was secured during the flooding to eliminate the possibility of electrical problems created by water, ungrounded equipment, or loose wires.

Recovery

Immediately after the earthquake, personnel were excluded from the laser and target bays until the extent of the damage could be determined. After ensuring that personnel safety had been adequately taken care of, our first priority was to return electrical power to the spatial filter ion pumps to maintain their vacuum and restart the air conditioning/HEPA filter fan systems. Establishing the clean room air flow system was important to prevent contaminants and moisture from migrating into laser components and to maintain the temperature stability of the system.

The laser frame was found to be safe. Inspection and realignment of the laser components began. The target frame was judged unsafe until it was reanchored to the floor, and only limited access to the target bay was allowed.

Inspection of the laser components mounted on the laser frame revealed that there was no damage to individual components. Realignment of the laser and a survey using benchmarks located outside the building revealed the amount of misalignment between the frames.

Realignment and activation of the laser began on January 28 and continued until the entire system was restored to full operating condition on February 20. The work resulted in better alignment of the system than before the earthquake.

A new set of anchors was designed for both space frames, which upgraded them to the new

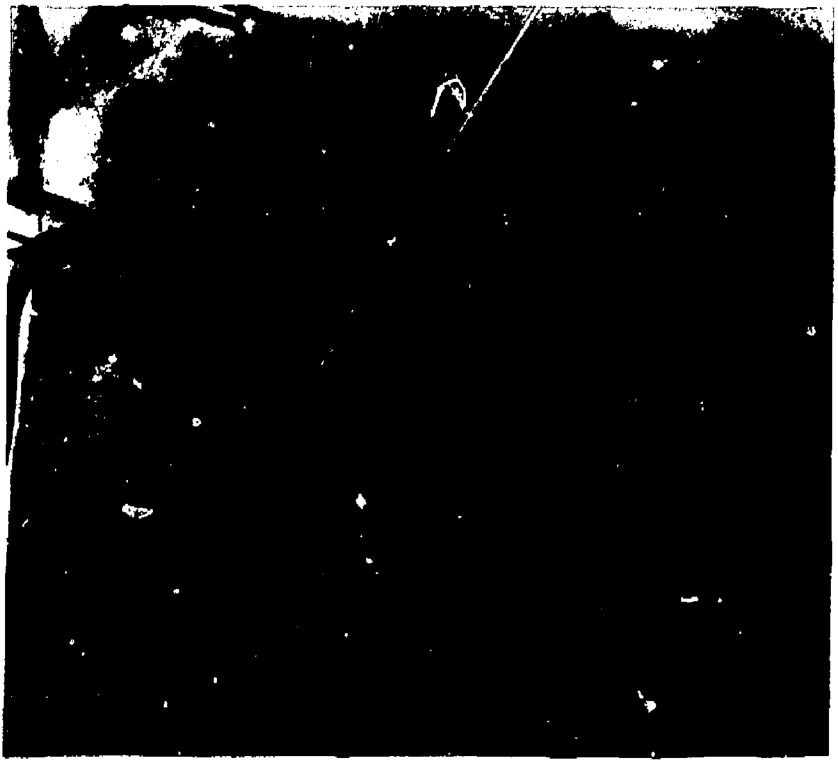

FIG. 3. One set of buttress plates on the Shiva laser frame. These supplementary anchors restrict vertical motion and rotation of the space frame.

Laboratory requirement of 0.5 g horizontal acceleration. It was not necessary to move the laser frame, and its new anchors were installed on February 1. These anchors also prevent the frame from rotating beyond the travel of the support roller bearing. Figure 3 shows one of the new buttress supports. The original seismic mount was not replaced. There is a possibility that it was damaged below the floor surface and additional anchors were added. The target frame weighing about 500 000 lb was jacked up 1/4 in. using 15 hydraulic jacks lifting simultaneously (see Fig. 4). The roller bearings were removed, inspected, repaired, and reinstalled. The frame was lowered and realigned to the laser system. A typical roller bearing used on both space frames is shown in Fig. 5.

This frame was repositioned on February 5 after the new anchors (see Fig. 6) were in place. The new anchors assured complete safety in the event another earthquake occurred during the 10-hr repositioning period.

The capacitor bank area was dried out and the insulating plastic sheets were replaced, allowing the rod amplifiers to be fired on February 13, 20 days after the earthquake.

Target viewer alignment of the target chamber and target diagnostics revealed there was no misalignment between the chamber and components on the target space frame. After the target space frame was repositioned, the neutron time-of-flight line-of-sight tube had to be realigned slightly to correct for relocation of the space frame relative to the building.

Once the space frames had been made safe for personnel, it was possible to realign the entire laser system from oscillator to the target chamber. With the capacitor bank power supply operational, full activation of the laser began on February 15. The first 20-arm target shot was made on February 20, less than one month after the earthquake. Reactivating a system as complex as the Shiva laser system required a significant amount of interaction and planning. This is obviously compounded when additional problems are imposed such as structural damage. An interdisciplinary team of about 100 persons working in close coordination made possible the rapid recovery.

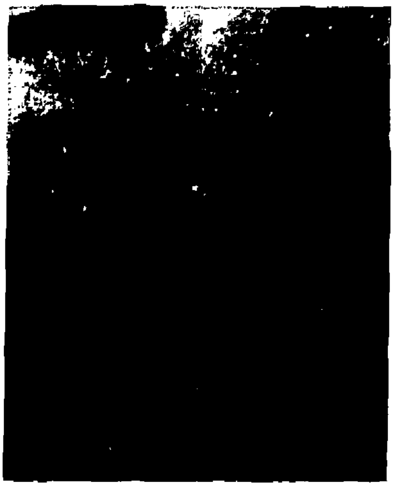

FIG. 4. One set of the 50-t jacks used to lift the target frame for repositioning.

FIG. 5. A roller bearing typical of those used on both space frames. Note the fractured roller at lower right; this roller broke when the target frame tipped during the earthquake.

Summary

The design of the seismic anchors for Shiva met their design criteria.[1] None of the more than 1500 optical elements were damaged and all the assemblies that were mounted solidly to the space frames remained aligned within 0.25 in. The laser frame anchor bolts may have loosened but did not break. The original laser frame seismic mount is now backed up by a new mount system. The target frame

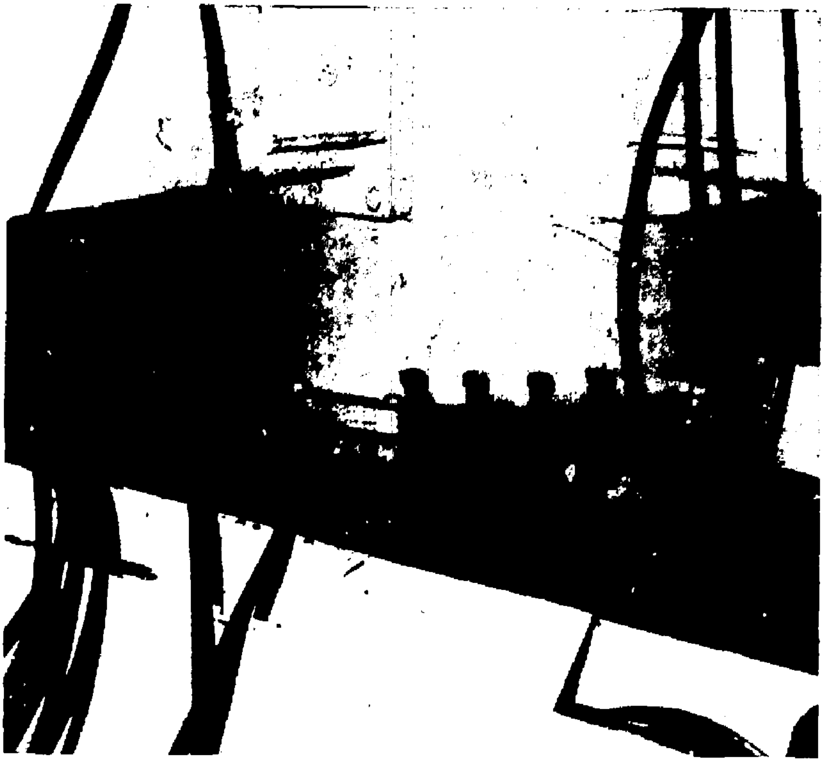

FIG. 6. Two of the five new buttress blocks that anchor the seismic mount on the target frame.

anchor bolts did break. An analysis of the anchor bolts showed an ultimate tensile strength of each bolt to be 93 000 psi and ultimate shear to be 55 000 psi, indicating that the individual bolt strength was as expected. Allowing the anchor bolts to fail at a high load prevented greater damage to the system. A major problem could occur if the frame is tied too rigidly to the floor. A larger earthquake could then structurally damage the frame, and possibly break components loose from their mounts.

The single occurrence that caused the greatest delay in reactivation of the system was capacitor bank flooding from the rupture of a fire sprinkler and water lines. A floor drain system has been installed to prevent overflow of water into the capacitor bank.

Full system operation was achieved within one month after the earthquake and at a cost of less than $100,000.

(For further information, contact H. G. Patton, Ext. 2-0406, J. W. Herris, Ext. 2-5407, C. A. Hurley, Ext. 2-0681, C. D. Swift, Ext. 2-9010, or D. R. Speck, Ext. 2-5479.)

X-Ray Backlighting Diagnostic System Developed for the Shiva Laser

The process by which laser light is used to compress deuterium-tritium (D-T) fuel and cause thermonuclear burn can be divided into four parts: absorption, energy transport, target hydrodynamics, and thermonuclear burn. Over the last several years, significant effort has been devoted to improve theoretical and experimental understanding of absorption, energy transport, and the state of the target at burn time. To date, few measurements have been been made of target hydrodynamic behavior. The use of x rays that can penetrate dense material permits determination of the density profile of the moving object through the relation between areal density and the attenuation of x rays. Measurements of this type have been very limited due to problems such as dynamic range, resolution, and target alignment.

We have developed an x-ray backlighting system (Figs. 7 and 8) to minimize the problems of dynamic range, resolution, and target alignment.

The system we use for the x-ray backlighting is a 22X magnification Wolter (hyperboloid-ellipsoid) axisymmetric grazing incidence x-ray microscope as the objective element and an x-ray streak camera of LLNL design as the detecting device. The microscope has a resolution of 2 to 3 μm with a depth of field of $\pm 100\ \mu$m. The streak camera has a thin photocathode of sensitivity from 100 eV to more than 10 keV. The system is limited by the resolution of the streak camera, which is 100 μm. The time resolution of the streak camera is 15 ps; its temporal dynamic range is approximately four orders of magnitude.

The x-ray backlighting system is aligned using a visible-light target viewer mounted coaxially along the x-ray microscope line of sight (Fig. 7). A visible light lens is mounted in the center of the x-ray microscope mirror such that its principal plane and optical axis coincide with the x-ray microscope. The initial alignment is done by placing a single-mode optical fiber mounted in the center of the chamber and projecting the image onto the streak camera slit; the streak camera is then positioned to center the image on the cathode slit.

A pellicle, mounted in an alignment camera 7(a) located in front of the streak camera, splits the beam and projects the image onto a reticle that is positioned to coincide with the image on the streak camera and is then locked into position. From this point on, aligning targets to the reticle is equivalent to aligning them to the streak camera slit. The alignment camera can also view the image of the target on the front of the streak camera slit. The alignment camera is equipped with Polaroid film packs for documentary photos of target alignment.

Targets are front- and back-illuminated for visible alignment with a band-pass-filtered mercury arc lamp (5461 Å) and lens and mirror system.

The x-ray backlighting is accomplished by focusing one of the laser beams onto a disk in back of the target during a shot to produce an x-ray source (Fig. 7).

The major component of the system consists of the x-ray microscope mirror which is mounted inside a manipulator on the Shiva chamber wall Fig. 7(b). This manipulator positions and points the x-ray mirror. A mechanism, mounted in the adjacent port to the x-ray microscope, inserts a tantalum shutter in front of the coaxial alignment lens; it also inserts numerous combinations of collimators, filters, blast shields, and a reflecting mirror.

The x-ray mirror is located 300 mm from the target, and the streak camera, or image plane, is located 6.9 m from the target. A vacuum line of sight joins the x-ray microscope to the streak camera which is mounted on a three-axis positioner. The alignment and streak cameras have their own complex vacuum systems that maintain a vacuum of 10^{-6} Torr.

The streak camera photocathode support foil is very fragile and can withstand only slight pressure differentials 5×10^{-2} Torr. A computer-controlled automated vacuum system controller now being constructed will cycle the system to and from atmosphere at a controlled rate, and will also interlock the valves, filter inserter, shutter mechanism, and pellicle to prevent damage to the diagnostics, target chamber, and vacuum system.

The x-ray backlighting system is now operating successfully on Shiva; Fig. 9 is a photograph recently taken during a shot. The target was a gold disk 600 μm in diameter and 15-μm thick. The disk was positioned normal to the laser beam and illuminated from one side only. The x-ray microscope and streak camera recorded the event viewing the edge of the disk. The horizontal direction on the photograph is the time axis and the vertical is the space axis.

In summary, the development of x-ray backlighting will aid in the study of the dynamics of laser fusion targets.

(For further information, contact M. W. Kobierecki, Ext. 2-5325, W. M. Ploeger, Ext. 2-5386, W. B. Laird, Ext. 2-5923, A. Coppabianca, Ext. 2-5377, or J. A. Zickuhr, Ext. 2-5350.)

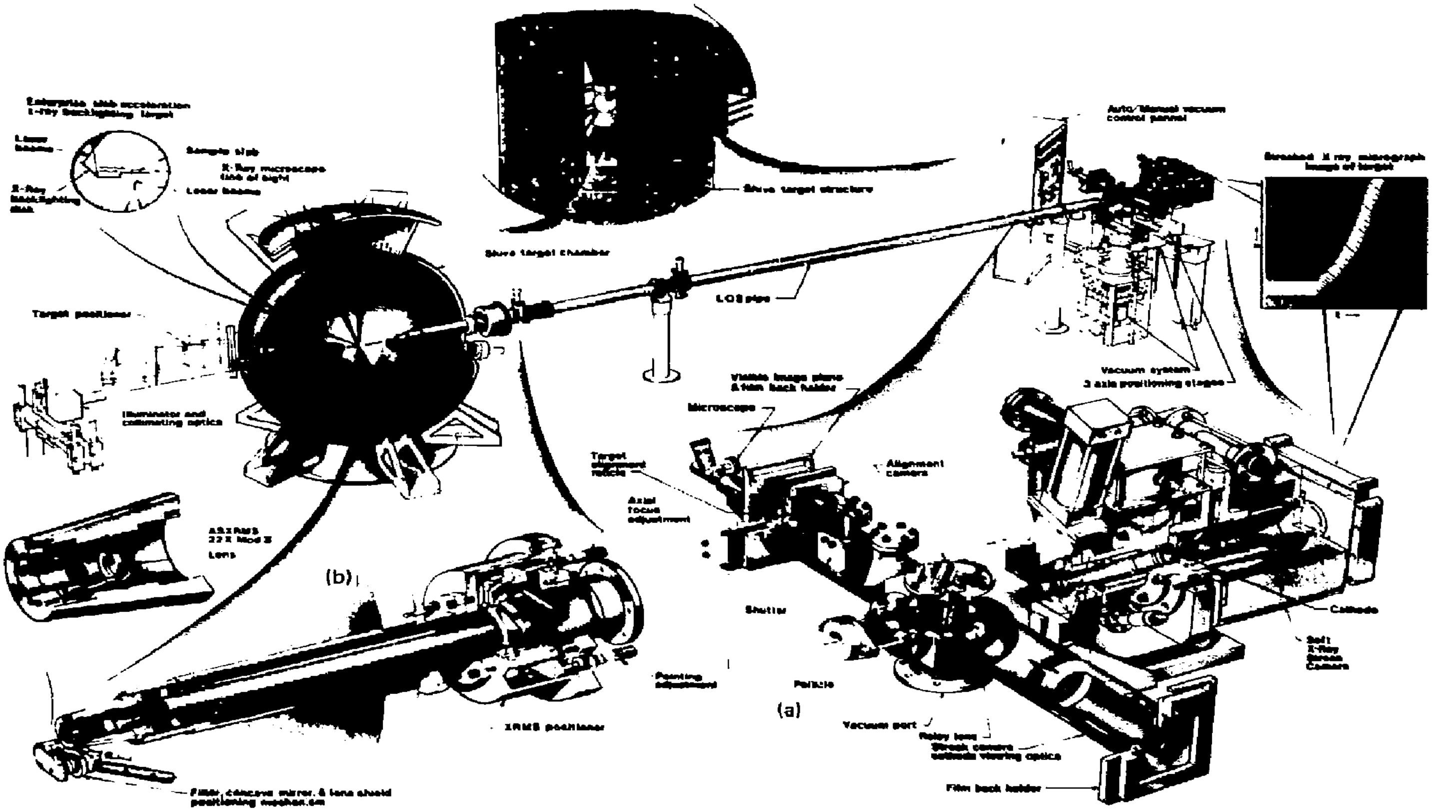

FIG. 7. The target room configuration for the Shiva backlighting system.

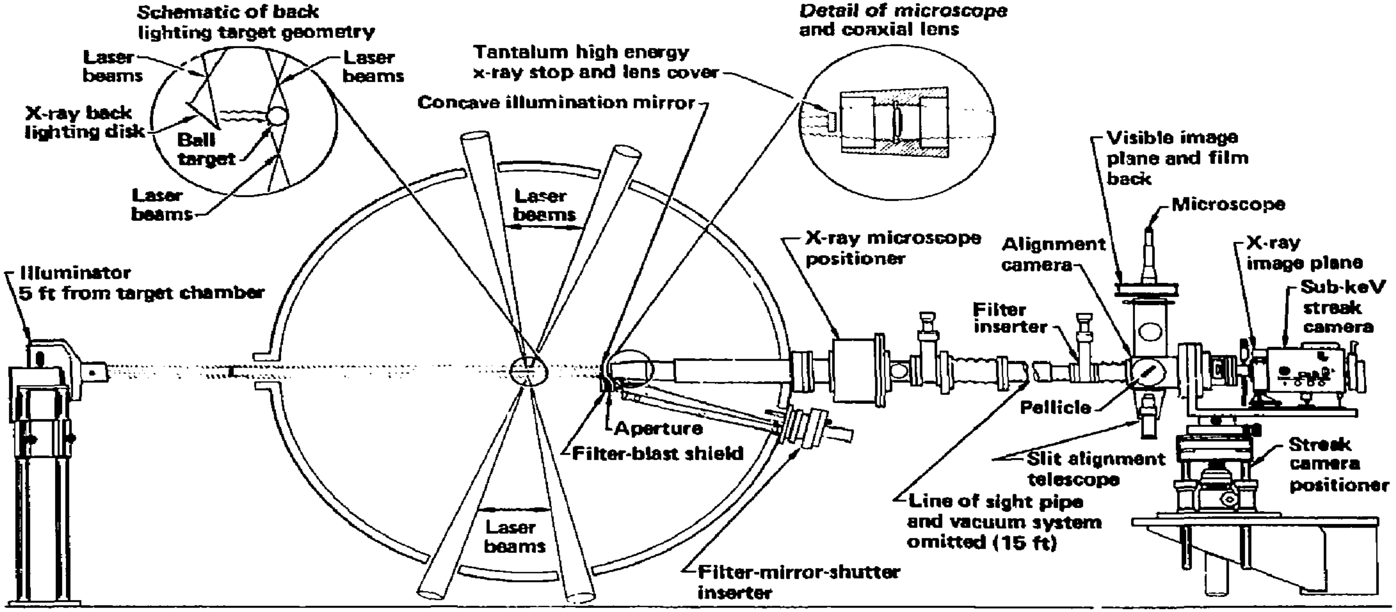

FIG. 8. Schematic of the Shiva backlighting system.

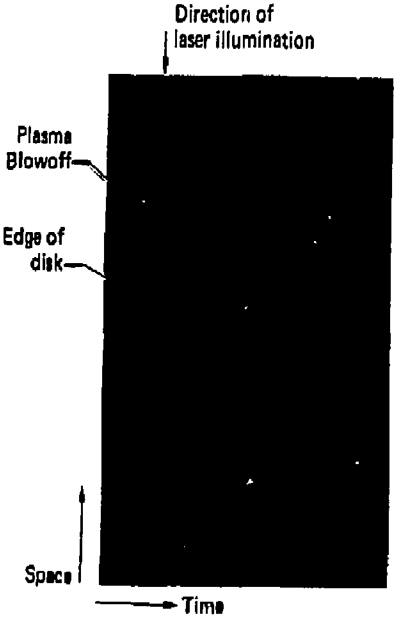

FIG. 9. A streaked x-ray micrograph image of a disk target.

Integrated Dye Flow System for LIS Program Dye Lasers

A major goal of LLNL's Laser Isotope Separation (LIS) Program is to develop large-scale economic laser processes to enrich uranium for use as light water reactor fuel. Tunable dye lasers are powerful tools in the development of isotopically selective photoionization methods. In order to better understand these processes, we desire dye lasers that maintain a constant spectral output for long periods of time so that data can be obtained under steady conditions.

Dye lasers are devices that produce coherent tunable light (see Fig. 10). A dye laser consists of a fluorescent dye, carrier solvent, dye cell, optical resonator, wavelength tuning optics, dye fluid pumping system, and dye optical pumping system. The fluorescent dyes have a broad optical absorption band and an equally broad optical emission band shifted to longer wavelength. Common dyes are Rhodamine, Kiton red, and Coumarin. These

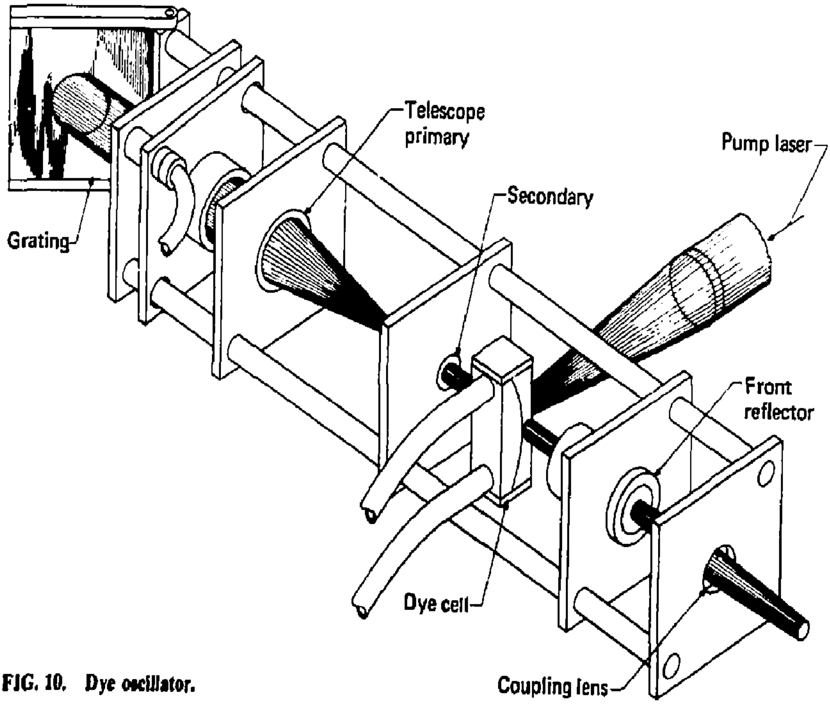

FIG. 10. Dye oscillator.

materials are commonly used in "day glow paints," cosmetic coloring, and cloth dyes. To function as a laser, the dye must be mixed with a solvent (alcohol, water, etc.) and pumped through an optical cell. The cell must be placed in an optical cavity, usually consisting of an output mirror on one side and an optical grating on the other side. Dye laser emission is then accomplished by optically pumping the dye in its absorption band with sufficient energy to stimulate emission.

To function adequately, these lasers must be mechanically stable and well damped. The most variable elements in the system are the dye cell and dye-solvent. The dye cell geometry is designed to contain the dye-solvent in a well-defined optical configuration. The remaining parameter in effective laser operation is the dye-solvent temperature control. While the dye-solvent is in the optical axis, small temperature changes will change the laser wavelength. This change has a deleterious effect on the experiment in progress. This report describes a cost-effective method of providing precise temperature control for a variety of lasers in our main facility.

Dye Flow System

As indicated in Fig. 11, dye is circulated from the reservoir through the flush valve by the pump which directs it to the reheater temperature control (±0.05°C). From there the dye goes through the filter, visual flow meter, laser interlock flow switch, and the dye cell. The dye then returns to the reservoir. In the main system, eight lasers are supplied by eight pumping units (duplicates). Primary temperature control is provided by one chiller of 60 Btu/min at 20°C. The water from this chiller is pumped to eight dye reservoir heat exchanger coils through a parallel flow circuit. The nominal performance in the dye is ±0.5°C for the primary loop. Secondary temperature control for the oscillators is provided by a 100-W cal-rod reheater and a "YSI" thermistor probe in each respective dye loop.

The thermistor temperature probe is mounted in the dye stream adjacent to and downstream from the cal-rod reheater. A temperature monitor probe is mounted in the supply line adjacent to the dye oscillator inside the lab. Fine temperature control of ± 0.05°C is achieved by reheating the dye to a set point using a sensitive Wheatstone bridge with the thermistor probe as the variable leg. This commercial unit, YSI No. 74, will switch the heater on-off with a 0.03°C sensitivity. This results in 0.05°C control in each dye loop it is packed in.

Flow rate is controlled by a bypass valve from the pump output to the reservoir. To prevent contamination of the solvent and premature degradation of the dye, the entire system is fabricated from stainless steel tubing except elastomer seals which are silicone or Teflon. Particulates in the dye contribute to poor laser performance by causing light scattering. One micrometre absolute filtration with 100% Teflon construction is provided by disposable millipore filters.

When the dye is being replaced, the system is kept clean by using filtered compressed air to flush all dye into the reservoir by closing the flush and bypass valves. Air is then injected through the quick

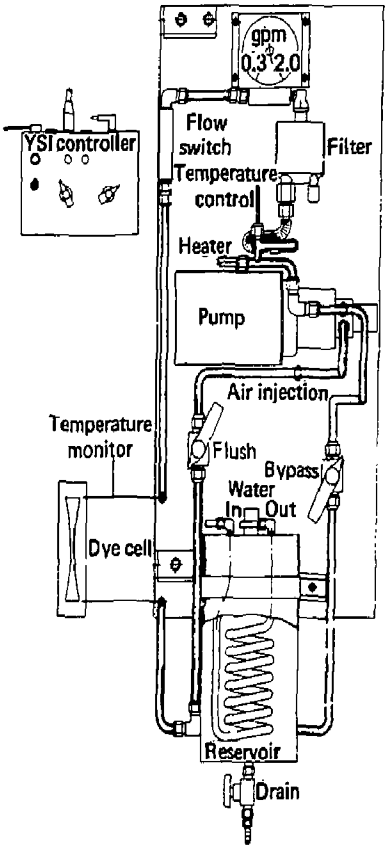

FIG. 11. Flow system.

disconnect valve. This purges the entire system downstream from the pump. Gravity will drain the rest of the fluid into the reservoir. A drain valve will drain the reservoir. A fill port is provided on top of the reservoir.

Two key lock "local/remote" control stations energize the pumps individually from adjacent the pumping plant or at the laser control rack inside the laboratory. Since the dye solvent must be flowing to prevent damage to the dye cell, a flow switch interlock shutters the pump beam to its respective cell when flow is inadequate.

This system currently is in operation on a routine basis. As a result of this integrated flow system, wavelength drifts are within the limits that can be servo-controlled with automated subsystems attached to the individual lasers.

(For further information contact J. C. Kuklo, Ext. 2-6025.)

Reference

1. C. A. Hurley, *Shiva Space Frame Earthquake Damage*, Lawrence Livermore National Laboratory, Livermore, CA, Rept. UCID-18644 (1980).

RESEARCH ENGINEERING DIVISION

The Research Engineering Division (RED) provides support in seven diversified areas.

Applied Energy Technology

We work closely with geothermal program personnel to solve energy-conversion system problems related to the effects of the high-temperature high-saline brine of the Salton Sea geothermal area.

In our solar program, we design, build, and test cost-competitive systems that may have industrial process heat application. A strong emphasis of our program is technology transfer.

For the *in situ* coal gasification project field experiments, RED is involved in subsurface drilling; instrumentation and logging; and the design, construction, and operation of a surface plant.

In the oil shale project, we are participating in laboratory testing and modeling of modified *in situ* and surface retorting of oil shale. The laboratory experiments require design, fabrication, and operation of retorts as large as 3 ft in diameter.

The spent fuel storage project is a field demonstration of the feasibility of storing spent reactor fuel assemblies underground in a deep granite formation. RED is involved in the underground site design, and in design of surface and subsurface equipment. Other aspects of this project include a Quality Assurance Program, and emplacement and retrieval of the fuel assemblies.

Biomedical and Environmental Research

For biomedical and environmental programs, RED contributes to research to detect, understand, and minimize the serious and long-term effects that technology may have on mankind and our environment.

High Energy Physics

We provide tools with which to pursue fundamental understanding of energy and matter. Technical support is provided for experiments performed at the 100-MeV electron linear accelerator (Linac), the RTNS II (rotation target neutron source), the insulating core transformer accelerator, the Van de Graaff accelerator, and the cyclotron.

Special Projects

RED has a small group working with Z-Division to support DOE's intelligence responsibility. Although this effort touches upon many topics of technical intelligence, the emphasis is on problems dealing with nuclear weapons and nuclear weapon proliferation.

Transportation

RED is providing technical assessment and planning support to DOE's Transportation Energy Conservation Division to assist in its research, development, and demonstration programs with emphasis in support of the electric and hybrid vehicle and the roadway-powered electric vehicle system.

Mechanical Energy Storage Technology

We are providing the planning and management as well as research and development for enhanced mechanical energy storage systems for both stationary and mobile (transportation) applications. Examples of the technology under consideration include flywheels, elastically deformed polymers, and compressed fluids.

Hazards Control

RED is participating with Hazards Control Department to assure the safety of laboratory personnel and facilities in the complex and diversified day-to-day activities at LLNL.

(For further information, contact T. Perlman, Ext. 2-1417.)

Prototype of an Ultrahigh-Speed Chromosome Flow Sorter Developed for Biomedical Use

The biochemical characterization of mammalian chromosomes is very advantageous to current cancer research. The processes of classification and sorting (separation) can be accomplished by "flow sorting." Basically, "flow sorting" consists of examining photometrically the laser-induced fluorescence given off by the dye-stained chromosomes as they are forced, one by one, in a liquid jet through a small nozzle (see Fig. 1). The nozzle orifice is typically 50 to 100 μm (0.002 to 0.004 in.) in diameter. After the fluorescence is measured, the liquid jet is broken into droplets at a given rate by the vibrating nozzle. Each droplet ideally contains

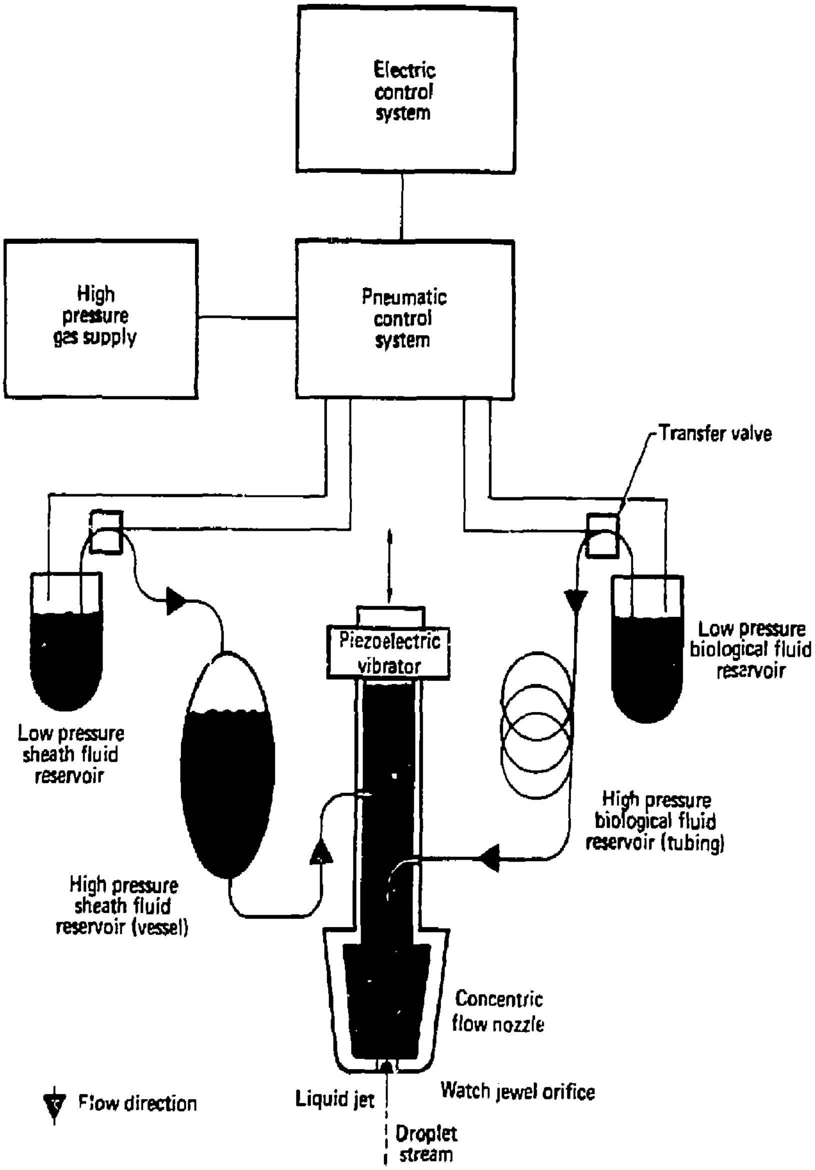

FIG. 1. Schematic system of the prototype ultrahigh-speed chromosome sorter.

no more than one chromosome. The droplets containing a desired chromosome type are given an electric charge just before separation from the jet. The desired chromosome is identified by the measured fluorescence. The charged droplets containing the desired chromosome type are deflected from the main droplet stream by passing through a strong electric field. The separated droplet stream is then collected.

The droplet production rate is a very important limiting factor in the sorting process. The total amount of collected material derived from such a sorting process is still extremely small, but large compared to that attainable two decades ago. Our objective was to add a very significant order of magnitude to the researcher's capability. In this effort we have succeeded in substantially increasing the droplet production rate. Existing commercial apparatus operates typically at 30 kHz and 15 psig, driving frequency (droplet production) and pressure, respectively. Prior LLNL work (ca 1978) by Alger extended this to 250 kHz and 150 psig. Present comparable attainment is 700 kHz and 800 psig (see Fig. 2). The original modest goal of 500 kHz and 600 psig has been exceeded. This achievement is not necessarily a limit. A thorough study of limiting nozzle parameters is under way. The present study has shown the importance of sharp-edged nozzle orifices as opposed to slowly changing transitions.

The simplified schematic of Fig. 1 shows the basic system without the detailed engineering advances incorporated in materials and control parameters. In essence the biological fluid and the sheath fluid are transferred from low pressure systems to the high pressure systems and are injected into a newly designed concentric flow nozzle from which the jet stream and droplets are ejected.

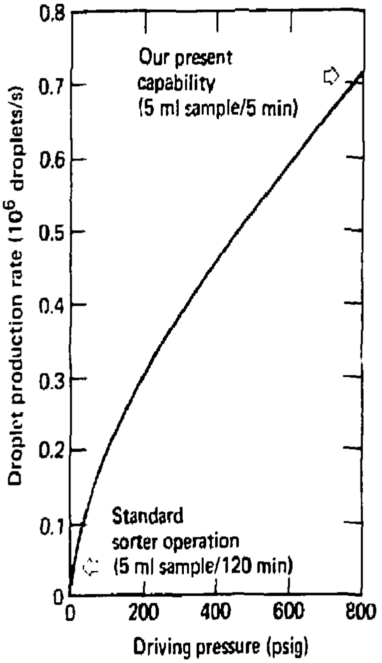

FIG. 2. **Maximum droplet production rate versus driving pressure for a 50-μm nozzle.**

The physical system is shown in Fig. 3. The solid-state electronic control and digital pressure measurement system is on the right side of the console. The pneumatic and hydraulic apparatus of Fig. 1 is on the left side of the console. On the right tabletop is the low-light-level video camera and on the left tabletop is the acoustically modulated laser. These two, in concert, stroboscopically image the droplets on the TV monitor located on top of the console. The electronics that drive the piezoelectric vibrator and the strobe system are located under the laser table along with other auxiliary equipment.

(For further information, contact D. E. Lord, Ext. 2-1270, or L. E. Marsh, Ext. 2-5608.)

Steel Reinforcing Bar Can Serve as a Temperature, Gas Flow, and Rubble Density Sensor for *In-Situ* Fossil Fuel Extraction Control

Problems affecting conventional thermocouple temperature monitoring of large volumes of oil shale or buried coal deposits can be overcome and additional multifaceted data acquired with a new approach using steel reinforcing bar (rebar). A compact, extremely strong configuration of multiple, nested "hairpins" (Fig. 4) made of ordinary steel rebar provides an economic answer to process control by monitoring temperature, gas flow, and rubble density for *in-situ* processing. The measurements are made by monitoring changes in electrical resistance caused by heating and/or cooling of steel rebar segments. Resistance measurements can be transformed into temperature measurements by means of the resistivity versus temperature curve for carbon steel. The resistance of an individual segment is measured by subtracting the resistance of the next shorter one from the longer. The resistance measurements are made using conventional electric bridge technology (Fig. 5).

Temperature Measurement and Comparison to Thermocouples

A favorable comparison to thermocouple data was obtained from a 1/60-scale model of the rebar

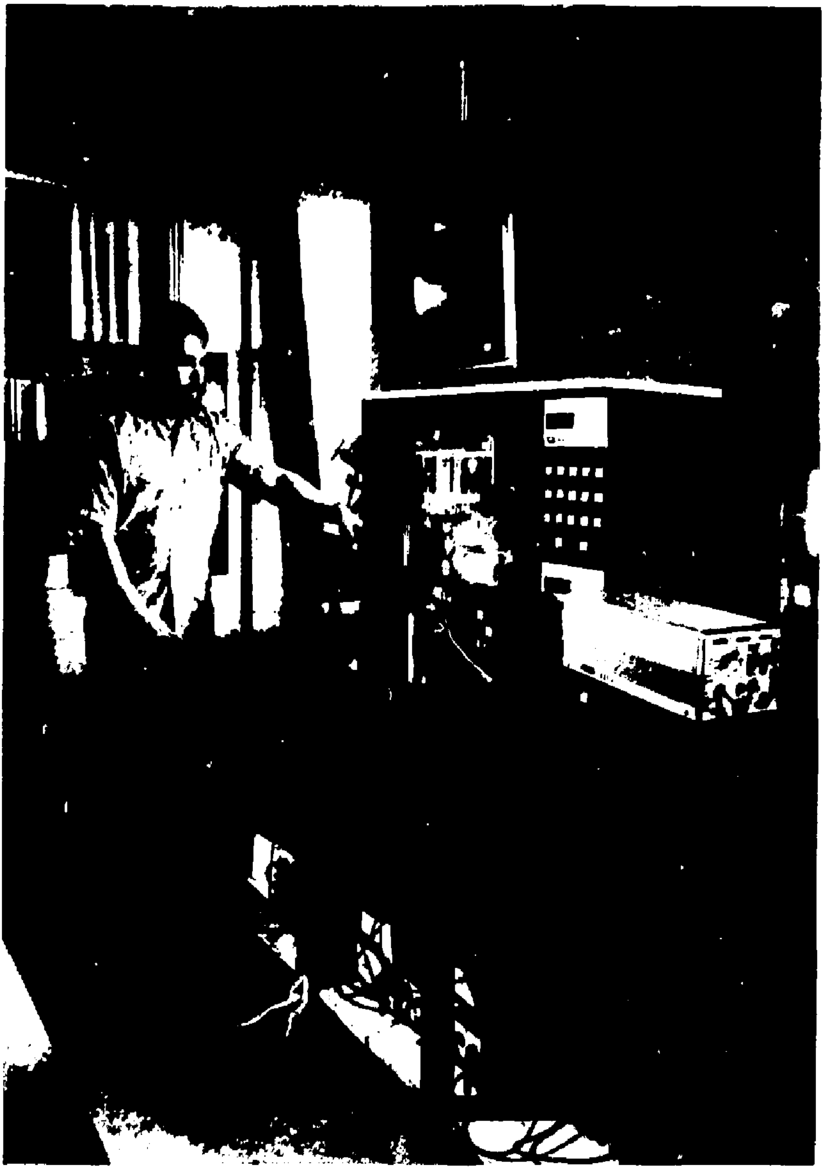

FIG. 3. The prototype ultrahigh-speed chromosome sorter.

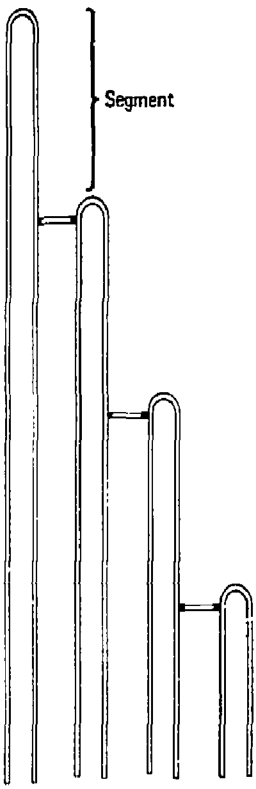

FIG. 4. Reinforcing bar hairpin array schematic.

system and associated equipment as shown in Fig. 6. Maximum differences were only a few percent from 100 to 1000°C. The temperature sensitivity of the rebar thermometer depends on the allowable sensing current. For example, in a 20-ft segment (40-ft length) of 3/8 in.-diam rebar, a pulsed 10-A current source produces a sensitivity of 2 mV/°C *with negligible self-heating. This is some* 40 times greater than the best thermocouple sensitivity without amplification. The cost of the rebar, depending on size, varies from 16 to 34¢/ft for a hairpin configuration of 3/8-to-3/4-in. diam, respectively, compared to sheathed thermocouples at about $1/ft. Since both systems would probably be grouted in place, the emplacement cost would be the same. The rebar system measures the average temperature over the segment length (perhaps 10 to *20 ft or more), whereas the thermocouple measures temperature essentially at a single point.* This single-point measurement is not desirable for highly insulating materials such as coal. The bar appears to have advantage where large volumes need monitor*ing. Also there are no electrical insulation failures* with the rebar.

Plans are underway to conduct tests on full-size arrays before actual emplacement in field experiments.

(For further information, contact D. E. Lord, Ext. 2-1270, or R. Ruiz, Ext. 2-7338.)

Water and Helium Flow Tests in Fractures of Climax Stock at the NTS

As part of the Waste Management Study, a radionuclide migration experiment is planned to characterize the flow capability of fractures in the Climax Stock granite at the Nevada Test Site (NTS). As a necessary preliminary to the radionuclide tracer test, a series of water and possibly helium flow tests are planned to evaluate fracture permeability and aperture width. These factors determine the suitability of a given fracture for use in the radionuclide tests.

The first task is to find a single recognizable *fracture intersecting two boreholes in the drift wall.* The fracture is isolated in each borehole by straddle packers. A water acceptance test will indicate water saturation of the fracture; pressure pulse tests will provide an estimate of fracture permeability and aperture width. These will be followed by a steady-state flow test on an acceptable fracture where water will be pressure-injected in the top borehole and a portion collected in the bottom one. During this fracture evaluation period, helium gas flow will be used if necessary to identify common fractures between the two boreholes, particularly those too *tightly closed to permit water passage.*

Description of the Basic System

The purpose of the system shown in Fig. 7 is to inject particulate-free (>0.1 μm) water into a tightly closed (10 μm) fracture extending through granite in the Climax Stock. It is also capable of helium injection and detection.

Required measurements are the flow of input water, flow of output water, input and output

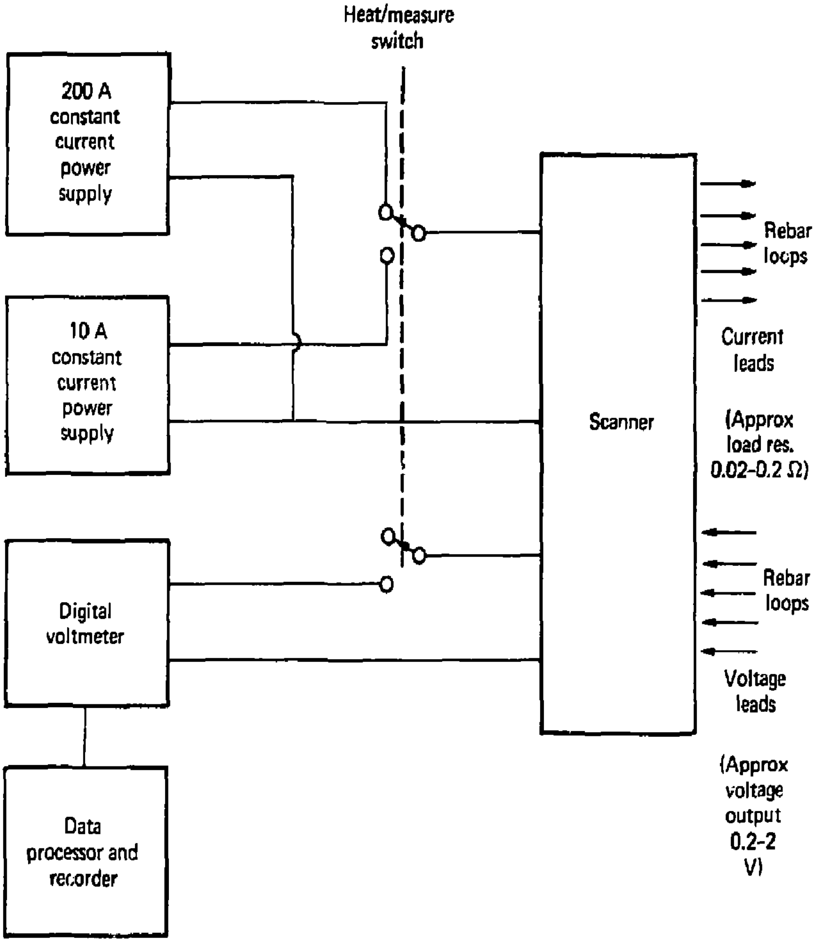

FIG. 5. Electrical configuration for 3/8-in.-diam, 20-ft-segment rebar loops. The 200-A supply can heat the rebar to 200°C in about 5 min. The 10-A supply provides 2 mV/°C sensitivity and a self-heating rate of 0.001°C/s.

pressure, and pressure in the trapped volume behind the packers.

Since the flow characteristics of a given fracture are not known beforehand, the system had to be designed to encompass a maximum range of pressures and flow rates. In this case, the maximum input pressure is 300 psi, limited primarily by the packer capability. The maximum flow rate is determined by the refill time of the pressure-injection bottles. It will vary depending on the residual bottle pressure from 1 gpm at low pressures (10 psi) to 0.2 gpm at the higher pressures (100+ psi).

Design Philosophy

The system has to operate in the Climax drift, some 1400 ft below the surface of the NTS. The drift has railroad tracks remaining from previous operations, so a rail cart seemed appropriate as an operations center. All components are mounted on

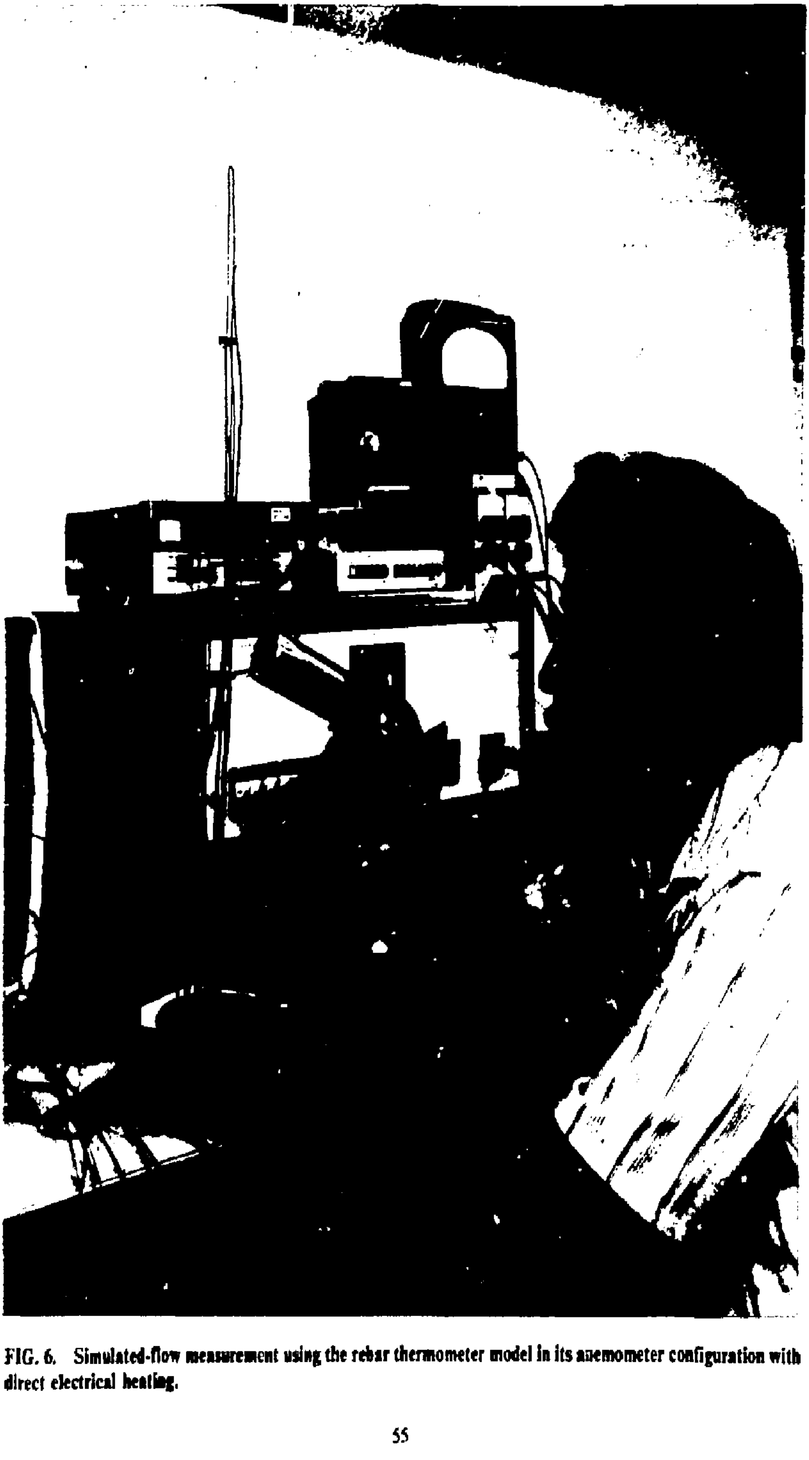

FIG. 6. Simulated-flow measurement using the rebar thermometer model in its anemometer configuration with direct electrical heating.

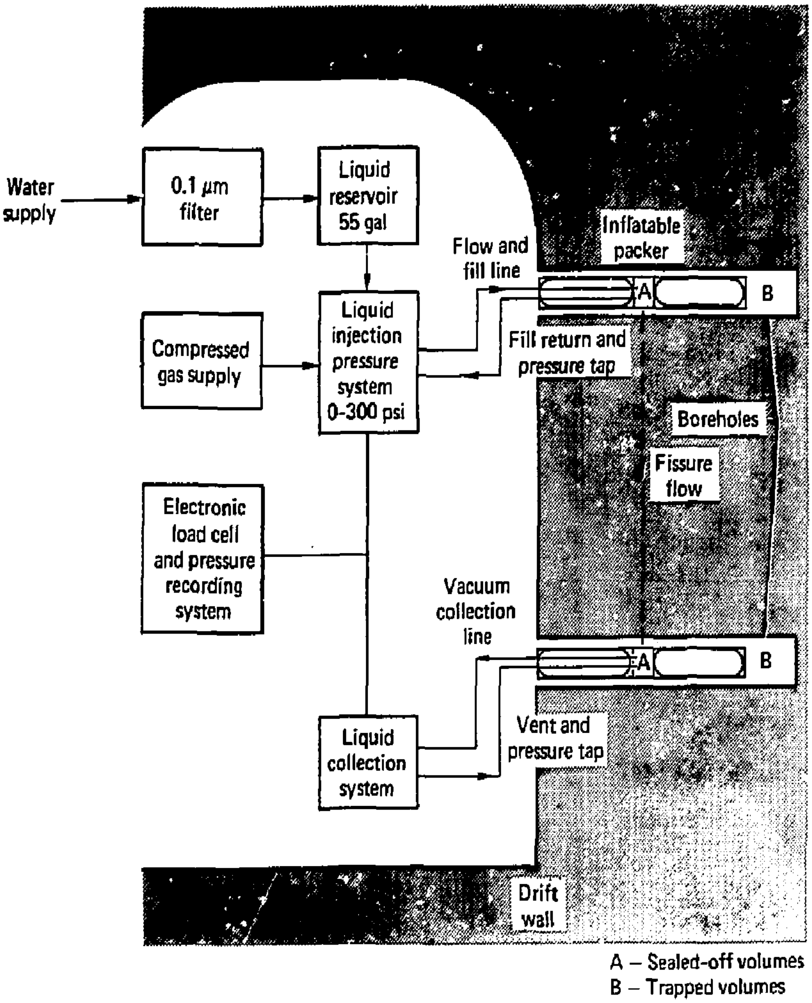

FIG. 7. System block diagram and measurements.

it (Figs. 8 and 9). There is limited volume access to the drift by elevator, so the system is modularly designed for minimum difficulty in transport and reassembly. Also because of the possibility of electrical power failure in the course of the flow experiment, the system is driven by conventional gas bottles as the pressure source. Air was chosen as the gas.

A pressure pulse input capability like "water hammer" is available for hydrokinetic analysis of the fracture's properties by establishing a flow into the input packer sealed-off volume and out of the pressure-tap tubing. This flow establishes a pressure drop of approximately one-half input pressure at the packer sealed-off volume. When the flow is suddenly stopped by the pressure-tap ball-valve, the

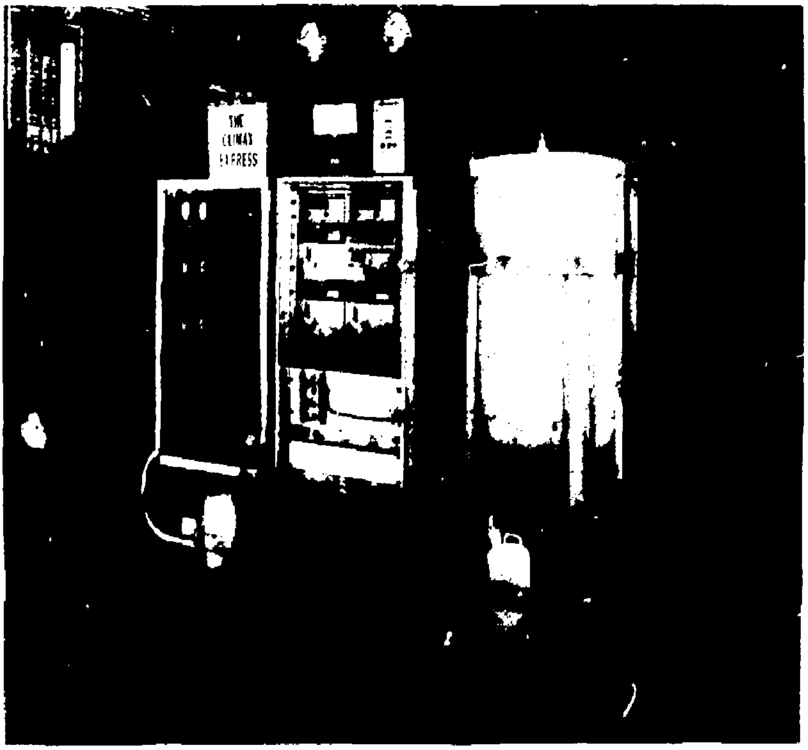

FIG. 8. Side view of the rail cart showing the pressure and flow control panel on the left, the electronic data indicating and recording console (with emergency lighting on the top), and the 55-gal water reservoir with filter on the right.

input-packer sealed-off volume pressure rises to the input pressure as fast as the acoustic wave can travel in the tubing-enclosed water (about 3 s). Liquid filling of the input-packer sealed-off volume is accomplished by this means also, without the sudden flow cut-off.

Collection of output liquid can be aided by a vacuum in the collection container. This vacuum is obtained from the roughing pump portion of the leak detector. In conjunction with the vacuum, opening the pressure tap to the atmosphere also provides a gas flow to aid water collection.

The trapped volumes behind each packer may be monitored for pressure and water presence. The top packer-trapped volume may be liquid-filled. These features are desirable to measure effects of interconnecting fractures and pulse effects. The system pressurizes the packers individually either pneumatically or hydraulically, up to 400 psig.

All controls are mechanical, and pressure gages are provided for monitoring and data purposes. The system is independent of electrical power except for the electronic data indicating and recording console. Because of nonelectric backup measurement systems, the experiment can continue even when the electronic module is not functioning.

Measurement System

The primary input flow measurement is accomplished by a continuous weight measurement, with respect to time, of the high pressure bottles as they are emptied. The total weight of bottle and water is measured by 50-lb strain gage type load cells.

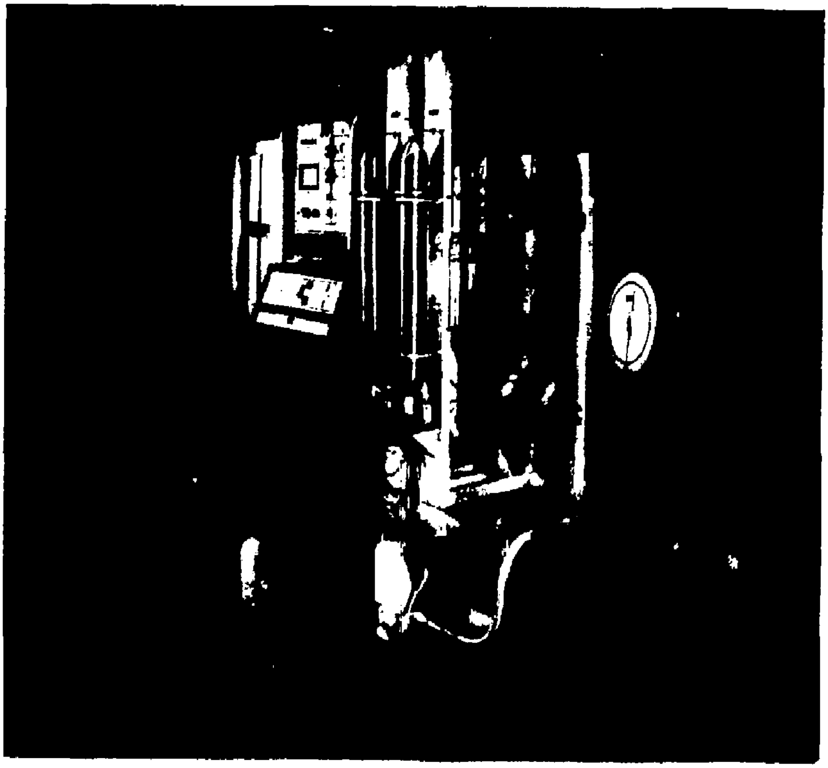

FIG. 9. The opposite side and front view of the rail cart showing the gas bottles mounted horizontally within the cart structure. The helium leak detector is left of center, and the water collection bottle and control panel are directly under the leak detector. The water injection bottles are mounted vertically to the right of the leak detector, and the Heise gage is mounted in the pressure control console at right.

Results are digitally recorded along with time, and mass flow is derived from this data.

A secondary flow measurement is available by reading the difference between system input and the packed-off volume pressures on the 12-in. Heise gage. This differential pressure reading can be calibrated in terms of volumetric flow.

A tertiary flow measurement is possible by timing the level changes in the 55-gal reservoir.

The output flow measurement is accomplished in like manner to the input measurement. The collected water is weighed by a strain gage type load cell. In this case the cell has a total 10-lb capacity. Provision for emptying the container periodically is available.

A backup flow method, timing level changes in the collection bottle, may be used.

Input pressure measurement is accomplished using Digiquartz digital pressure transducers. These model 2400 types have a full-scale range of 400 psia with a repeatability specification of 0.005%. Pressure and time parameters are recorded digitally and the continuous readout is digital.

Output pressures are handled similarly except that the transducers are sensimetric Model 971C strain gage types of 50-psia range. These have total error band specifications of 0.25%.

Transducers and load cells are calibrated by the LLNL calibration laboratory using standards traceable to the National Bureau of Standards.

Calibrations, in so far as possible, are done on total systems, i.e., transducer *and* readout system together.

(For further information, contact D. E. Lord, Ext. 2-1270, or P. W. Burklund, Ext. 2-7338.)

Cost of Seven Types of Electric Vehicles Analyzed

We have completed a study of the cost-effectiveness of electric vehicles for the Division of Electric & Hybrid Vehicles, Office of Transportation Programs, U.S. Department of Energy. In the analysis, several electric vehicle propulsion systems were computer-modeled. To identify the best systems, the cost and performance of the electric vehicles (EVs) with a normalized driving range of 100 mi were calculated and compared. The range capabilities of the vehicles were normalized to permit equitable comparisons beteeen the competing systems. The time period considered for the analysis is 1985.

A total of seven EV drivetrain systems were evaluated. They contained a variety of components, including dc and ac motors, continuously variable transmissions (CVT), and flywheels. The modeled drivetrains were:

1. dc drive without transmission (chain drive).
2. dc drive with 3-speed transmission.
3. dc drive with CVT.
4. ac drive with 3-speed transmission.
5. Parallel battery/flywheel with dc drive.
6. Parallel battery/flywheel with ac drive.
7. Series battery/flywheel with ac drive.

Each of the vehicle drivetrains were modeled with six different types of batteries. The battery types were:

1. Lead/acid.
2. Nickel/zinc.
3. Nickel/iron.
4. Sodium/sulfur (ceramic).
5. Zinc/chlorine.
6. Lithium/iron sulfide.

Of the battery types considered, only lead/acid is presently commercially available for use in electric vehicles. However, assuming research and developmental goals are met, prototypes of the other batteries should be available within the next five years. All of the alternate battery types have greater energy content than lead/acid, but at higher costs.

The analysis showed lowest vehicle costs for the dc drivetrain with CVT. The battery/flywheel vehicles were significantly more costly than the battery-only EVs, but the flywheel provided superior performance. Of the battery/flywheel systems evaluated, the lowest costs were obtained with the series configuration with ac drive. Block diagrams of these two drivetrains are shown in Figs. 10 and 11. For brevity, the other drivetrain configurations are not discussed here. In all cases, the EVs are designed to carry four passengers.

In the battery-only drivetrain shown (Fig. 10), the motor is allowed to idle at 2500 rpm when the vehicle is not in motion. This permits a reduction in the cost and complexity of the motor speed controller, since it eliminates the need for a voltage controller in the armature circuit. In this system, speed control is accomplished through a combination of the CVT and a voltage controller in the field circuit. The modeled CVT is a rolling contact drive design (cone toroidal type) which provides a continuously variable gear ratio from 1:1 to about 9:1.[1] The desired gear ratio is determined with an on-board microprocessor. The clutch shown in the diagram is

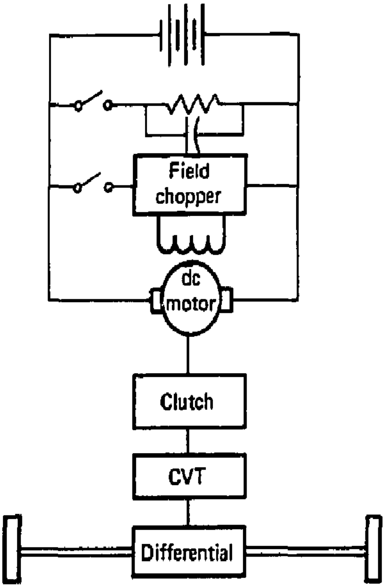

FIG. 10. Drivetrain with the dc drive and CVT.

used only to disengage the drivetrain when the vehicle is not in motion. Other CVT designs are possible which will permit an idle mode and thus eliminate the need for the clutch.[2]

In the battery/flywheel system shown (Fig. 11), propulsion comes from a combination of the motor and/or flywheel. The flywheel provides power during vehicle accelerations and stores energy during braking for later reuse. The motor provides power during steady cruise and replaces energy consumed in the flywheel rundown losses. Because the power requirements for steady cruise are much lower than those for accelerations, this motor can be smaller than that needed in a battery-only EV. Thus, the flywheel can improve vehicle performance without increasing vehicle weight.

The results of the performance and cost calculations for the foregoing drivetrain configurations are summarized in Table 1. Since the acceleration performance of a battery/flywheel vehicle is essentially limited only by the power rating of the flywheel, the acceleration capability is assumed constant in all cases for the battery/flywheel configuration. For the battery-only configuration, the acceleration performance depends upon the available battery power and total vehicle weight. For both the battery-only and battery/flywheel designs, the maximum vehicle speed is 65 mph. In each case, the cost data are shown relative to a typical four-passenger gasoline-powered automobile with performance capability similar to today's compacts (0 to 30 mph in 6 s). The life-cycle costs for the gasoline vehicle assume a gasoline cost of $1.25/gal in constant 1979 dollars.

Although not shown in Table 1, similar results were also obtained for the other drivetrain configurations. From such results, we conclude that for the 100-mi-range requirement, the most promising of the battery types evaluated are nickel/zinc, nickel/iron, and sodium/sulfur. In most cases, the nickel/iron battery yielded lowest life-cycle costs and highest initial costs, whereas sodium/sulfur yielded lowest initial costs and highest life-cycle costs. Nickel/zinc provided a reasonable compromise with initial and life-cycle costs falling between the extremes exhibited by nickel/iron and sodium/sulfur. Nickel/zinc also provided the best performance in the battery-only EV. Lead/acid batteries were disregarded in the foregoing evaluations because none of the vehicles were able to meet the 100-mi-range requirement with this type of battery. This does not, however, imply that lead-acid batteries would not be desirable for vehicles with lower range requirements.

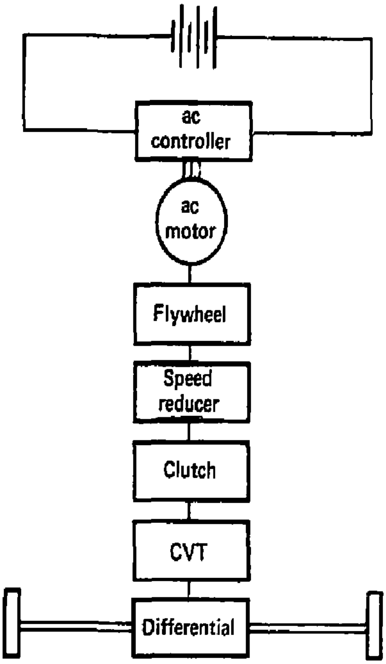

FIG. 11. The series battery/flywheel drivetrain with the ac drive.

Our overall conclusions are that electric vehicles can be built in the mid-1980s with a range capability of 100 mi and acceleration performance comparable to today's gasoline-powered compact automobiles. This assumes that current developmental goals are met in battery and other EV-component technologies. Because of production lead-time constraints, however, commercial versions of these vehicles may not be available until sometime beyond 1985. Due to the high cost of batteries, the initial cost of electric vehicles will be substantially greater than those for comparable gasoline-powered automobiles. But, because of lower fuel costs, the life-cycle costs for the EVs may be roughly equal to or lower than those for gasoline vehicles. The life-cycle cost comparison would, of

TABLE 1. Calculation results for two drivetrain configurations.

Battery *type*	Range[a] *(mi)*	Initial[b] *cost*	Life-[b,c] cycle *cost*	Δt (s) *0 to 30 mph*
Drivetrain with the dc drive and CVT				
Lead/acid	72	1.24	0.95	6.6
Nickel/zinc	100	1.46	1.12	5.7
Nickel/iron	100	1.57	0.97	6.2
Sodium/sulfur	100	1.30	1.29	7.3
Zinc/chlorine	100	1.43	1.14	7.6
Lithium/iron sulfide	100	1.45	1.12	7.2
Series battery/flywheel drivetrain with the ac drive				
Lead/acid	91	1.46	1.18	5.6
Nickel/zinc	100	1.69	1.33	5.6
Nickel/iron	100	1.67	1.16	5.6
Sodium/sulfur	100	1.49	1.49	5.6
Zinc/chlorine	100	1.67	1.42	5.6
Lithium/iron sulfide	100	1.72	1.40	5.6

[a] *Range at 80% battery discharge.*

[b] Costs are shown relative to a typical four-passenger gasoline-powered automobile with performance capability of 0 to 30 mph in 6.0 seconds.

[c] Life cycle cost for the baseline gasoline vehicle assumes a gasoline price of $1.25/gal (1979 dollars).

course, improve for the EV should gasoline prices continue to rise in the future.

(For further information, contact M. K. Kong, Ext. 2-6425.)

Test Facility Designed to Evaluate Roadway-Powered Electric Vehicle Systems

A variety of electric vehicle concepts are being studied by the Department of Energy in an effort to reduce this country's demand for petroleum. At present, most electric vehicles have a limited range because of the size and weight of their batteries. The Roadway-Powered Electric Vehicle (RPEV) system, where the vehicle obtains power from the road, is a possible solution to this problem. It is now being studied at LLNL. The concept was developed initially by the DOE at Lawrence Berkeley Laboratory (LBL) beginning in 1976. The power source in the road continuously provides adequate energy to the vehicle to permit good acceleration and velocity performance over the entire length of the powered roadway(s). The vehicle can move off the powered roadway by utilizing energy stored in its batteries. The energy stored on board the vehicles increases their operational flexibility by permitting driving on nonpowered roads, and reduces the number of powered roadways required.

Conceptual drawings of the system are shown in Figs. 12 and 13.

A feasibility study[3] published by LBL in 1977 indicates that an inductively coupled power system could satisfy the rigorous requirements of a freeway. It would be compatible with other types of automobiles, adaptable to electric vehicles of all sizes, accommodate operator skill variation, and it would be environmentally acceptable and result in no additional highway driving hazards.

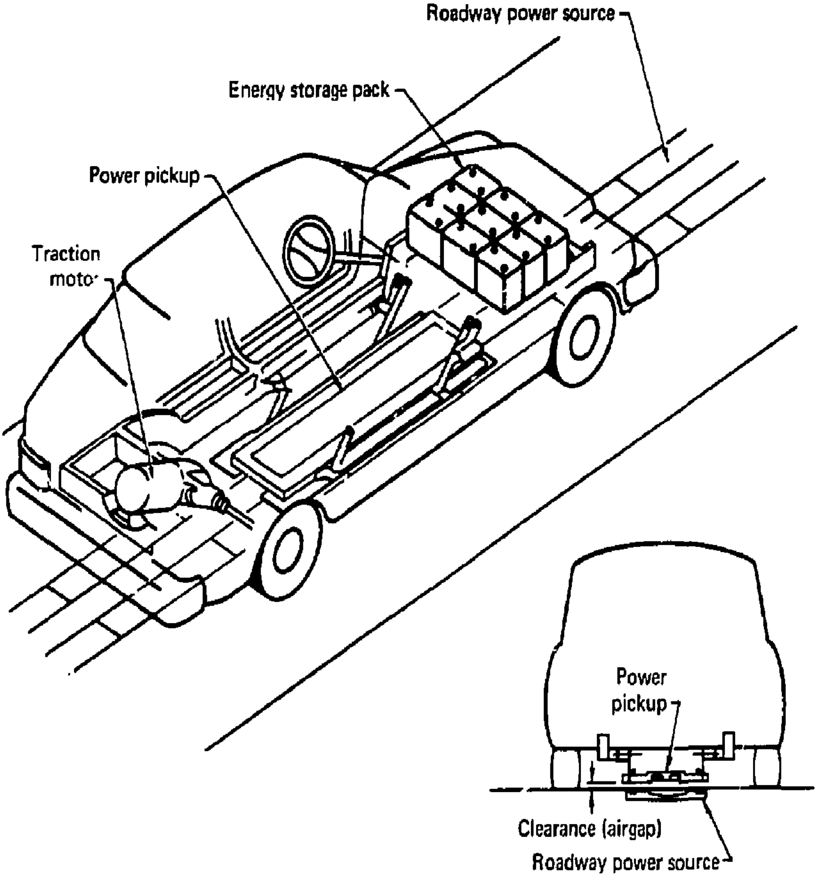

FIG. 12. **Roadway-powered electric vehicle system.**

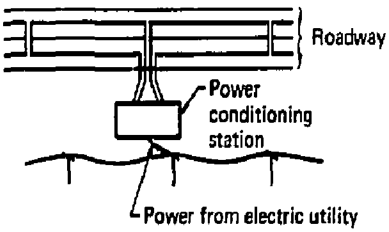

FIG. 13. **Powered highway system.**

Subsequent efforts at LBL investigated various roadway power system designs, emphasizing trade-offs involved in design optimization. Based on these efforts, a prototype power coupling system was designed. Static tests were conducted and the results were published in 1978.[4]

The results obtained from the static tests demonstrate the predictability and efficiency of the inductive power coupling mode. The next step in investigation of the RPEV system feasibility is to determine performance characteristics under dynamic operating conditions. The work begun at LBL was transferred to LLNL in 1979, where a dynamic test program is being conducted.

Currently, the RPEV project is sponsored at LLNL by the DOE, DOT, and Caltrans. This broad sponsorship is appropriate and necessary because highway construction and maintenance are the responsibility of federal and state transportation departments, and energy matters are the responsibility of the DOE. It is anticipated that other state and local agency transportation departments will become sponsors of this project in the future.

Dynamic Test Program

LLNL is presently charged with conducting an experimental program utilizing a modified electric vehicle on a section of powered roadway.[5,6] A test facility with a powered roadway was designed, and construction of the test track and shop building in the northeast corner of the Laboratory site is nearly complete. The facility includes a test track of powered and nonpowered roadway, an ac power source, an electric vehicle equipped with a pickup and batteries, and instrumentation and controls necessary to acquire test data under the dynamic conditions of the vehicle traveling on the roadway.

The overall length of the test track is 220 m, of which 50 m is powered. The test track is constructed of concrete 3.7-m wide to simulate a highway lane.

Power source core sections of the same design as those previously tested at LLNL are laid in a concrete slot formed in the roadway, and the height is adjusted to bring the source laminations flush with the surface of the roadway. This permits control of test parameters associated with measurement of the airgap between the road surface and the power pickup on the vehicle.

The source conductor consists of six insulated aluminum cables, connected in parallel, and placed in the slot formed by the source cores. A sectional view of this installation method is shown in Fig. 14.

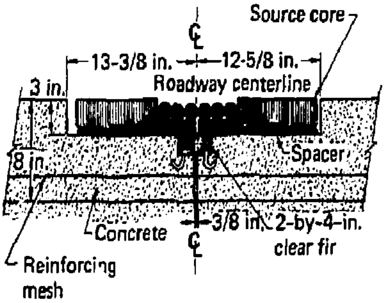

FIG. 14. Sectional view showing planned method of source core and conductor installation.

A motor-generator provides the loop voltage to sustain a desired source loop current in the range of 500 to 1000 A, at a frequency of 150 to 400 Hz. The loop current is monitored and the generator output is controlled by a source current controller. Compensation for the roadway's inductive load is provided by a source capacitor bank connected in parallel with the roadway loop.

The RPEV test vehicle is a modified 1969 Volkswagen. The vehicle is equipped with a 6-kW, series-wound dc-traction motor, a chopper controller, and eight 12-V traction batteries. A hand-operated pickup suspension system has been designed to raise and lower the power pickup. Space has been provided for electronic and electrical instrumentation.

The power pickup has been designed and is being procured. The pickup will have a cross section similar to that used in the static prototype, except that its windings will be made of aluminum instead of copper. Associated with the pickup winding is a capacitor compensation bank. Provision will be made to allow manual and automatic switching of various capacitor combinations across the winding. This will compensate for changing coupling characteristics caused by variations in airgap and lateral offsets to provide control over the pickup's output voltage.

The dynamic test program at LLNL addresses five areas:

- System characteristics.
- Power coupling capacity.
- Vehicle performance.
- Roadway compatibility.
- Safety.

The system characteristics test series provide a description of the magnetic, electrical, thermal, acoustic, and physical features of the dynamic test system. The power coupling capacity test series will be conducted to determine the peak power that can be coupled by means of the prototype source and pickup system. The vehicle performance test measures the vehicular steering/ride/performance characteristics off and on the powered roadway, and during engagement and disengagement from the powered roadway. The roadway compatibility test allows estimates of the operational and environmental differences caused by application of power to a roadway. Safety tests will provide information about the potential hazards introduced by application of power to the roadway. When dynamic test results are available, the direction of further system development can be decided by the sponsors.

Automobile Application Analysis

A number of studies and assessments comprising an overall RPEV Applications Analysis are being conducted to understand the benefits and problems associated with implementation of RPEV for the nation's automobile transportation system. These study areas are closely interrelated, and considerable feedback between individual study areas and technological developments is required.

Of early interest is determination of the impact of wide-scale implementation of RPEV on electric utility generating capacity and the potential petroleum savings. This information will be developed parametrically until market penetration studies can be conducted.

Initial test and study results are expected in the late summer.

(For further information, contact C. E. Walter, Ext. 2-1777.)

References

1. J. F. Kraus, "An Automotive CVT," in *Mechanical Engineering*, October 1976.
2. N. H. Benchly and A. A. Frank, *Continuously Variable Transmissions: Theory and Practice*, Lawrence Livermore National Laboratory, Livermore, CA, Rept. UCRL-15037 (1979).
3. J. G. Bolger and F. A. Kirsten, *Investigation of the Feasibility of a Dual Mode Electric Transportation System*, Lawrence Berkeley Laboratory Report LBL-6301 (1977).
4. J. G. Bolger, M. I. Green, L. S. Ng, and R. I. Wallace, *Test of the Performance and Characteristics of the Prototype Inductive Power Coupling for Electric Highway Systems*, Lawrence Berkeley Laboratory Report LBL-7522 (1978).
5. C. G. Dease and R. I. Wallace, *Roadway Powered Electric Vehicle (RPEV) System Project Implementation Plan/Schedule*, Lawrence Livermore National Laboratory, Livermore, CA, Rept. TSG 092679 (1979).
6. D. D. Davis, C. W. Dease, R. I. Wallace, and C. E. Walter, *Roadway Powered Electric Vehicle (RPEV) System*, Lawrence Livermore National Laboratory, Livermore, CA, Rept. UCRL-82662 (Preprint), February 1980 (Prepared for presentation at EV Expo '80, St. Louis, MO, May 20–22, 1980).

MATERIALS ENGINEERING DIVISION

The Materials Engineering Division (MED) provides complete technical services for engineering characterization of materials, and for inspection, evaluation, and proof-testing of complete systems. The Division has some 20 separate laboratories and facilities organized into sections responsible for specific technology areas.

The Materials Test and Evaluation Section provides mechanical testing—ASTM standard tests and special tests tailored to individual customer requirements. Developments in acoustic emission, fracture mechanics, high-rate response, and composite materials evaluation are major efforts.

Work in the Engineering Measurements Section ranges from calibration of a single transducer to fielding complete measurement systems. Service for the calibration and installation of transducers and accelerometers is available

The Nondestructive Evaluation Section provides quality-assurance services and engineering inspection for LLNL programs. Nondestructive evaluation is done with neutron, x-ray and gamma source radiography, ultrasonics, eddy current, dye penetrant, magnetic particle, and holographic techniques. Precision radiation gaging is available.

The Engineering Design Section designs and fabricates hardware in support of the Chemistry and Materials Science Department, the Earth Sciences Division, and MED itself. A major effort is support of the tritium facility operation.

The High Pressure Section provides the technology and facilities for conducting high-pressure gas and liquid experiments. The section is also responsible for providing certified tubing, valves, fittings, and miscellaneous hardware for tritium-handling systems.

The Computer System Applications Group has expertise ranging from the design and fielding of computer-based data acquisition and control systems to research on the mechanical response of complex structures. A major effort is support of the Weapons Division's environmental testing activities.

MED supports the Chemistry and Materials Science Department in its operation of the plutonium facility. MED has two objectives in this operation: (1) engineering design, fabrication and execution of testing in support of chemistry programs, and (2) weapons-program support by fabrication of device hardware and by doing engineering tests and evaluations.

(For further information, contact D. W. Moon, Ext. 2-8360.)

Precision Field Displacement Measurements

In the Argus Laser Bay, Building 381, measurement of three relative motions of the optical table with respect to Room 1544 was required over a period of hours and also over a period of minutes. The measurement problem was compounded by the fact that to obtain the relative motion between the optical table and Room 1544, we had to make two measurements from points 40 ft apart. Because of the structural arrangement of the optical table, it was physically impossible to make a direct measurement. Figure 1 shows the locations of the two measuring stations.

A review of the building design indicated that the hall could be treated as a monolithic structure over our required 40-ft span.

Displacement transducer systems were developed to measure the relative motions between the hall and the optical table and between the hall and Room 1544. To obtain relative movements of the optical table and Room 1544, a programmable data logger was used to record the data and reduce it to absolute motions between the reference point in Room 1544 and the reference point to the optical table.

Figure 2 indicates the location of each of the three displacement transducers at one station. The transducers are noncontacting sensors using eddy current principles. Each transducer has a 0.020-in. range with a resolution of better than 10 μin. Before the test, each transducer was calibrated in the Engineering Measurements Section Displacement Calibration Laboratory to determine individual sensitivity.

Long-term data (5 days) is presented in Fig. 3 indicating east-west motion between the two stations. Figure 4 shows fast scan data obtained on September 22, 1980.

(For further information, contact W. M. Shay, Jr., Ext. 2-7044, D. C. Gerigk, Ext. 2-6932, or A. W. Knabe, Ext. 2-9177.)

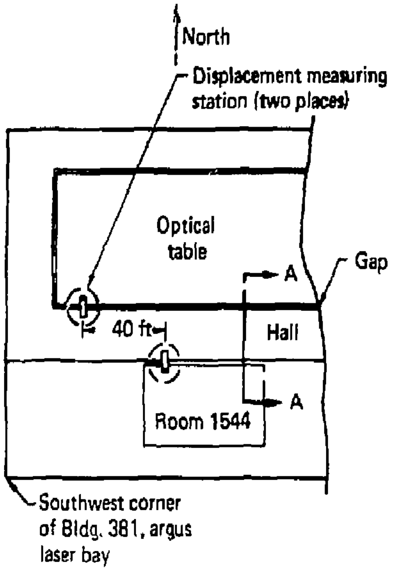

Plan view

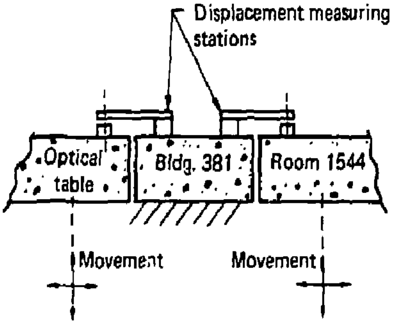

Section A-A

FIG. 1. **Displacement measuring station locations.**

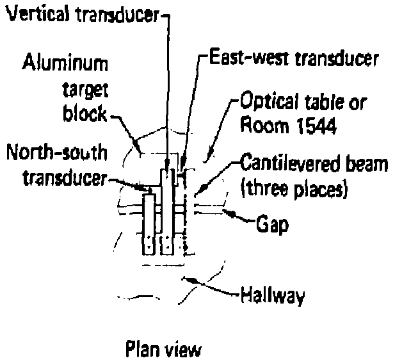

FIG. 2. **Detail of one of the displacement measuring stations.**

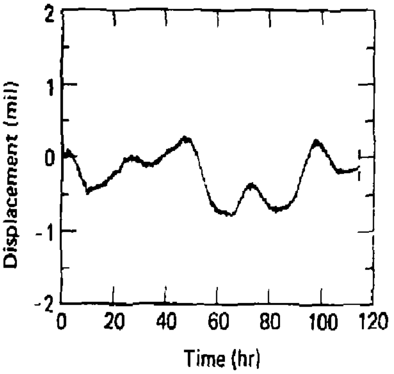

FIG. 3. **Argus laser room relative to Room 1544 (east-west measurement).**

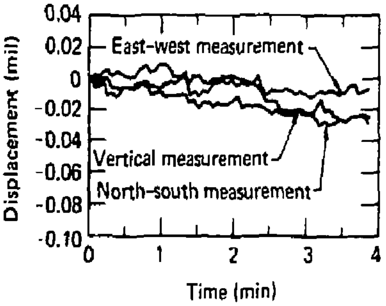

FIG. 4. **Argus laser bay relative to Room 1544 (fast scan, September 22, 1980).**

Unique Apparatus Designed for Tests on Wear of Tank Track Pads

The Materials Test & Evaluation Section along with the Thermal Physical Measurements Group is involved in a series of laboratory and field tests for the U.S. Army on T-142 tank pads.

The pads show premature wear at low mileage and the program is working to provide a failure model and solutions for this problem.

A unique piece of apparatus was designed and built to measure internal temperatures of tank pads (Fig. 5) during field testing at the Army Proving Grounds in Yuma, Arizona. The testing program includes such factors as tank speed, mileage, running time, and heat generation.

Two needles with thermocouples welded into the tips are actuated by air cylinders and injected into the pads. Then a reading is taken from temperature readouts. The depths of needles can be varied and different temperature gradients can be measured at various locations and depths on the pads.

This apparatus can be used for pavement, rough terrain, and cross-country testing.

(For further information, contact S. D. Santor, Ext. 2-7124.)

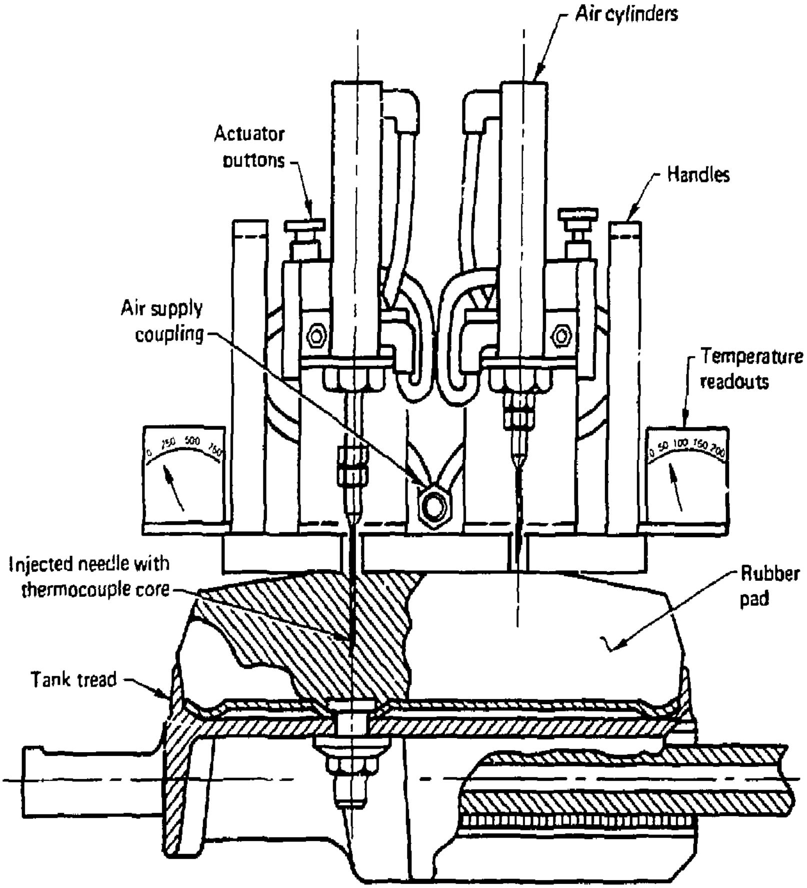

FIG. 5. Thermocouple injection apparatus.

High Explosive Actuator Ball Shutter Protects Shot Chamber's Optical Windows

A high explosive actuator ball shutter has been developed to protect the quartz windows in a 10-g shot chamber used for optical-laser experiments on detonating high explosives.

The overall objective of a study, which brought about the need for this explosive device, is to determine the Raman spectra of a detonating explosive. This requires pulsed-laser-beam access to the explosive through polished fused silica windows. As a result of the detonation, however, unprotected windows are damaged by shrapnel from the explosive assembly, rendering them useless for further tests.

It became necessary to design and test a new type high speed shutter to protect the quartz window (Fig. 6).

Experimental Design

Two fast "ball shutters" protect the quartz pressure windows in the operating sequence as follows: An SE-12 detonator in a chamber barrel propels a steel projectile, which then moves a lever connected by a shaft to a 1-1/4-in.-diam ball with an 11/16-diam hole through the center (Fig. 7). This action allows a pulsed-laser beam to pass unobstructed through the hole.

SE-12 detonators in the "gun barrels" were fired 951.4 μs before the 10-g PETN main charge was fired for application to our experiment. The

FIG. 6. Ball shutter assembly components.

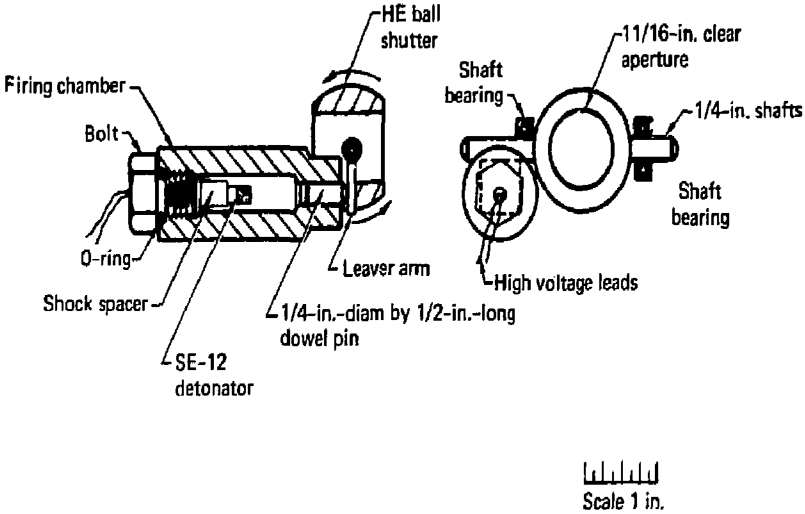

FIG. 7. Ball shutter schematic.

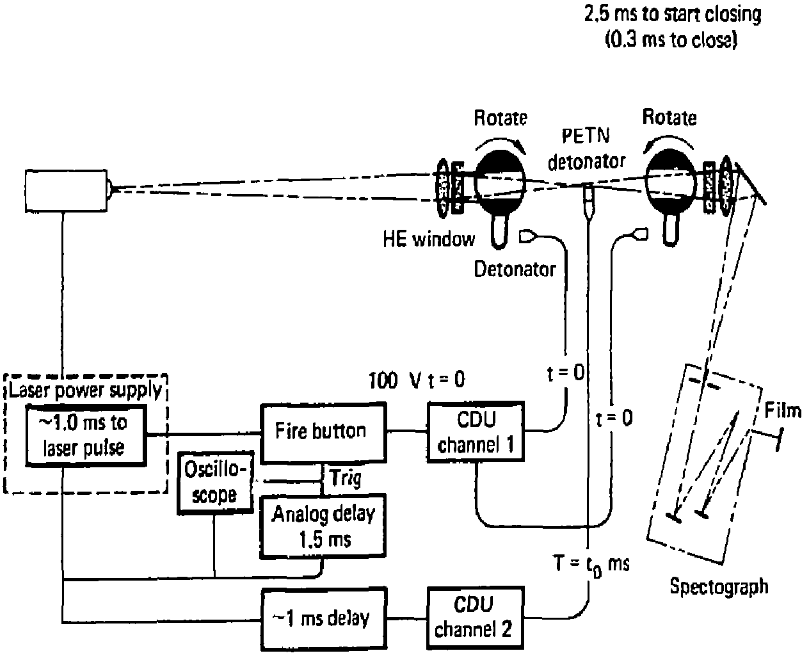

FIG. 8. High explosive ball shutter.

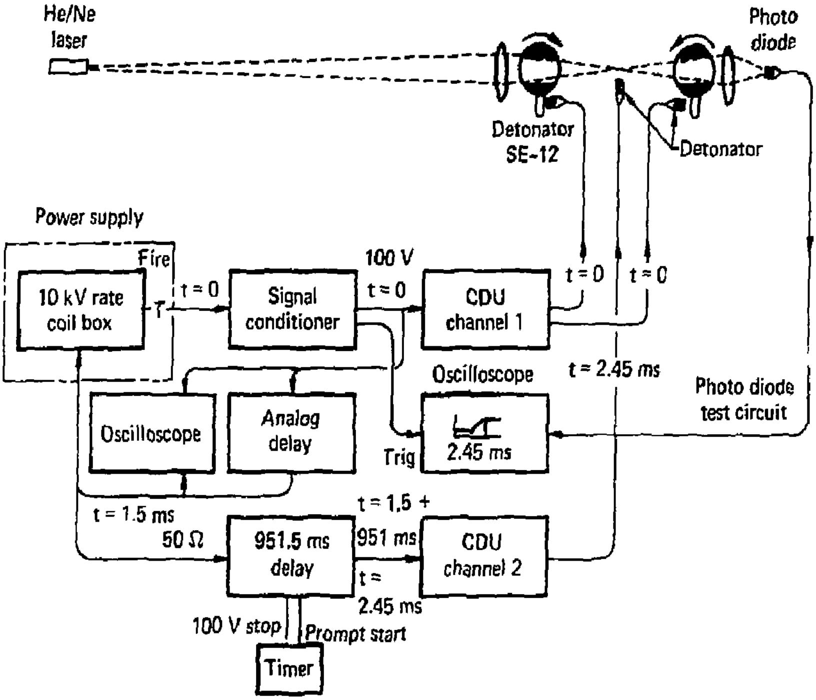

FIG. 9. Timing circuit ball shutter.

timing sequence (Fig. 8) shows that the laser pulses must be allowed to pass; this path is then closed off to fragments, thus protecting the optical windows.

The fast double-acting ball shutter was tested under experimental conditions in the 10-g chamber by passing a 1 mW helium-neon continuous-wave laser through the system and detecting the beam interruption caused by the closing shutters with a fast PIN diode circuit, as in Fig. 9. About 300 μs is required to completely close off the 11/16-in.-diam aperture of the ball shutter. In a further test, laser interrogating pulses passed through and the windows remained unharmed when the SE-12 detonator was fired (Fig. 10).

The detonation chambers and projectile are cleaned and reused again.

Conclusions

The ball shutters will protect optical windows from damage, thereby enabling optical access to small amounts of violently reacting or detonating materials (Fig. 11).

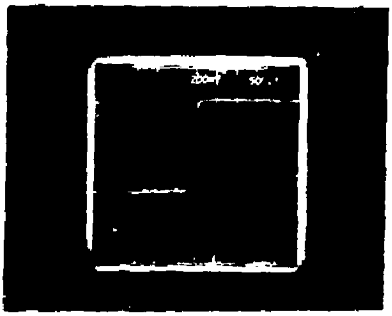

FIG. 10. The HE detonator takes 1.5 ms to start the ball to close, and 0.3 ms to completely close off the laser beam.

(For further information, contact R. A. McWilliams, Ext. 2-0544, or W. G. von Holle, Ext. 2-6326.)

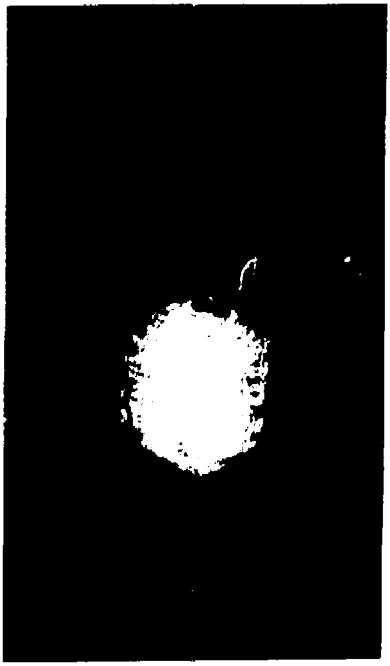

FIG. 11. Quartz window shattered by high-velocity hot particles from the HE detonator.

MAGNETIC FUSION ENGINEERING DIVISION

The Magnetic Fusion Engineering Division (MFED) supports LLNL's physics programs in three principal areas:

- Magnetic fusion energy (MFE) confinement experiments.
- MFE development and technology.
- Particle beam development.

Although the goals differ greatly, the three areas share a common technology base. Support is needed from virtually all mechanical engineering disciplines, as well as from engineers specializing in normal and superconducting magnetics, cryogenic systems, vacuum systems, and high-voltage components.

Our role in MFE confinement experiments is to provide the systems engineering, design, and fabrication of mechanical hardware. This research in the magnetic confinement of nuclear fusion reactions is expected to lead to tapping deuterium, an isotope of hydrogen present in sea water, as a nearly inexhaustible energy source. The major confinement experiments are the Tandem Mirror Experiment (TMX), Beta II (formerly 2XIIB), and the Mirror Fusion Test Facility (MFTF).

In MFE development and technology, our mission is to develop the technology base and engineering skills necessary to meet the future needs of magnetic confinement systems. Currently we have active programs in multifilamentary Nb_3Sn superconductor development, high-vacuum technology, neutral-beam source development, and fusion reactor studies. Basic research and development are emphasized to lay the groundwork for future fusion experiments

The particle beam development program, funded by the Defense Advanced Research Projects Agency (DARPA), involves building high-current, high-voltage, electron accelerators. Such accelerators are of interest in basic physics research and the weapons community. The present program calls for development of two accelerators, the Experimental Test Accelerator (ETA) and the Advanced Test Accelerator (ATA). The ETA program is the predecessor to ATA, and will generate the technology data base to build the 10-kA, 50-MeV ATA machine.

(For further information, contact D. K. Fisher, Ext. 2-6750.)

Tandem Mirror Fusion Test Facility Magnet System Has Exacting Structural and Thermal Requirements

In October 1980 the United States Congress approved a budget for expansion of the Lawrence Livermore National Laboratory's Mirror Fusion Test Facility (MFTF) to a tandem mirror facility designated MFTF-B (Fig. 1). The new facility, scheduled for completion in 1984, is expected to demonstrate energy "break even" capability (ratio of fusion energy to plasma heating energy) of mirror fusion and engineering feasibility of reactor-scale machines. Twenty-two superconducting magnets in a 12-m-diam by 64-m-long vacuum vessel (Fig. 2) will confine a fusion plasma fueled by 80 axial streaming plasma guns and over 40 radial neutral beams. Successful operation of the magnets requires thermal and structural designs to assure a stable superconducting state and to prevent unacceptable mechanical stresses.

Structural requirements for the magnet system include unique spatial constraints and materials restrictions to meet the operational needs of the unusual configuration. All of the magnets are liquid-helium cooled, which represents about 1500 t of structure at 4.5 K in the vacuum environment of the large vessel. Magnet support structures must satisfy complex load conditions, including electromagnetic (both normal operating and fault conditions) and seismically induced. Improved plasma confinement, characterized by long particle lifetimes, requires attention to coil alignment and minimizing field errors. Continued monitoring of field accuracy and possible adjustment during operation are contemplated.

Operating conditions for the magnet system include rapid cooldown and warm-up to minimize downtime for maintenance. Also, a short-time magnet surface temperature cycle is needed during regeneration of cryopumping surfaces. The magnets must be protected from plasma radiation and beam impingements by using appropriate shields. Neutrons and gamma radiation must also be sufficiently intercepted to protect the superconductors and other sensitive materials. Liquid nitrogen barriers must shield the magnets from room temperature radiation and conduction heat sources. Adequate liquid helium flow through the magnets is

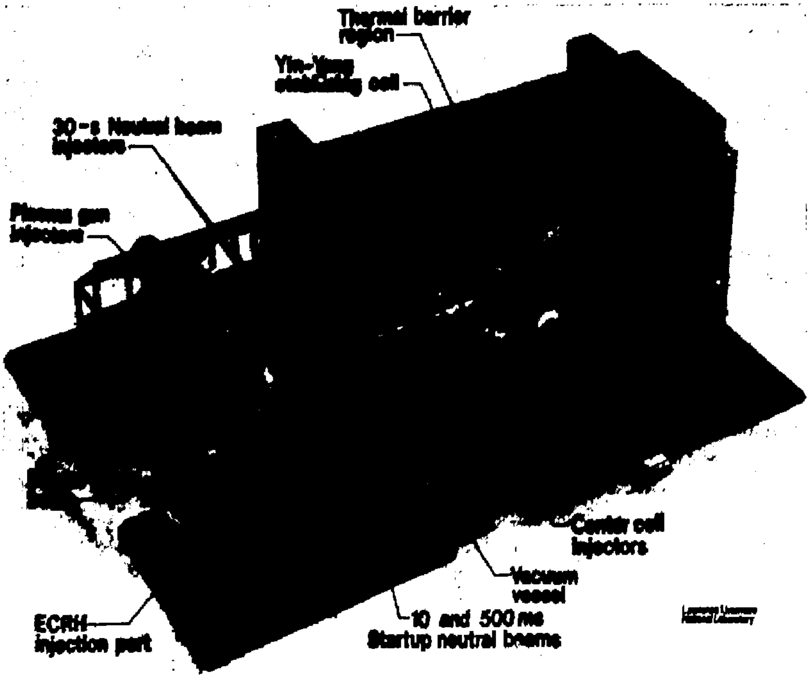

FIG. 1. The MFTF-B Tandem Mirror Facility.

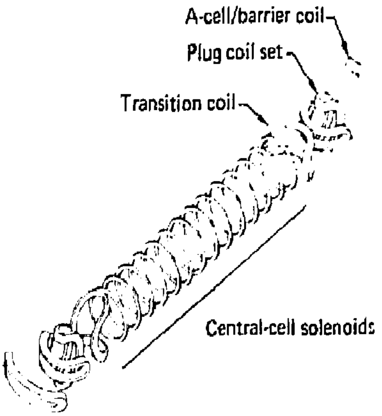

FIG. 2. MFTF-B magnet configuration.

required to maintain sufficient cooling of the superconductors in the presence of unavoidable heat sources. Moreover, the superconductor coil must be designed to inhibit helium vapor buildup. In the event of a magnet quench or fast dump, an adjacent magnet must withstand additional induced currents without adverse effects. Consequently, the superconductors must have properly selected materials and dimensions.

Cognizance of the thermal and structural behavior of a large superconducting system, such as will be in the MFTF-B, can be useful for evaluating future fusion reactors. The next step for mirror fusion development is expected to be a tandem mirror fusion reactor delivering net energy. Its basic geometry will probably be similar to the MFTF-B.

Consequently, present designs may be typical in future reactors.

(For further information, contact J. H. VanSant, Ext. 2-9890, or R. H. Bulmer, Ext. 2-1483.)

Superconducting Magnet Nearing Completion for Mirror Fusion Test Facility

Construction is progressing rapidly for Lawrence Livermore National Laboratory's advanced experimental magnetic fusion device, the Mirror Fusion Test Facility (MFTF). This facility could bring the U.S. closer to operational power-producing fusion reactors by the end of this century. The magnet for this $94.2-million research facility is expected to be operational in mid-1981. The MFTF will be a physics and engineering bridge between present experiments and future prototype reactors.

A major component of the MFTF is a superconducting yin-yang magnet with a 3.6-m magnetic well for plasma confinement. Several industries are involved, such as IGC and Airco for the superconductor production, General Dynamics-Convair Division for the thermal and structural design, Esco for the structural steel production, and CBI-Nuclear for the fabrication of the structural case.

The design stress for the magnet structure has been established at 80 ksi max (three-quarters of the 120 ksi yield of 304 LN at 4 K). The detailed design by General Dynamics was developed using finite-element analysis. The requirements for the MFTF established that the system have a 500 stress cycle capability. The combination of these factors makes this an ideal system for analysis by fracture mechanics.

The large, superconducting, 7.68-T yin-yang magnet for the MFTF is nearing completion. Both halves of the magnet have been wound and enclosed in a 316L stainless steel jacket. This 750 000-lb superconducting magnet embodies many unique features. The superconducting composite of copper with 480 niobium-titanium filaments is wrapped with a high-purity perforated and embossed copper strip. By incorporating careful process control, the many production problems related to fabrication of the superconductor were overcome. Button-on-a-string insulation was used between magnet turns, with perforated G-11 laminated plastic sheet between layers. Control of the insulation thickness, special clamps, and conductor tension were needed to keep the winding within the 0.005 in./layer design criterion and to limit conductor strain to 0.5%. Extensive tests in the conductor and joints confirmed a safety factor better than 3. Special 304LN stainless steel, with 0.14% nitrogen and low sulfur and phosphorus, was specified for the coil structure. The production material met the desired yield and tensile properties of 120 ksi and 180 ksi, respectively. Fracture toughness limited the design stress to 80 ksi, but the weld development program based on 316L-15 weld rod exceeded expectations. Qualification welds with low-ferrite materials produced toughness up to 183 ksi in., approaching that of the base metal.

(For further information, contact R. E. Hinkle, Ext. 2-0216, E. N. C. Dalder, Ext. 2-7270, or A. J. Hodges, Ext. 2-1470.)

Development Program Under Way for Niobium-Tin Superconductor

Multifilamentary niobium-titanium is a commercially available superconductor and is being used in the Magnetic Fusion Test Facility (MFTF) now under construction. However, niobium-titanium is limited to applications requiring fields of 9 T or less. The next generation of fusion facilities may require fields of up to 12 T, and niobium-tin (Nb_3Sn) is the material most likely to meet these needs. However, Nb_3Sn differs from niobium-titanium in two important respects. Niobium-tin is a strain-sensitive material that requires special handling and process design to prevent degradation of its superconducting properties. In addition, the matrix must be bronze, rather than high purity copper; this introduces an additional problem in developing a stabilized conductor, i.e., a conductor in which the current can transfer from the superconductor to the stabilizing copper in the event of a fault.

LLNL has been sponsoring a conductor development program in industry since 1974 to assure that a suitable Nb_3Sn superconductor will be available commercially and that sufficient design information exists so that Nb_3Sn will be an option in 1982.

Current Progress

Typical Nb_3Sn multifilamentary superconducting composites produced by the bronze diffusion process have repetitive fiber elements of niobium embedded in a bronze matrix, with an Nb_3Sn reaction zone serving as the interfacial layer between the two. Clusters of these units are surrounded by tin diffusion inhibitors, such as tantalum, and placed inside a second external copper matrix (Fig. 3). The strain degradation of the critical current density has been both analytically and experimentally investigated in an inversion of this configuration. The new geometry consists of bronze filament cores inside niobium tubes, with the usual Nb_3Sn interface (Figs. 4 and 5). Since the niobium acts as a diffusion barrier, copper can be directly utilized as the embedding matrix, eliminating the motivation for tantalum addition. Analytic results were obtained from a computer program (MAXIMSUPER) that evaluates the three-dimensional strain fields on the Nb_3Sn zones in a cylindrical repeating element of the composite. The strain fields are caused by both residual (thermal contraction) and applied axial loading. The code then incorporates the calculated Nb_3Sn strain values into appropriate scaling laws to predict the critical current density and its degradation with increasing axial strain.

Investigations were performed to ascertain additional information on the connection between the cubic to tetragonal martensitic phase transformation and the phenomenon of superconductivity in Nb_3Sn. Of particular interest is the degradation of the critical parameters, such as T_c, H_{c2}, and J_c, with mechanical straining of the superconductor. These studies yielded information that assisted in the derivation of the critical current-strain scaling laws just mentioned. Since martensitic transitions are also known to be strain sensitive, perhaps the structural change is directly responsible for the

FIG. 4. Cross section of an internal-bronze-core-geometry conductor showing the niobium-Nb_3Sn tubes inside an outer copper matrix. The magnification is 20X.

FIG. 3. Cross section of the MFTF magnet conductor showing 18 clusters of niobium filaments (16,000/cluster) in a bronze matrix, surrounded by tantalum barriers, and immerged in an outer copper matrix. The magnification is 10X.

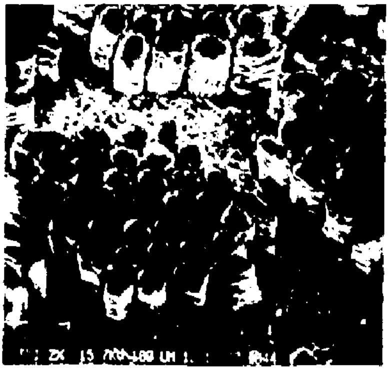

FIG. 5. Micrograph of the tubes shown in Fig. 2, with the bronze cores and outer copper matrix etched away to show enhanced details of the niobium-Nb_3Sn tubes. The magnification is 151X.

anomalous reduction in the superconducting properties of the material. Low temperature x-ray diffraction experiments were performed on Nb_3Sn ribbons (*in which the bronze layers had been etched off*) mounted to copper and indium sample stages. The cryostat has the unique feature that allows the superconductor to be placed under both compressive and tensile strains (while at low temperatures) by means of a vacuum mechanical insert. Results indicate that the martensitic phase transition temperature T_m increases with increasing compressive strains. Critical parameters, such as H_{c2} and T_c are thought to vary according to a two-level state model which expresses the Nb_3Sn cubic-to-tetragonal, martensitic-phase transformation as being strain sensitive.

Experimental investigations conducted with a 12 T, low temperature, tensile-test facility on both the niobium core and bronze core geometries confirm the importance of the tangential strains (in addition to the axial strain) on the critical current properties of the conductors. In particular, resulting higher radial and azimuthal strains yield lower critical current densities in the latter geometry. Under applied axial loading, the increasing tangential strains exhibit contradistinctive behavior from that of the axial z strain, which changes sign from compressive to tensile. The magnitude of these tangential strains depends primarily on the composite geometry and configuration. Good agreement between the MAXIMSUPER predictions and experimental results indicates that the program may be suitable for superconducting composite design applications.

(For further information, contact R. W. Hoard, Ext. 2-6729, or R. M. Scanlan, Ext. 2-7002.)

Engineering Design of a 40-kV Neutral-Beam Source

The 40-kV source for Lawrence Livermore National Laboratory's *Tandem Mirror Experiment* (TMX) is a mature design reflecting our experience both in manufacturing and maintaining of sources and in neutral-beam operation on test stands and fusion experiments. We have eight 40-kV modules in service and ten more 20-kV modules of this style under construction.

The accelerator section is built much like the original Lawrence Berkeley Laboratory source designed for the 2XIIB experiment (Ref. 1), with the following modifications:

- Grids are curved to spherical surfaces.
- The bulk of organic materials has been eliminated and what remains can be eliminated when required.
- The number of vacuum joints has been reduced.
- The structure is stiffened to facilitate measurement of the grids and to ensure stability throughout source life cycle.
- Beam-forming electrodes have been increased in size to enhance heat transfer and structural stability and to help locate these elements precisely.
- External voltage-holding properties are improved by careful attention to contours. The addition of a corona shield reduces electric fields around the accelerator and arc chamber.

General Description

Sections of the 40-kV, 40-A, TMX source are shown in Figs. 6(a) and 6(b). This module is comprised of the arc chamber and accelerator sections.

The source accelerator section uses a single rectangular insulator to perform three functions: providing voltage standoff, forming the supporting structure, and acting as the vacuum wall. Both machinable glass ceramic (Corning Macor^{TM}) and F.R.P. (Nema G-10) have been used for this insulator. In either case, the insulator is joined to the titanium base plate and extractor electrode by thermal-setting-epoxy adhesive. The parts are self-jigging; the bonding is done at 120 to 130°C under a load of 0.34 MPa (50 psi).

The beam-forming electrodes are made of roll-formed molybdenum for the extractor grid and tungsten (ground rod) for the accelerator and decelerator grids. The beam-forming electrodes are elastically bent by their mountings to conform to spherical surfaces for focusing on a target plasma at 3.2 m. Each electrode is free to expand independently of all others in response to thermal loading.

Formed molybdenum masks are used to cover structural members that cannot be contoured for voltage holding and to block back-streaming electrons between voltage levels in the accelerator.

Figure 7 shows the major structural members of the accelerating section. It includes, from left to

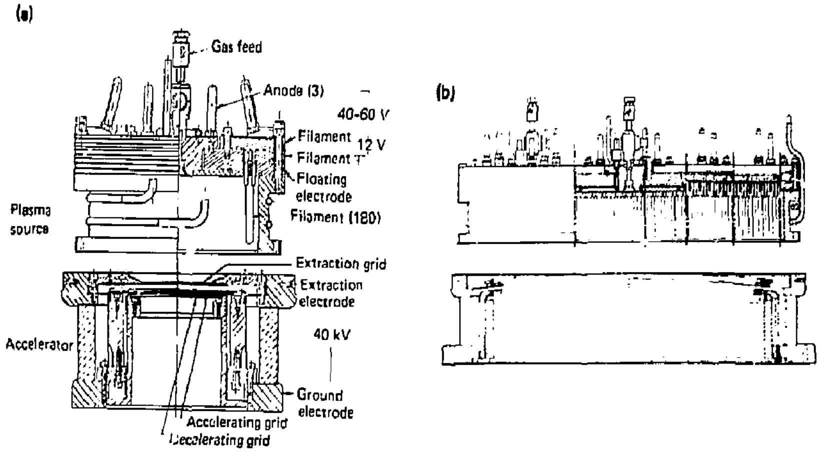

FIG. 6. (a) and (b) Sections through the TMX source.

FIG. 7. Major structural members.

right: an extraction-grid mounting rail; the extraction-grid plate with a mounting rail in place, but not bolted down to the curved mounting surface; a fully assembled accelerating grid on its hat (the hat mounts to the base plate by an insulator not shown); the decelerating grid, partially assembled on its hat, and, finally, the insulator stack.

Figure 8 is a photograph of the fully assembled accelerator section. This is our prototype. It is typical in all respects of the production models, except in the height of the insulator. The insulator is shorter because, at the time of assembly, we did not have a large enough piece of material. The active grid extraction area is 7 by 39 cm, transparency is 60%, and the outside dimensions are 58 by 21 cm. The spherical curvature of the extraction surface can be seen in this photograph; the extraction grid mounting rails are covered by radiation shields.

The arc chamber (described in Ref. 2) is modeled from the LBL design for TFTR. We scaled the LBL design down to match our smaller extraction area but operate at about 60% greater extraction current density ($J = 0.4\ \mathrm{A/cm^2}$) for a shorter pulse length ($T = 25$ ms).

The arc chamber's major structural members are copper; the three anode plates and the filament chucks are molybdenum. The arc chamber contains 180 tungsten hairpin filaments, and it is bolted to the accelerator section and O-ring sealed.

Figure 9 is a photograph of the complete neutral-beam source. This source, a production model, has the full-height insulator of Nema G-10. A corona shield is mounted at the extraction electrode and covers all but the back face of the arc chamber; its purpose is to smooth electric field contours around the arc chamber. The entire source is enclosed in a magnetic shield at ground potential when mounted on the TMX experimental vessel.

Steam Ejector-Condenser—Stage I of a Differential Vacuum Pumping Station

A steam ejector-condenser unit (Fig. 10) was built and tested to produce a 10-Torr vacuum with a 2-cm aperture to the atmosphere. This unit is the first stage of a differential vacuum pumping station

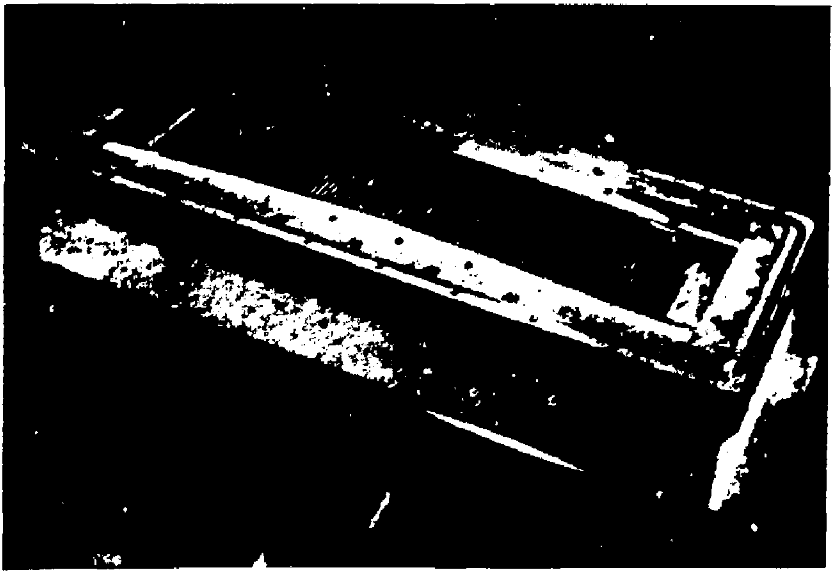

FIG. 8. [illegible]e assembled accelerator section.

---

[1] *For further information, contact T. J. Duffy, Ext. 2-1696.*

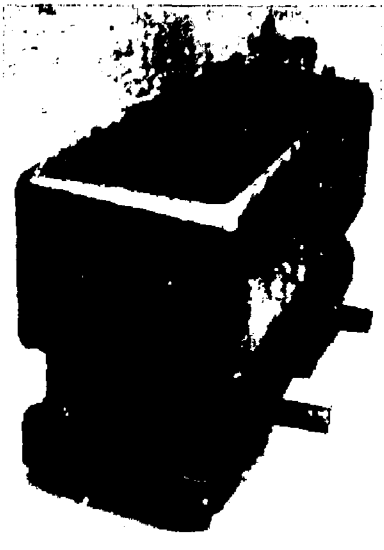

FIG. 9. The complete 40-kV source.

(see Fig. 11) that will be used with the Experimental Test Accelerator (ETA). The accelerator's electron beam will pass through a series of openings from a high vacuum (5×10^{-6} Torr) to the atmosphere. The differential system consists of four vacuum pumping units separated by low-conductance 2-cm-diam apertures to reduce the gas flow between stages. The steam ejector in the condenser vessel (Stage I) is open at its center to permit passage of the accelerator beam. The ejector exhausts into the condenser and forms a barrier of air flow into Stage II. This feature permits high-volume cold trapping and cryopumping of water vapor in the remaining lower-pressure stages II, III, and IV.

The steam is supplied to the ejector nozzles by a steam boiler and a superheater. The superheat minimizes the formation of liquid droplets as the vapor expands in the nozzles. The steam ejector was built with five nozzles mounted in a conical array with the center open for passage of the accelerator electron beam. The ejector produces a vacuum of 10 Torr and exhausts into the condenser, which is maintained at ≤70 Torr.

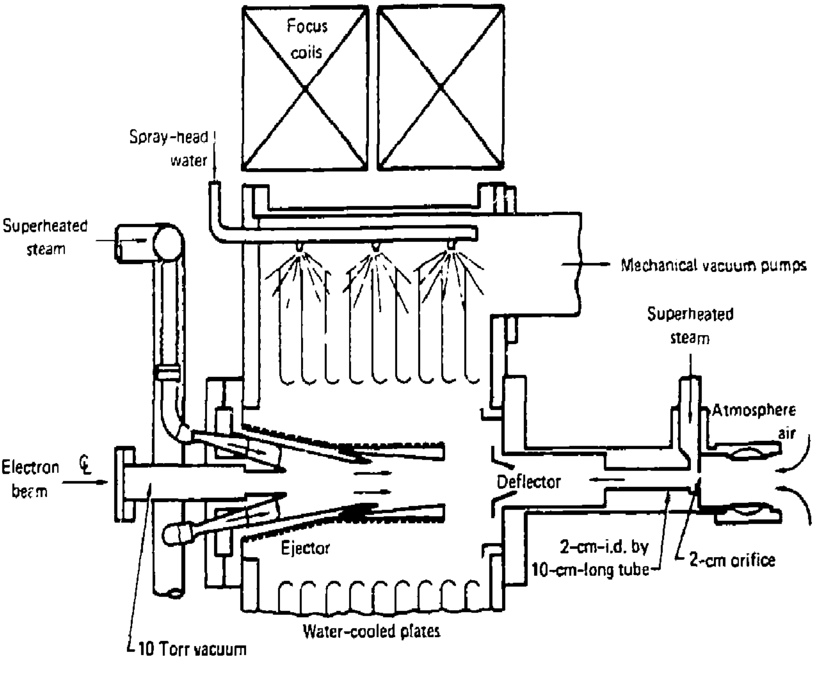

FIG. 10. The steam ejector-condenser prototype unit.

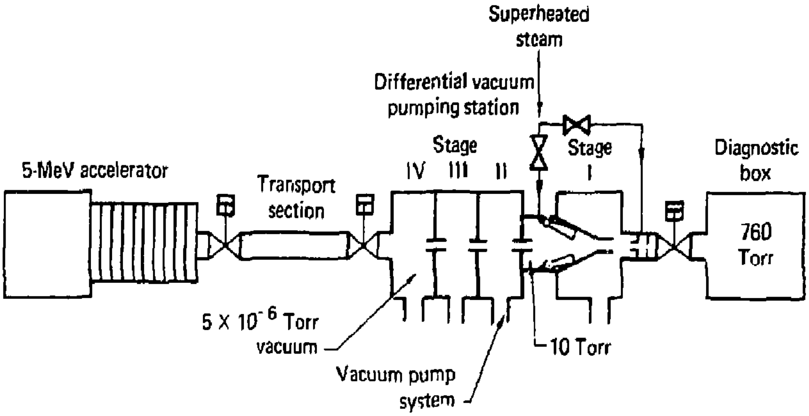

FIG. 11. The differential vacuum pumping station connected to a 5-MeV accelerator.

Because the vapor pressure of water is approximately 25 Torr at normal cooling temperatures, a vacuum is produced when the steam is condensed and the air is removed by a mechanical vacuum pump. To cool the air and condense the superheated steam, the condenser is outfitted with 6.5 m^2 (70 ft^2) of water-cooled surfaces and a direct-cooling spray system. The condensed water drains into a vacuum-tight collection vessel, which also provides a suction head for a circulating water pump. A canned-type centrifugal pump supplies condensate water to the direct-cooling spray system mounted in the upper portion of the condenser and discharges the excess to a drain at atmospheric pressure. A water-cooled trap removes water droplets from the air being pumped out of the condenser. Superheated steam is used to reduce the quantity of atmospheric air flowing into the steam ejector-condenser unit. The quantity of air that would flow through an unrestricted, 2-cm-diam orifice from atmospheric pressure to vacuum is 6.2×10^{-2} m^3/s at standard temperature and pressure (130 scfm). This presents a sizable vacuum pumping requirement, because a condenser pressure of 70 Torr or less is necessary to keep the steam ejector operating reliably. Superheated steam injected at the 2-cm orifice on the atmosphere side reduces the air flow to one-tenth of the unrestricted rate.

The steam ejector was fabricated from type 304 stainless steel. The vacuum flanges are a standard knife-edge design with copper gaskets and are suitable for high temperature use (500°C).

Conclusion

The prototype tests have shown that the steam ejector-condenser is a reliable operating unit suitable for long-term, steady-state accelerator operation. As the first stage of the differential vacuum pumping station, it will provide a pressure change from atmosphere to 10 Torr through an unrestricted 2-cm-diam aperture. The ejector also prevents air from entering the adjacent lower pressure stage, which permits high-volume cold trapping and cryopumping of water vapor in all of the remaining lower pressure stages.

The steam ejector-condenser system is relatively simple to start and operate. After closing the valve to the atmosphere, the utility systems, pump, boiler, and superheater are activated. When the inlet steam supply to the nozzles reaches 250°C at a pressure of 400 Torr, a vacuum in the ejector is established (10 Torr) and the atmospheric valve can be opened.

(For further information, contact C. L. Hanson, Ext. 2-7866, or T. W. Alger, Ext. 2-6194.)

References

1. K. Berkner, W. R. Baker, W. S. Cooper, K. W. Ehlers, W. B. Kunkel, R. V. Pyle, and T. W. Sterns, "Performance of LBL 20 kV, 10 A, and 50 A Neutral Beam Injectors," in *Proc. of the*

2nd Symp. on Ion Sources and Formation of Ion Beams (APS and USAEC, Berkeley, CA, October 1974).

2. K. W. Ehlers, "Rectangularly Shaped, Large-Area Plasma Source," *7th Symp. on Engr. Prob. of Fusion Res.* (ANS and IEEE, Knoxville, TN, October 1977).

MATERIALS FABRICATION DIVISION

The Materials Fabrication Division, a multidisciplinary organization within Mechanical Engineering, provides services that are not available from commercial sources. The number and diversity of LLNL research efforts make this Division one of the Laboratory's largest. We have about 400 highly skilled personnel and more than 3,700 pieces of equipment in our $13.5 million inventory. Our facilities provide special capabilities in the fields of optics, welding, vacuum process, glass, plastics, sheet metal, metal finishing, metrology, pressing, inspection, and assembly, as well as conventional and numerically controlled machining of metals, high explosives, and ceramics.

In-house fabrication services are available for all LLNL programs when requirements call for:

- Fabrication capabilities not readily available elsewhere.
- Rapid turnaround times.
- Handling of materials that are toxic, radioactive, or classified.

In addition, the Division's facilities are used to develop improved manufacturing techniques and to advance machine tool research. Our operating philosophy is to satisfy the mechanical fabrication need of the programs, consistent with priorities set by those programs.

(For further information, contact R. A. Berg, Ext. 2-7643.)

Laser Beams Offer Advantages in Brazing Applications

An advantage offered by brazing over fusion welding is that strong joints may be produced at relatively low heat input. Yet, most production brazing processes require heating the entire part to the brazing temperature.

This extended time at temperature can introduce undesirable interactions between the brazing filler metal and the base metal. Some parts have integral components of glass or plastic that would be destroyed at brazing temperatures. Also, joints frequently must be made near adhesively bonded connections, glass-to-metal seals and solid-state electronic circuits and components.

The application of electron-beam (EB) joining techniques has satisfied many requirements for a highly concentrated heat source capable of joining materials with minimal heat effects. Despite the narrow heat-affected regions and degree of control offered by EB methods, heat input and distortion are still excessive for some applications.

The development of metalworking lasers during the past decade has provided an even more precise tool for coping with the need for joining micro parts. But most laser joining so far has been confined to fusion welds. For certain types of joining requirements involving thin sections (often in thicknesses down to 0.001 in. (0.0254 mm), even laser fusion welding has not been entirely adequate.

Most of the problems encountered with laser and EB fusion welds in small parts have been associated with thermally damaging heat-sensitive materials near the joint and distorting thin-wall precision components. As part size and material thickness decrease, the difficulty of holding the parts in proper alignment and obtaining reproducible and uniform fusion along the entire joint length can increase to formidable proportions.

It became evident during laser welding attempts to satisfy some of these specialized requirements that if a yet lower-heat-input technique could be devised, many of these "impossible" precision joining and surfacing applications might be accommodated. It seemed likely that the energy characteristics of the laser beam, if properly controlled, might provide a degree of precision in localized brazing not attainable by other means. Therefore, we initiated a study to investigate the possibility of using laser beams as a micro-heat source to produce brazed joints.

It was not the intent [illegible] program to develop optimal joint properties in [illegible] material or combination of materials. [illegible] primary interest was simply to explore the feasibility [illegible] brazing thin sections with lasers, and to achieve this goal with minimal heat input. This was explored using the experimental test setup shown in Fig. 1. Once feasibility was demonstrated, further refinements of technique, joint geometry, [illegible] filler metal type, and other variables could be made as required for best overall response for given materials and applications.

The study led to these conclusions:

- Laser beams are a practical source of

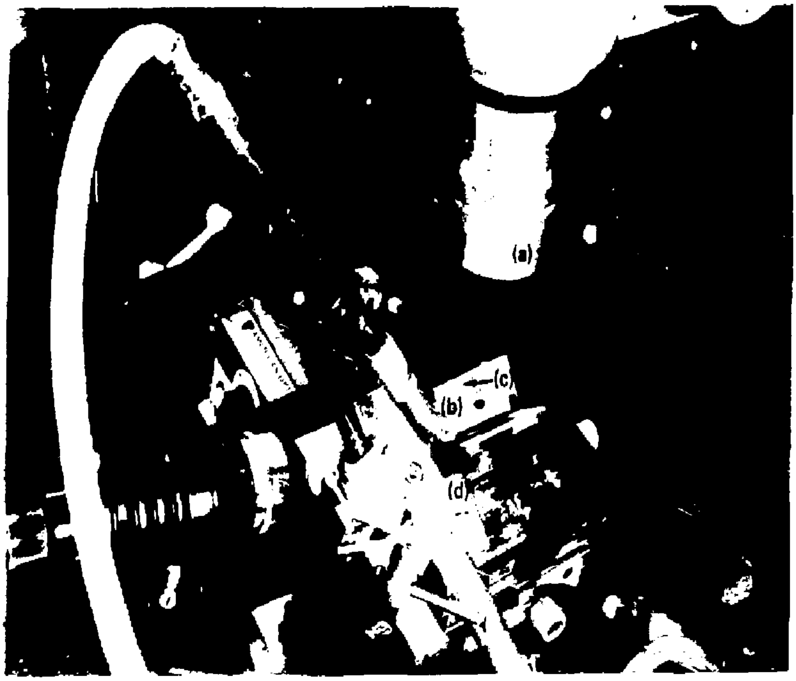

FIG. 1. Setup for laser brazing test. The laser beam from exit lens in cylindrical tube (a) at upper right passes downward through the hole in the inert-gas-shielding fixture (b) to the tee-joint test specimen (c) positioned on the vee-block (d) below it.

energy for brazing a wide range of metals and alloys using standard brazing filler metals.

- Best response in laser brazing materials having thicknesses less than about 0.01 in. (0.25 mm) is obtained with a low-replication-rate Nd:YAG pulsed laser using a defocused toroidal-shaped beam. Firing the laser beam directly over the brazing filler metal preplaced in the joint provides lowest heat input to the part with minimal distortion and interaction between base metal and brazing filler (Figs. 2 and 3).

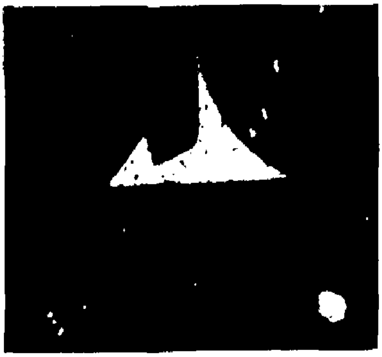

FIG. 2. A cross section of the joint (at 125X magnification) in 0.005-in.-thick type 304 stainless steel laser-brazed using a silver-copper alloy.

- The extremely rapid solidification and cooling rates (more than 10^6°C/s) characteristic of braze deposits produced in this manner result in an increase in deposit microhardness, with a nearly twofold increase for some compositions. This hardness increase in multiple-overlapping-spot deposits is believed due to the formation of supersaturated solid solutions or nonequilibrium crystalline phases.

- These effects offer opportunities for significantly increased mechanical joint properties for applications below the critical transformation temperatures of these metastable microstructures.

FIG. 3. Fillet (T-joint) between 5-mil type 316 stainless steel and 10-mil titanium laser-brazed with copper filler metal.

- While it is unlikely that laser brazing techniques will replace existing brazing procedures in applications adequately accommodated by conventional methods, the high energy densities offered by lasers, and their compatibility with computer numerical control systems, could make laser brazing a cost-effective competitor for production brazing applications involving large numbers of identical small parts.

(For further information, contact C. E. Witherell, Ext. 2-8341, or T. J. Ramos, Ext. 2-9938.)

Welding Stainless Steels for Structures that Must Withstand Liquid Helium Temperature

Superconducting magnets for fusion energy reactors require massive monolithic stainless steel weldments that must withstand extremely low temperatures under stresses approaching 100 ksi (700 MPa).

Such low temperatures come about because only superconducting magnets can achieve the required power density. Present magnet designs employ copper-stabilized columbium-titanium alloy superconductor windings at liquid helium temperature (4.2 K or -452°F). Operation of these magnets in the superconducting regime generates large reaction forces in the magnet's containment vessel, or structural support. To withstand these forces, wall thicknesses of several inches (>70 mm) are required.

These structures are complex curved shapes weighing several hundred tons. Critical closure seams, which often must be welded in a fixed position and under field conditions, present the fabricator with difficult quality assurance challenges, because welding must be from one side, without access for radiographic film placement or retrieval. These circumstances demand the highest attainable weld integrity.

A three-year study was conducted to determine the feasibility of producing heavy-section welds having usable levels of strength and toughness at 4.2 K (-452°F) for fabrication of these structures in type 304LN stainless steel plate.

Seven welding processes were evaluated. Test weldments in full-thickness plate were made under severe restraint to simulate that of actual structures (see Fig. 4). Type 316L filler metal was used for most welds.

The study yielded the following results:

- Fusion welds having yield strengths at liquid helium temperature matching that of nitrogen-modified Type 304L stainless steel plate, and acceptable levels of soundness, ductility, and toughness, have been made in heavy sections under full restraint using standard welding processes and commercially available Type 316L filler metal.
- Welds made under certain conditions and that solidify as primary austenite have exhibited intergranular embrittlement at cryogenic temperatures. This is believed to be associated with grain boundary metal carbides or carbonitrides that precipitate during the reheating of already-deposited beads by subsequent passes. Microfissuring in these welds may also be related to grain boundary carbide precipitates.
- Weld deposits that solidify as primary delta ferrite resist microfissuring and appear immune to intergranular embrittlement under ordinary welding conditions. However, ferrite residuals in the microstructure impair notch-toughness at low temperatures.
- Tests on Type 316L shielded metal arc welds indicate that, for fully austenitic deposits, the best cryogenic properties are obtained by:

(a) Using filler metals having the lowest attainable nitrogen and carbon contents (less than 0.020% for each is desirable).

(b) Using small diameter electrodes and filler wires, small weld beads, and good arc protection to avoid nitrogen pickup from the atmosphere

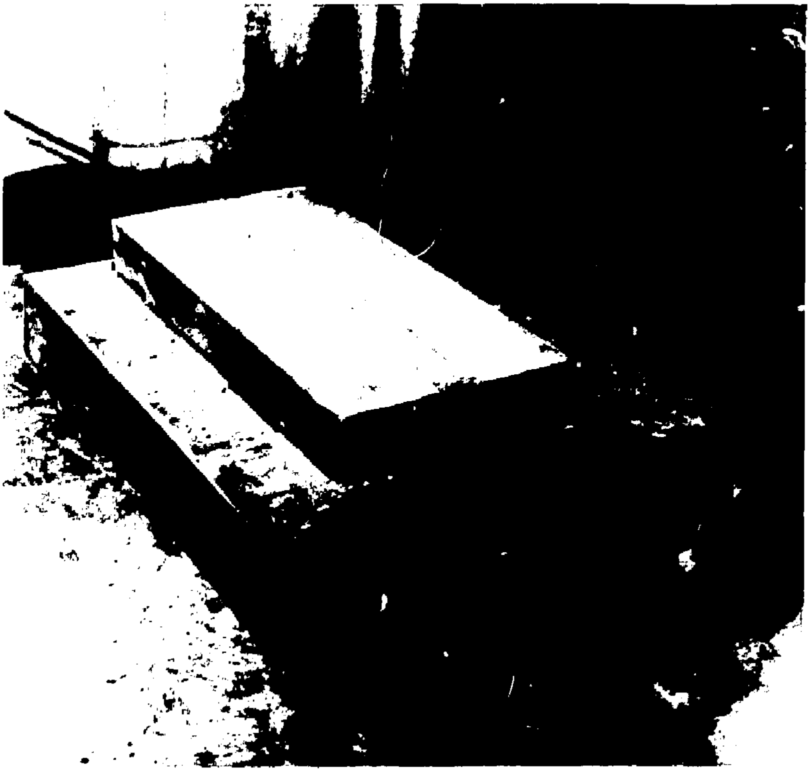

FIG. 4. **Test weldment in a 3-in.-thick plate of type 304LN stainless steel prepared while welded to a 4-in.-thick steel slab to simulate the heavy restraint of a superconducting magnet vessel.**

(c) Avoiding weaving or other deposition techniques leading to reheat cycles imposed upon previously deposited weld beads, which prolong time at temperatures *favorable to carbide* precipitation.

- For structural applications at liquid helium temperature, the choice between welds solidifying as primary austenite and those solidifying as primary delta ferrite must take into account several factors. The availability of fully austenitic fillers of favorable composition and the ability to ensure that they will be deposited under the proper conditions must be weighed against the decreased sensitivity to *microfissuring and grain boundary embrittlement* offered by welds that solidify as delta ferrite. However, careful control of the composition and use of filler metals solidifying as primary ferrite are required to minimiz[illegible]ion of ferrite residuals.

(For further information, contact C. E. Witherell, Ext. 2-8341.)

A Self-Calibrating Nondispersive Spectroradiometer Measures Absolute Concentrations of Atmospheric Gases in Field Environments

The need to measure carbon dioxide and liquefied natural gas (LNG) in field environments required new instrumentation to evaluate atmospheric stress on plant productivity, and to model the effects of weather on a large release of liquid fuel. Because no commercial instruments existed that could accurately measure to LLNL requirements, the Materials Fabrication Division worked with personnel of three programs to develop the needed instrumentation.

The combination of expertise and new technology has resulted in the production of 46 sensors of 6 different types, each one considered a prototype because of the development required for specific applications. These instruments are nondispersive spectroradiometers that use a self-calibrating reference wavelength and rationing electronics, which measure the specific gas concentration by its molecular absorption of infrared. Fast detectors and microprocessors normalize nonlinear effects. The output is absolute concentration, which can be recorded with respect to time.

Field instruments differ from those used in the laboratory. Their purpose is to obtain real-time measurements, either monitoring an environmental effect or measuring a dynamic change with the same accuracy obtainable in the laboratory. In the laboratory a gas is drawn into a controlled environment and the instrument response is peaked. The signal is averaged with time and recalibration is available at any time. The sample can be preserved for comparison or modified in a controlled way and remeasured. In the field a portable sensor is placed in the environment it is measuring.

The goal of the designers is an instrument free of calibration drift with good rejection of the interfering background signals in a harsh field environment. The "LNG" sensors stand open on towers in a 50°C desert sun and during a measurement cycle are subjected to a cryogenic gas and wind-blown ice crystal fog and potential flame front. The measurement volume is open so shipping and storage in agricultural environments are design considerations. The "aircraft" sensor required the design of a supporting pylon to expose the measuring volume to undisturbed air beyond the bow wave. This is highly unusual to expose optical instruments to this vibration, humidity, and temperature change during a precision measurement cycle.

Design

A single detector, single source with open optical cell and narrow infrared bandpass filters for wavelength selection provides the best arrangement. This scheme ratios an unattenuated wavelength through the same path with a wavelength attenuated by the concentration of a specific gas. This is done by only changing the bandpass infrared filters. For some applications a chopper is added for fast response or electronic signal integration. A major breakthrough was miniaturizing a folded-path optical absorption cell. This high throughput imaging cell allows eddy size correlation in open atmospheres and nonthermostated portability for chambered instruments like the one used to determine single-leaf parameters.

The variables and aberrations of these multipass cells were calculated and verified by test. For example, one 50-cm path is fully corrected at f/3 in a 3-cm cell. Half the correcton is a cylindrical germanium lens at the entrance pupil; another at the exit pupil images the tangential focus onto the sagittal image.

The design parameter relationships are

$$\Delta S \cong \frac{-D^2}{2R} \times \frac{N}{3} ,$$

where ΔS is the distance between the tangential and sagittal focus, D is the source-to-detector distance, R is the radius of the mirrors or cell length as they image at each other's radius, and N is the number of images on the field mirror and also the spacing between the objective mirror center lines.

This optical arrangement allows major elements to be set back behind the field mirror so that the source can be placed deep in its insulation and the chopper/filter between the mirror and detector at minimum blur. Variations in this electro-optical arrangement were made to accommodate the specifics of each measurement application. For example, the tower sensor shown in Fig. 5 does not require correction because the distance between the source and detector is small compared to the cell height.

For the aircraft and tower sensors we reversed the role of these mirrors to image the pupil onto the detector to minimize the effects of dirt on the mirrors and vibration in wind.

The LNG sensors[1] (Fig. 6) are subject to dense fog and water vapor condensation, so folding mirrors could not be used and paths were kept short.

Critical to all the designs are well-insulated black-body sources (durable optical coatings), stable pyroelectric detectors, and choppers that produce a minimum of noise. The development and search for improved components is in process. However, commercial recognition of the market is needed. Many instruments are required for measurement collaboration to form conclusions about our environment. Technology transfer is an important role in this program.

The Environmental Sciences Research Program includes an atmospheric stress and plant

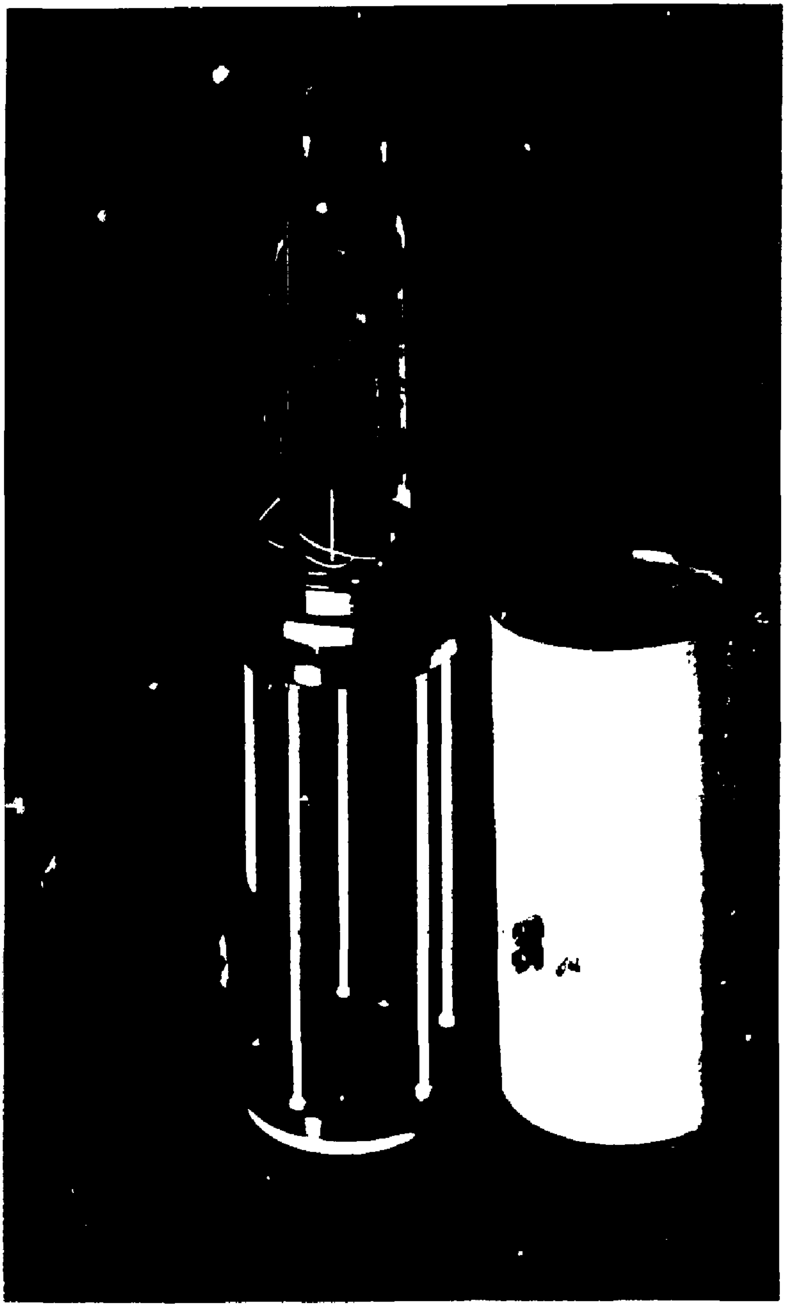

FIG. 5. The carbon dioxide tower instrument for ±0.2 ppm atmospheric concentration.

FIG. 6. Three prototype LNG sensors for greater percentage concentration changes at 0 to 100%.

productivity measurement capability[2,3] and the ambitious EPA program, National Crop Loss Assessment Network with CO_2 sensors. A consortium of federal agencies and universities are responding to the "World CO_2 problem" with two different LLNL instruments. One will be mounted on a tower over growing vegetation to monitor the carbon dioxide exchange for several days, and one will be placed on an aircraft to measure carbon uptake and release over large areas. As data loggers and collaborative measurements are developed, these sensors will be placed over jungle growth, in deserts, and on ice floes and ocean buoys to monitor long-term changes in our environment.

(For further information, contact C. H. Gillespie, Ext. 2-7584.)

Electroforming Copper Targets for a Fusion Materials Test Facility

Copper targets used in RTNS-II, the world's most intense 14-MeV neutron source, contain water-cooling channels for temperature control. There are two methods for fabricating these targets: (1) diffusion bonding a copper panel containing photoetched channels to another copper panel and (2) an electroforming technique that involves filling the photoetched channels with wax, electroplating thick copper to seal over the channels, and then removing the wax. The latter technique, a development of the Coating Processes Group, offers considerable promise over the diffusion bonding method, since it is less expensive and subject to fewer potential technical problems.

In the last decade the wax electroforming technique has been developed in industry to the point where it is now one of the primary methods of fabricating the channel closeout of regeneratively cooled thrust chambers. The most prominent application at present is the Space Shuttle Main Engine (SSME). For this application, electrodeposited nickel is used as the coolant channel closeout material for the wrought copper alloy (Narloy-Z) combustion chamber liners of the SSME.

Our work for RTNS-II utilizes the technology developed for the SSME. Targets 23 cm in diameter (for RTNS-I) and 50 cm in diameter (for RTNS-II) have been fabricated. Figure 7 shows the photoetched pattern used in the 50-cm targets. The convolutions in the channels enhance heat transfer to the coolant. The channels are 0.020-in. deep and vary from 0.020-to-0.080-in. wide. The electroforming procedure consists of filling the channels with wax, wet sanding to remove the excess wax and expose copper land areas, making the wax conductive by using silver powder, preparing the parts for plating by using a process consisting of anodic treatment in phosphoric acid followed by cathodic treatment in sulfuric acid, and then plating with thick copper (20 mils). The wax is then removed by flushing hot perchlorethylene through the channels with a specially designed fixture mounted in the center region of each panel. Neutron radiography has been used to verify wax removal from the channels. Parts are then routinely checked by pressure testing with water at 2500 psi. One part was pressure tested at 3600 psi and the holding fixture failed, further showing the integrity of the plated bond.

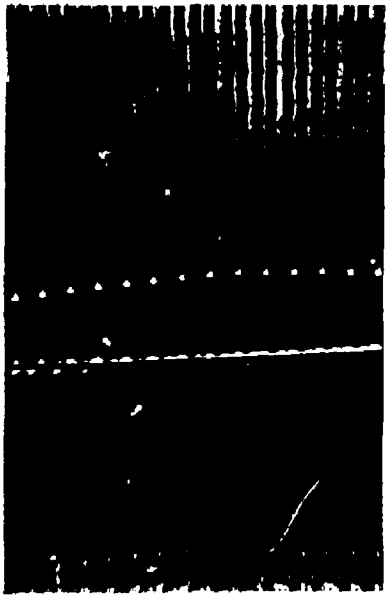

Fig. 7. A section of the etching mask used to produce water-cooling channels in a 50-cm-diam copper target for RTNS-II.

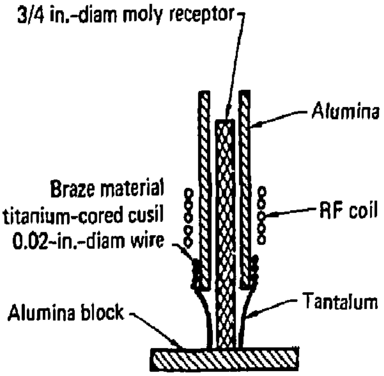

FIG. 8. Braze setup for a tantalum-alumina braze.

Work is presently being done to further fine-tune the electroforming process in the eventuality that this method is chosen as the base-line fabrication technique for targets.

(For further information, contact W. K. Keller, Ext. 2-7927 or J. W. Dini, Ext. 2-8342.)

Joining Tantalum to Ceramic by Brazing

A technique has been developed in the Vacuum Processes Laboratory for joining ceramic to tantalum by vacuum brazing. The joint is used to provide a vacuum leak-tight seal between the ends of a 1.3-in.-diam ceramic tube and tantalum electrodes. The completed assemblies provide a basis for a new generation of lasers for laser isotope separation.

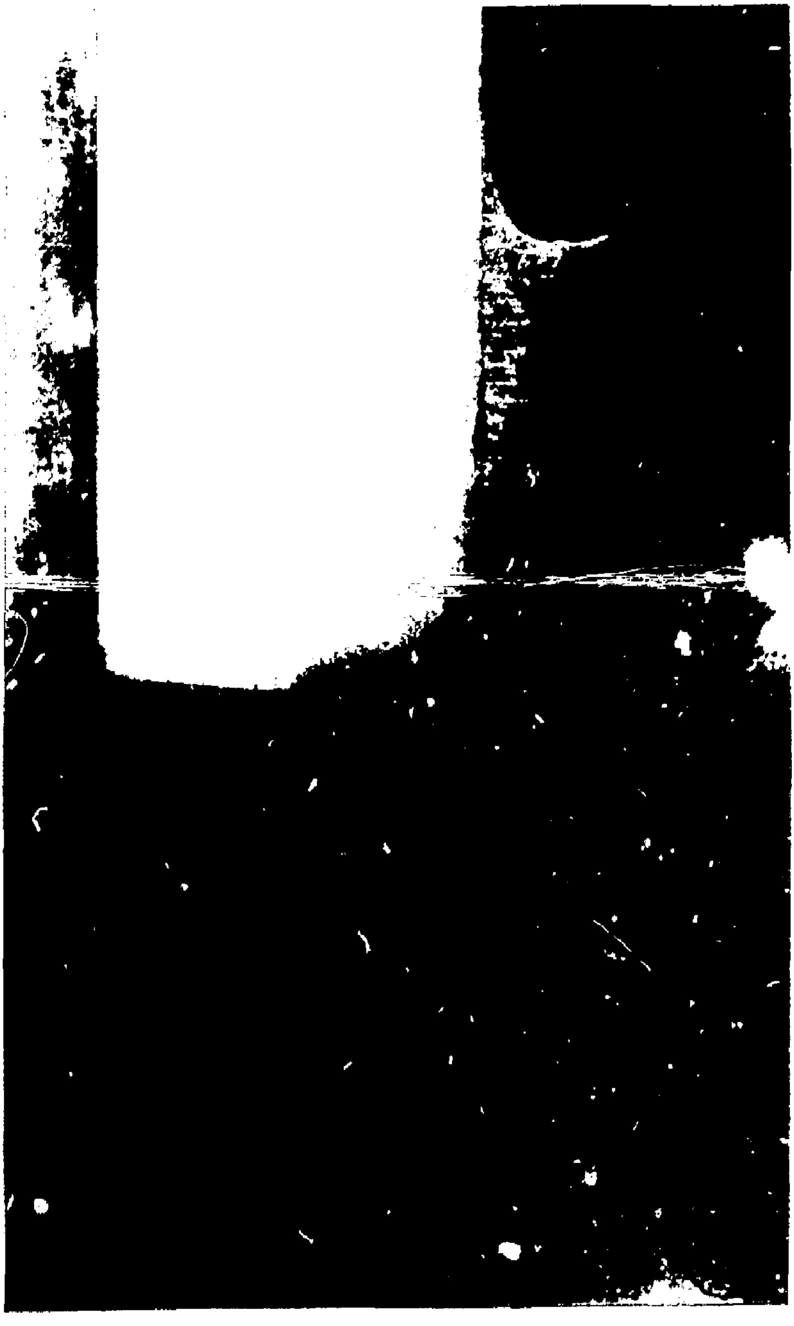

Fig. 9. Cross-section of a tantalum-alumina joint. Note the braze alloy fillet both above and below the point of contact.

Conventional techniques for joining metals to ceramic require premetalizing the ceramic with an active metal, such as titanium, a process both time-consuming and operator-dependent. The joining technique developed in the Vacuum Processes Laboratory uses a copper-silver eutectic with a central core of titanium for the braze alloy.

The braze, which is performed in a diffusion pumped vacuum system, is set up as shown in Fig. 8. Heating is done with a 10-kW, 450-kHz radio frequency power supply, coupled to the part by means of a 1/8-in. water-cooled copper coil. At 780°C, the copper-silver eutectic melts, exposing the titanium, which then chemically reacts with the alumina forming a boundary layer of TiO and TiO_2. The copper-silver then physically bonds to the titanium, forming the joint. Capillary action pulls the braze alloy through the joint, forming a fillet on both sides to add to the strength of the joint (see Fig. 9).

Tests have shown the joints to be vacuum leak tight, repairable, and consistently reproducible. Eliminating the premetalization process makes this single-step procedure better suited for production than the more conventional methods.

(For further information, contact D. D. Berger, Ext. 2-7684.)

References

1. G. E. Bingham, C. H. Gillespie, and J. H. McQuaid, *A Battery-Powered, Differential Infrared Absorption Sensor for Methane, Ethane, and Other Hydrocarbons*, Lawrence Livermore National Laboratory, Livermore, CA, Rept. UCRL-83317 (1979).
2. G. E. Bingham, "Predicting Plant Damage from Air Pollution," in *Energy and Technology Review*, September 1980, Lawrence Livermore National Laboratory, Livermore, CA.
3. P. I. Coyne and G. E. Bingham, "Photosynthesis and Stomal Light Responses in Snap Beans Exposed," in *APCA J.* **28**(11) (1978).

PUBLICATION ABSTRACTS*

H. P. Alesso, *An Isomorphism Between Reliability and Fault-Tree Structure Groups*, Lawrence Livermore National Laboratory, UCRL-85100 (1980). Prepared for the *SIAM Journal on Applied Mathematics*.

We present an isomorphism between reliability and fault-tree structure groups that will be useful for developing a noncoherent structure theory. Structure groups are construrted from coherent structure functions over the set {identity, dual, complement, *dual-complement*} of operations together with the binary composition mapping {°}.

Terry W. Alger, *Thermal Characteristics of Discharge-Heated Copper Vapor Laser (DHCVL) Heat Shields Formed of Multiple Coaxial Cylinders*, Lawrence Livermore National Laboratory, UCRL-83649 (1980). Prepared for the 19th Natl. Heat Transfer Conf., Orlando, FL, July 27–30, 1980.

A calculational method for predicting the axial temperature variation of each cylinder of a finite length heat shield formed of multiple coaxial cylinders was developed for longitudinal discharge, discharge-heated copper vapor laser (DHCVL) application. This model includes diffuse-gray thermal radiation and axial conduction effects, but it neglects radial conduction and convection. Example calculations for three different possible DHCVL geometries (diameters) are presented to demonstrate the importance of emissivity, number of included cylinders and the applied heat flux on the plasma tube maximum temperature and the axial temperature profile. Comparison is made between a predicted and a measured DHCVL maximum plasma tube temperature.

C. M. Bacigalupi, *Design of a Maze Structure to Attenuate Blast Waves*, Lawrence Livermore National Laboratory, UCRL-52921 (1980).

Building criteria for cells used to process and store high explosives dictated maze-type entries, to avoid mechanical closure devices. Experiments were conducted to develop a minimum-cost maze configuration that would limit the effects of an accidental 10-kg detonation to acceptable levels (<15 psig reflected) in adjacent areas. Components of suppressive design that were considered were right-angle turns, blast deflectors, baffles (reduced-area openings), and energy-absorbing materials The proposed configuration uses multiple baffles and a blast deflector to reduce the exit pressure to about 8 psig reflected.

Richard H. Bossi, *Luminous Intensity in Real-Time Radiography*, Lawrence Livermore National Laboratory, UCRL-84493 (1980).

Real-time radiographic systems relying on the conversion of x-rays to light in a fluorescent layer for imaging often employ a commercially available intensifying screen. The selection of the fluorescent screen for a given application is a function of the available radiation intensity and image quality considerations. A number of commercial fluorescent screens have been compared for light yield over a range of x-ray energies. The image quality of the screens has also been evaluated using edge spread and modulation transfer function measures.

Donald M. Boyd, *Holographic and Acoustic Emission Evaluation of Pressure Vessels*, Lawrence Livermore National Laboratory, UCRL-84046 (1980). Prepared for the Proc. of the ASME Centennial PVP Conf., San Francisco, CA, August 12-15, 1980.

---

*The abstracts are arranged alphabetically by first author's name.

Optical holographic interferometry and acoustic emission monitoring were simultaneously used to evaluate two small, high pressure vessels during pressurization. The techniques provide pressure vessel designers with both quantitative information such as displacement/strain measurements and qualitative information such as flaw detection. The data from the holographic interferograms were analyzed for strain profiles. The acoustic emission signals were monitored for crack growth and vessel quality.

Donald M. Boyd and William W. Wilcox, *Weld Evaluation on Spherical Pressure Vessels Using Holographic Interferometry*, Lawrence Livermore National Laboratory, UCRL-84079 (1980). Prepared for the 4th Intern. Congress on Experimental Mechanics, Society of Experimental Mechanics, Boston, MA, May 26–30, 1980.

Waist welds on spherical experimental pressure vessels have been evaluated under pressure using holographic interferometry. A coincident viewing and illumination optical configuration coupled with a parabolic mirror was used so that the entire weld region could be examined with a single hologram. Positioning the pressure vessel at the focal point of the parabolic mirror provides a relatively undistorted 360 degree view of the waist weld. Double exposure and real time holography were used to obtain displacement information on the weld region. Results are compared with radiographic and ultrasonic inspections.

Donald M. Boyd, William Wilcox, and Bruce Maxfield, *Holographic Interferometry Applied to Braze Evaluations*, Lawrence Livermore National Laboratory, UCRL-84279 (1980).

Double exposure holographic interferometry was used to determine the extent of the heat-affected zone of an electron-beam heated braze joint between two dissimilar metals.

C. A. Calder, E. C. Draney, and W. W. Wilcox, *Noncontact Measurement of the Elastic Constants of Plutonium at Elevated Temperatures*, Lawrence Livermore National Laboratory, UCRL-84139 (1980). Prepared for the *Journal of Nuclear Materials.*

The elastic constants at elevated temperature were measured for pure α-phase Pu and Pu-1 wt% Ga delta-stabilized alloy. Test temperatures ranged from ambient to 119°C for the α-phase Pu and to about 500°C for the delta-stabilized Pu alloy. A recently developed noncontact testing technique was used that incorporated high energy laser deposition with Michelson displacement interferometry. Young's modulus and the shear modulus decreased linearly as the temperature increased. The testing was limited by mirror degradation at phase change temperatures.

Gary W. Carter, *A Unique Rod Lens/Video System Designed to Observe Flow Conditions in Emergency Core Coolant Loops of Pressurized Water Reactors*, Lawrence Livermore National Laboratory, UCRL-52902 (1979).

This report describes techniques and equipment used for video recordings of the single- and two-phase fluid flow tests conducted with the PKL Spool Piece Measurement System designed by Lawrence Livermore Laboratory and E.G.&G., Inc. The instrumented spool piece provides valuable information on what would happen in pressurized water reactor emergency coolant loops should an accident or rupture result in loss of fluid. Field testing of the 80.8-mm and 113.0-mm internal diameter spool pieces was conducted at the Wyle Laboratories Experimental Test Facility in Norco, CA. The video recordings of the various flow parameters were made between February and April 1979. The complete closed-circuit television video system, including rod lens, light supply, and associated spool mounting fixtures, is discussed in detail. Photographic examples of test flows taken during actual spool piece system operation are shown.

Alan B. Casamajor, *The Impact of Land Use on Solar Industrial Process Heat for the Food Processing Industry,* Lawrence Livermore National Laboratory, *UCRL-85019 (1980). Prepared for the* Solar Industrial Process Heat Conf., Houston, TX, December 17-19, 1980.

A solar land use study of 1330 food processing plants located in the far-western United States (Arizona, California, Hawaii, Oregon, and Washington) has been conducted. Based upon estimates of each plant's annual energy consumption of process heat, derived from: annual sales figures, employment, and total energy consumption for that plant's Standard Industrial Classification (SIC) group; and the available surface area at each plant, determined by a site inspection, an assessment of each plant's potential for solar energy was made. Those industries having the highest potential for applying solar energy to their process heat loads include:

- Fruit and vegetable packing
- Sugar refining
- Meat packing
- Wine and brandy
- Bread
- Daily products

It has been further determined that about 25% of the energy used for food processing in the study area can be supplied by solar if all of the available surface area at and adjacent to these plants is devoted to solar collectors.

Ray H. Cornell, Stephen D. Santor, and Ronald D. Streit, *Evaluation of Heat Generation in SBR due to Cyclic Loading with Application to the T-142 Tank Shoe Pad,* Lawrence Livermore National Laboratory, UCRL-84633 (1980). Prepared for the ACS Rubber Division Meeting (Paper No. 40), Detroit, MI, October 7-10, 1980.

Field tests of a temperature measuring method for calculating hysteretic heat in generation in T-142 tank pads correlates well with values calculated from a formula derived by Battelle. The temperature method calculates a heat generator rate of 108 kW/m^3 while the Battelle formula gives 107 kW/m^3. Hysteresis determinations from small laboratory samples did not show direct correlation between temperature derived heating rates. While the mechanical data shows total heat generation temperature measurements only relates local hysteresis. Our temperatures were taken centrally in the laboratory sample where heat generation may be small compared to heat generated near the periphery. More work in this area is planned.

J. K. Crane, R. D. Smith, W. L. Johnson, C. W. Johnson, C. W. Jordan, S. A. Letts, G. R. Korbel, and R. M. Krenick, *The Use of Molecular Beams to Support Microspheres During Plasma Coating,* Lawrence Livermore National Laboratory, *UCRL-*84488 (1980). Prepared for the 27th Natl. American Vacuum Soc. Symp., Detroit, MI, October 14-17, 1980.

Spherical laser fusion targets can be levitated on beams of Ar or other gas atoms. This is an especially useful and reliable technique for supporting microspheres during plasma coating or plasma etching. The reliability of this technique is principally the result of two things: the success of a special centering device which provides a lateral, stabilizing force on the levitated microspheres; and a gas handling system which is capable of controlling levitation gas flow in the microtorr liter/sec range. We have determined that the operational regime of this device is that of Knudsen's flow. This knowledge of the flow characteristics has been important in developing this device.

D. Douglas Davis, Clyde W. Dease, Ronald I. Wallace, and Carl E. Walter, *The Roadway Powered Electric Vehicle (RPEV) System,* Lawrence Livermore National Laboratory, UCRL-83662 (1980). Prepared for The Electric Vehicle Exposition & Conf., St. Louis, MO, May 20-22, 1980.

Practicality of the Roadway Powered Electric Vehicle (RPEV) System under dynamic operating conditions is being examined by the Lawrence Livermore National Laboratory (LLNL). In the RPEV System, energy is electromagnetically coupled without mechanical contact from a powered roadway to electric vehicles. Energy from the roadway can be used for high-speed, long-range travel, and for replenishing energy stored onboard the vehicles. The stored energy is available for shorter range travel on nonpowered surface streets.

The dynamic test system at LLNL includes a 50-m lane of powered roadway, an ac power source and an electrically propelled test vehicle equipped with a roadway power pickup, onboard batteries, and instrumentation. The dynamic power coupling system allows up to 16 kW of coupled power. Its design is based on results obtained from static prototype tests, conducted previously at the Lawrence Berkeley Laboratory (LBL). Dynamic tests will examine power coupling capacity, system characteristics, vehicle performance, roadway compatibility, and safety.

The report includes descriptions of the LLNL dynamic test facility, the status of RPEV component and test system development, dynamic test plans, and results of the static prototype tests previously conducted by LBL.

J. N. Doggett, C. C. Damm, and C. L. Hanson, *The Tandem Mirror Next Step—Remote Maintenance,* Lawrence Livermore National Laboratory, UCRL-84624 (1980). Prepared for the ANS Winter Meeting, Washington, D.C., November 17-21, 1980.

Our study of the next proposed experiment in the Mirror Fusion Program, the Tandem Mirror Next Step (TMNS), has included serious consideration of the maintenance requirements of such a large source of high energy neutrons with its attendant throughput of tritium. Although maintenance will be costly in time and money, our conclusion is that with careful attention to a "design for maintenance" plan such a device can be reliably operated.

David B. Duncan and Warren H. Giedt, *Measured and Predicted Temperatures and Strains in Stationary GTA Welds,* Lawrence Livermore National Laboratory, UCRL-84552 (1980). Prepared for the Intern. Conf. on Welding Research in the 1980's, Welding Research Institute, Osaka University, Japan, October 27–29, 1980.

Local temperature measurements on the heated and unheated surfaces and strain measurements on the unheated surfaces of unrestrained circular weld specimens of pure nickel and nitronic 40 stainless steel during stationary welding are compared with values predicted from finite element programs for temperature and strain variations. Experimental and predicted temperature histories agree within 5% for nickel and 10% for the stainless steel. The larger differences for the steel may be due to less precise property data. Radial and hoop strain and unheated surface displacement variations presented for the stainless steel show agreement to within about 25% of the finite element code results. Further study of the influence of property variation and different welding conditions is suggested.

John O. Hallquist, *User's Manual for DYNA2D—An Explicit Two-Dimensional Hydrodynamic Finite Element Code with Interactive Rezoning,* Lawrence Livermore National Laboratory, UCID-18756 (1980).

This report provides a user's manual for DYNA2D, an explicit two-dimensional axisymmetric and plane strain finite element code for analyzing the large deformation dynamic and hydrodynamic response of inelastic solids. A contact-impact algorithm permits gaps and sliding along material interfaces. By a specialization of this algorithm, such interfaces can be rigidly tied to admit variable zoning without the need of transition regions. Spatial discretization is achieved by the use of 4-node solid elements, and the equations-of-motion are integrated by the central difference method. An interactive rezoner eliminates the need to terminate the calculation when the mesh becomes too distorted. Rather, the mesh can be rezoned and the calculation continued. The command structure for the rezoner is described and illustrated by an example.

Jack Hovingh, *Heat Transfer in Inertial Confinement Fusion Reactor Systems,* Lawrence Livermore National Laboratory, UCRL-81673 (1980). Prepared for the 19th Natl. Heat Transfer Conf., Orlando, FL, July 27-30, 1980.

The short time and deposition distance for the energy from inertial fusion products results in local peak power densities on the order of 10^{18} watts/m^3. This paper presents an overview of the various inertial fusion reactor designs which attempt to reduce these peak power intensities and describes the heat transfer considerations for each design.

Jack Hovingh and James A. Blink, *Parametric Analysis of Stress in the ICF HYLIFE Converter Structure,* Lawrence Livermore National Laboratory, UCRL-84272 (1980). Prepared for Proc. 4th Topical Meeting on Techn. of Controlled Nuclear Fusion, King of Prussia, PA, October 14-17, 1980.

The concept of a liquid-metal first wall in an ICF energy converter has a particularly attractive feature: the liquid metal absorbs the short-ranged fusion energy and moderates and attenuates the neutron energy so that the converter structure may have a lifetime similar to that of a conventional power plant. However, the sudden deposition of fusion energy in the liquid-metal first wall will result in disassembly of the liquid, which then impacts on the structure. The impact pressure on the structure is a strong function of the location and thickness of the liquid-metal first wall. The impact stress is determined by the impact pressure and duration and by the thickness and location of the structure. The maximum allowable stress is determined by the design stress criteria chosen by the structural designer. Scaling laws for the impact pressure as a function of the liquid-metal first wall location and mass are presented for a 2700 MW(f) (fusion power) plant with either one or four fusion reactor vessels. A methodology for determining the optimum combination of liquid-metal first wall geometry and first-structural-wall thickness is shown. Based on the methodology developed, a parametric analysis is presented of the liquid-metal flow rate and first-structural-wall requirements.

R. W. Howard, R. M. Scanlan, G. S. Smith, and C. L. Farrell, *The Effect of Strain on the Martensitic Phase Transition in Superconducting Nb_3Sn,* Lawrence Livermore National Laboratory, UCRL-84211 (1980). Prepared for Proc. 1980 Superconductivity Conf., Santa Fe, NM, September 19–October 2, 1980.

The connection between the cubic-to-tetragonal martensitic phase transformation and the phenomenon of superconductivity in A15 compounds is being investigated. The degradation of the critical parameters, such as T_c, H_{c2}, and J_c, with mechanical straining is of particular interest. Since martensitic transitions are also known to be strain sensitive, perhaps the structural change is directly responsible for the reduction in superconducting properties. We performed low-temperature x-ray diffraction experiments on Nb_3Sn ribbons (with the bronze layers etched off) mounted on copper and indium sample stages. The cryostat we used is unique in that it has a vacuum mechanical insert which allows the superconductor to be placed under both compressive and tensile strains while at low temperatures. Preliminary results indicate that the martensitic phase transition temperature, T_m, increases with compressive strains. Other effects of strain on tetragonal phase production are also discussed.

C. A. Hurley, *Some Comments on the Shiva Spaceframe Earthquake Damage,* Lawrence Livermore National Laboratory, UCID-18644 (1980).

On January 24, 1980, at 11:00 a.m., an earthquake, measuring 5.5 on the Richter scale, shook the Livermore Valley. There were three very pronounced shocks, the first at 5.5 followed by two, one at 5.2 and the other at 4.8, on the Richter scale. The Shiva spaceframe was shaken out of alignment. Shiva consists of two frames, a laser frame and a target frame. Components on each frame stayed within alignment with respect to each other, but the target frame moved with respect to the laser frame. Shearing of the seismic anchor bolts on the target frame was responsible for this misalignment. The operations staff was kept out of the laser bays until the unanchored frame was made safe. The reason for the seismic anchor failing lies in the unique design of the frame as an optical bench, not as a building or as a normal load bearing structure. This was the third in a series of earthquakes for Shiva, the first occurring on June 20, 1977 at a magnitude of 4.7 on the Richter scale and an epicenter 2 miles away. The second quake was on August 6, 1979, with a magnitude of 5.9 and the epicenter 60 miles away. There was no damage or misalignment due to these first two earthquakes. The third however, severely tested the Shiva system and will be the subject of this report. Accelerometers were not in operation on the system so we do not know what the acceleration forces were. Our subsequent investigation however, gives us some indication of these forces.

C. A. Hurley, *Mechanical Technology Unique to Laser Fusion Experimental Systems*, Lawrence Livermore National Laboratory, UCRL-84052 (1980). Prepared for the 11th Symp. on Fusion Techn., Oxford, United Kingdom, September 15–19, 1980.

Hardware design for laser fusion experimental machines has led to a combination of engineering technologies that are critical to the successful operation of these machines. These large opto-mechanical systems are dependent on extreme *cleanliness*, accommodation to efficient *maintenance*, and high *stability*. These three technologies are the primary mechanical engineering criteria for laser fusion devices.

J. D. Illige, C. M. Yu, and S. A. Letts, *Metal Coatings for Laser Fusion Targets by Electroplating*. Lawrence Livermore National Laboratory, UCRL-84474 (1980). Prepared for the 27th Natl. American Vacuum Soc. Symp., Detroit, MI, October 14–17, 1980.

Metal coated laser fusion targets must be dense, uniform, spherically symmetric to within a few percent of their diameters and smooth to better than a few tenths of a micron. Electroplating offers some unique advantages including low temperature deposition, a wide choice of elements and substantial industrial plating technology. We have evaluated electroless and electroplating systems for gold and copper, identified the factors responsible for small gain size and plated glass microspheres with both metals to achieve smooth surfaces and highly symmetric coatings. We have developed plating alloys which sustain the microspheres in continuous random motion during plating. We have established techniques for deposition of the initial conductive adherent layer on the glass microsphere surface. Coatings as thick as 15 microns have been made. The equipment is simple, relatively inexpensive and may be adopted for high volume production of laser fusion targets.

R. R. Jacobs, D. Eimerl, J. Goldhar, J. R. Murray, W. R. Rapoport, L. Schlitt, and J. C. Swingle, *Intensification of Rare Gas Halid Lasers with Application to Laser Fusion*, Lawrence Livermore National Laboratory, UCRL-84082 (1980). Prepared for Optical Engineering Proc. of 1980 European Conf. on Optical Systems and Applications, Utrecht, The Netherlands, September 23–25, 1980.

The two techniques of backward-wave Raman pulse compression and pulse stacking are reviewed in the context of using KrF lasers as drivers in inertial confinement fusion. Experimental and theoretical results on Raman pulse compression in methane are presented including data on 70–75% pump energy extraction by the counterpropagating Stokes wave. Results from on-going pulse stacker/Raman compressor experiments are also described, along with future investigations in this general area.

Ralph R. Jacobs, Julius Goldhar, David Eimerl, Steven B. Brown, and John R. Murray, *High Efficiency Energy Extraction in Backward Wave Raman Scattering*, Lawrence Livermore National Laboratory, UCRL-84028 (1980). Prepared for *Applied Physics Letters*.

Pump depletions of 70–75% have been demonstrated for a KrF laser-driven, methane gas-filled backward Raman amplifier and are in agreement with predictions of the Frantz-Nodvik saturated amplifier model. The associated counterpropagating Stokes laser intensity is measured to be $\lesssim 3.5$ times that of the pump; the corresponding pulse compression ratio is ≈ 5.

Satish V. Kulkarni, *Flywheel Rotor and Containment Technology Development Program of the U.S. Department of Energy*, Lawrence Livermore National Laboratory, UCRL-84713 (1980). Prepared for the 3rd Intern. Conf. on Composite Materials, Paris, France, August 25–29, 1980.

The status of the flywheel rotor and containment technology development program in the United States, sponsored by the Department of Energy, is reviewed in this paper. The specific objectives of the effort are delineated, and prototype composite rotor designs are described. These prototypes are being evaluated to identify promising designs for future development and end-use applications. The composite-laminated-rotor development effort at Lawrence Livermore National Laboratory (LLNL) and General Electric are also discussed, including design modifications to improve energy density, fabrication of thick composite laminates and filament-wound rings, low-cost manufacturing processes, generation of rotor-design data, nondestructive inspection, and spin testing of rotors. Finally, an assessment is made of the current rotor-burst-containment design philosophy and of the applicability of jet-engine fan-blade containment technology to flywheel systems. Based on this assessment, preliminary design criteria for containment are evolved.

Stephen M. Lane, E. Michael Campbell, and Charles Bennett, *Measurement of DT Neutron-Induced Activity in Glass Microshell Laser-Fusion Targets,* Lawrence Livermore National Laboratory, UCRL-83882 (1980). Prepared for *Applied Physics Letters.*

Laser-fusion targets consisting of DT gas contained in Teflon-coated glass microshells produce 14.1-MeV neutrons that can interact with the ^{28}Si nuclei in the glass to produce radioactive ^{28}Al. Using a very efficient collection-detection scheme that could detect the decay of 10% of the ^{28}Al created, we identified these nuclei by their 1.78-MeV gamma ray that decayed with a 2.2-min half-life. From the number of ^{28}Al nuclei created and the neutron yield the compressed glass areal density was found to be 0.0059 g/cm^2.

D. R. Lesuer, J. B. Bergin, S. A. McInturff, and B. A. Kuhn, *Liquid-Metal Embrittlement of Refractory Metals by Molten Plutonium,* Lawrence Livermore National Laboratory, UCRL-83986 (1980). Prepared for the 13th Annual Technical Meeting of the Intern. Metallographic Soc., Brighton, England, August 18–20, 1980.

We have studied the embrittlement by molten plutonium of the refractory metals and alloys W-25 wt% Re, tantalum, molybdenum, and Ta-10 wt% W. At 900°C and a strain rate of 10^{-4} s^{-1}, the materials tested may be ranked in order of decreasing susceptibility to liquid-plutonium embrittlement as follows: molybdenum, W-25 wt% Re, Ta-10 wt% W, and tantalum. These materials exhibited a wide range in susceptibility. Embrittlement was found to exhibit a high degree of temperature and strain-rate dependence, and we present arguments that strongly support a stress-assisted, intergranular, liquid-metal corrosion mechanism. We also believe microstructure plays a key role in the extent of embrittlement. In the case of W-25 wt% Re, we have determined that a "dealloying" corrosion takes place in which rhenium is selectively withdrawn from the alloy.

S. A. Letts, D. W. Myers, and L. A. Witt, *Ultrasmooth Plasma Polymerized Coatings for Laser Fusion Targets,* Lawrence Livermore National Laboratory, UCRL-84475 (1980). Prepared for the 27th Natl. American Vacuum Soc. Symp., Detroit, MI, October 14–17, 1980.

Coatings for laser fusion targets were deposited up to 135 μm thick by plasma polymerization onto 140 μm diameter DT filled glass microspheres. Ultrasmooth surfaces (no defect higher than 0.1 μm) were achieved by eliminating particulate contamination. Process generated particles were eliminated by determining the optimum operating conditions of power (20 watts), gas flow (0.3 sccm trans-2-butene, 10.0 sccm hydrogen), and pressure (75 millitorr), and maintaining these conditions through feedback control. From a study of coating defects grown over known surface irregularities, a quantitative relationship between irregularity size, film thickness, and defect size was determined. This relationship was used to set standards for the maximum microshell surface irregularity tolerable in the production of hydrocarbon or fluorocarbon coated laser fusion targets.

Ernest H. Lorbeer and Carl E. Walter, *System for Acquisition and Reduction of Demonstration Data for Electric Vehicles,* Lawrence Livermore National Laboratory, UCID-18754 (1980).

Congress seeks to reduce petroleum consumption by encouraging the use of electric vehicles and has legislated an Electric and Hybrid Vehicle Demonstration project. In carrying out this mandate, DOE developed a data plan to assess the Demonstration project. The Data Acquisition and Reduction Module (DARM) System was developed by LLNL for use on demonstration electric vehicles to determine reliably and inexpensively quantitative data on their performance.

The DARM System consists of an instrumentation unit which is installed in selected demonstration vehicles, a tape reader, and data reduction programs. Once the on-board DARM unit is installed, the vehicle operator needs only to insert and remove cassette tapes at intervals of up to three months. The tapes can be reduced with the specialized reduction program, entered into a data base, and the data subjected to analysis at a Data Reduction Center.

DARM provides data on energy consumption (into and out of the battery), distance and time travelled, and number of stops experienced. A profile of energy consumption and time spent as a function of speed and acceleration allows deduction of driver satisfaction and provides direction to designers for improving electric vehicle performance.

John T. Merrill, *Evaluation of Aerosol-Control Measures on Flow Sorters,* Lawrence Livermore National Laboratory, UCRL-83530 (1980). Prepared for *Cytometry.*

Flow sorters produce microdroplets as part of their normal operation, and if these microdroplets escape into the room, they are potentially hazardous. We have tested several aerosol-control measures on a commercial flow sorter. To accomplish this, T-4 phage were introduced into the sorter's liquid jet through the sample injection tube, and culture plates containing lawns of T-4-sensitive *E. coli* bacteria were exposed around the sorter for each operational configuration. After the exposure, the plates were incubated and then scored for plaques. A single phage-containing microdroplet landing on a plate was sufficient to cause a plaque of lysed bacteria to form. The number of plaques was thus an indicator of how much aerosol was released for each configuration. The most effective control of aerosols was accomplished by catching the central undeflected stream in a vacuum-exhausted tube, and this technique, coupled with the manufacturer's vacuum-exhaustion of the air around the sorting location, produced no plaques. Allowing the undeflected stream to splash into a flask or beaker produced the most plaques, excluding failure modes of the instrument. Several failure modes were tested, including having the central stream hit the outside of the catch-tube or deflection plates, and loss of the manufacturer's vacuum-exhaustion system. Many flow sorters allow the undeflected stream to splash and are thus producing aerosols. The simple addition of a catch-tube removed this major contributor to the aerosol production.

D. Milam, J. B. Willis, F. Rainer, and G. R. Wirtenson, *Determination of Laser Damage Thresholds by Comparison with an Absolute Laser Damage Standard,* Lawrence Livermore National Laboratory, UCRL-84830 (1980). Prepared for *Applied Physics Letters.*

Absolute laser-damage thresholds can be rapidly measured by comparison with an absolute laser-damage standard.

R. C. Murray, T. A. Nelson, and D. S. Ng, *Seismic Review of the R.E. Ginna Nuclear Power Plant as Part of the Systematic Evaluation Program for the Nuclear Regulatory Commission,* Lawrence Livermore National Laboratory, UCRL-84155 (1980). Prepared for the American Society of Civil Engineers Specialty Conf., Civil Engineering and Nuclear Power, Knoxville, TN, September 15–17, 1980.

This paper is a progress report on work at the Lawrence Livermore National Laboratory (LLNL) to perform a limited seismic reassessment of the Robert E. Ginna Nuclear Power Plant. The reassessment is being done for the Nuclear Regulatory Commission (NRC) as part of the Systematic Evaluation Program. The reassessment focuses generally on the reactor coolant pressure boundary and on those systems and components necessary to shut down the reactor safely and to maintain it in a safe shutdown condition following a postulated earthquake characterized by a peak horizontal ground acceleration of 0.2 g. Methods and modeling procedures used to analyze a complex of interconnected buildings are highlighted. However, results, conclusions, and recommendations about the ability of the structures to withstand the postulated earthquake are not presented. Such judgments will be part of the final report on the LLNL reassessment of Ginna for the NRC.

R. C. Murray and H. J. Weaver, *Dynamic Behavior of LLNL Buildings During Aftershocks of the January 24, 1980 Greenville Earthquake,* Lawrence Livermore National Laboratory, UCRL-52969 (1980).

Computer programs developed at the Lawrence Livermore National Laboratory (LLNL) were used to extract information about the dynamic behavior of several LLNL structures from velocity time-history signals recorded during two earthquake aftershocks. The most complete analysis was performed on Building 111. This analysis is presented as a case study to show the power of the LLNL computer codes in identifying the principal vibratory modes of a structure and the frequencies and damping values of these modes. The importance of this technique for monitoring changes in the seismic integrity of critical structures is discussed.

Jon L. Opsal, *Matrix Theory of Elastic Wave Scattering: Application to Scattering of Transverse Waves,* Lawrence Livermore National Laboratory, UCRL-84116 (1980). Prepared for the ARPA/AF Review of Progress in Quantitative NDE, Scripps Institution of Oceanography, La Jolla, CA, July 8–13, 1979.

New calculations of elastic wave scattering using Visscher's matrix theory have been made for transverse waves incident on axially symmetric defects. Longitudinal incident waves have also been considered with the results in agreement with those obtained previously by Visscher. A number of interesting features for incident transverse waves will be presented as well as some of the practical aspects of the calculation (e.g. convergence, accuracy, and computer time).

R. G. Ozarski and J. Prior, *Polarizer Reflectivity Variations,* Lawrence Livermore National Laboratory, UCID-18588 (1980).

On Shiva the beam energy along the chain is monitored using available reflections and/or transmission through beam steering, splitting, and polarizing optics without the intrusion of any additional glass for diagnostics. On the preamp table the diagnostic signal is obtained from the signal transmitted through turning mirrors. At the input of each chain the signal is obtained from the transmission through one of the mirrors used for the chain input alignment sensor (CHIP). At the chain output the transmission through the final turning mirror is used. These diagnostics have proved stable and reliable. However, one of the prime diagnostic locations is at the output of the beta rod. The energy at this location is measured by collecting small reflections from the last polarizer surface of the beta Pockels cell polarizer package. Unfortunately, calibration of this diagnostic has varied randomly, seldom remaining stable for a week or more. The cause of this fluctuation has been investigated for the past year and it has been discovered that polarizer reflectivity varies with humidity. This report will deal with the possible causes that were investigated, the evidence that humidity is causing the variation, and the associated mechanism.

John H. Pitts, *A Consistent HYLIFE Wall Design That Withstands Transient Loading Conditions,* Lawrence Livermore National Laboratory, UCRL-84271 (1980). Prepared for Proc. 4th ANS Topical Meeting on Techn. of Controlled Nuclear Fusion, King of Prussia, PA, October 14–17, 1980.

Our design for a first structural wall (FSW) promises to satisfy the impact and thermal stress loads for the 30-year lifetime anticipated for the HYLIFE reaction chamber. The FSW is a 50-mm-thick cylindrical plate that is 10 m in diameter; it can withstand a rapidly varying liquid metal impact stress up to a peak of 60 MPa, combined with slowly varying thermal stresses up to 86 MPa. We selected 2-1/4 Cr-1 Mo ferritic steel as the structural material because it has adequate fatigue properties and yield strength at the peak operating temperature of 810 K, is compatible with liquid lithium, and has good neutron activation characteristics.

H. T. Powell and R. J. Poli, *Electron Beam-Pumping of XeCl Using Variable Current Density,* Lawrence Livermore National Laboratory, UCRL-84680 (1980). Prepared for the 33rd Gaseous Electronics Conf., Norman, OK, October 7–10, 1980.

We have studied the XeCl fluorescence and laser performance as a function of e-beam current density, gas mixture, and laser cavity reflectors. A well-defined gas volume was homogeneously excited by an e-beam current density in the range 5-500 A/cm^2 for a period of 50 ns. We have used either Cl_2, HCl, CCl_4, or CCl_3F as chlorine donors and have observed qualitative effects caused by vibrational excitation of the donor and subsequently increased electron attachment, burn-out of the chlorine donor, and electron deactivation of XeCl. We found only minor differences in both fluorescence and laser performance between Ne, Ar, and Kr as majority diluents. We also studied the saturation of XeCl caused by intracavity laser fluences up to 10 MW/cm^2 and the deleterious effect on the laser performance of transient medium absorption.

H. T. Powell and B. R. Schleicher, *Lasers Based on Selenium $^1S_0$ Metastable Atoms,* Lawrence Livermore National Laboratory, UCRL-84397 (1980). Prepared for *Journal of Chemical Physics*.

We have investigated the laser performance of the $^1S_0$-$^1D_2$ and $^1S_0$-$^3P_1$ electric-dipole-forbidden transitions of the ground configuration of selenium atoms using 172 nm photolysis of OCSe to produce large concentrations of Se(^{1}S). With complete dissociation of OCSe the Se(^{1}S) atoms are quenched by photoelectrons and Se(^{3}P) atoms, both undesired products of the photolysis. The quenching by electrons is removed and the laser performance is greatly improved by employing small concentrations of SF_6 for electron attachment. At optimized conditions, we have obtained a laser output on both transitions corresponding to 0.3 photons for each OCSe molecule initially in the laser volume. We have also investigated the effects on the lasers of collision-broadening and collision-induced emission and have demonstrated XeSe and KrSe collision-induced lasers operating at wavelengths near the Se($^1S_0$-$^1D_2$) transition.

R. J. Sanchez and R. J. Sherry, *Continuous Mixing and Application for Wet Winding Fiber Composites,* Lawrence Livermore National Laboratory, UCID-18765 (1980).

This report describes a method for mixing and applying matrix during fiber composite winding. The method allows precise control of the fiber-matrix ratio and easy adjustment of the ratio at any time.

Bruce J. Schumacher, *RTNS-II Tritium Scrubber Design and Performance,* Lawrence Livermore National Laboratory, UCRL-83403 (1980). Prepared for the ANS Topical Meeting on Tritium Technology in Fission, Fusion, and Isotopic Applications, Dayton, OH, April 29–May 1, 1980.

The Rotating Target Neutron Source (RTNS-II) at LLNL is an accelerator-based neutron source used for studying radiation damage to materials caused by bombarding a solid metal-tritide target with energetic deuterons to produce fusion neutrons. Deuterium continually displaces tritium from the target at rates which currently go as high as 7 curies/hr. The addition of a second accelerator and increasing the yield of the present accelerator could increase tritium output to 20–30 curies/hr. Since it is not acceptable to release this tritium to the environment, a tritium scrubbing system was devised to clean the vacuum system exhaust before it is vented to the atmosphere. The system has been in continuous operation for over one and one-half years. Tritium released from the facility through the scrubber system is typically less than 1 mCi/day.

R. M. Singleton and J. T. Weir, *Microradiographic Characterization of Metal and Polymer Coated Microspheres,* Lawrence Livermore National Laboratory, UCRL-84471 (1980). Prepared for the 27th Natl. American Vacuum Soc. Symp., Detroit, MI, October 14–17, 1980.

X-ray microradiography is used to make measurements of opaque metal and polymer coatings on hollow glass microspheres which are used as laser fusion targets at Lawrence Livermore National Laboratory. Metal coatings include platinum, tantalum, gold, copper and beryllium where thicknesses range from 1 μm to 10 μm on 70 μm to 200 μm diameter mandrels. Contact film images are made with x-ray energies from 5 keV to 90 keV, depending on the material and geometry. The recorded x-ray images show the internal structure of the coatings which is not observable with optical and SEM techniques. The film images are digitized and directly measured using a small computer-based image analysis system. Wall thicknesses and nonconcentricity can be measured to within 0.3 μm, and diameters to within 1.5 μm. Voids and small spatial defects of the internal structure are also identified.

Gary E. Sommargren, *Optical Heterodyne Profilometry,* Lawrence Livermore National Laboratory, UCRL-84114 (1980). Prepared for *Applied Optics.*

A noncontract optical technique for the measurement of surface profile is described, which has a height sensitivity on the order of one angstrom. It is based on a common path heterodyne interferometer in which two orthogonally polarized beams of slightly different frequency are focused on the surface to be measured. One of the focal points acts as a reference as the other point circularly scans the surface. The phase of the beat frequency of the interfering return beams is directly proportional to the surface height. The results of a surface measurement include graphical displays of the surface profile, autocovariance function, spectral density function, stability, and repeatability. Comparison with other instruments is also discussed.

Irving F. Stowers, *Design and Performance of a High Pressure Spray Cleaning System,* Lawrence Livermore National Laboratory, UCRL-84237 (1980). Prepared for the 5th Intern. Symp. on Contamination Control of ICCCS, Munich, West Germany, September 15–17, 1980.

A very high velocity liquid spray has been previously shown to be an extremely effective method for removing small solid insoluble particles from both polished glass and metallic surfaces. In direct comparisons spraying has been shown to be at least two orders of magnitude more effective than ultrasonic cleaning.

This paper discusses a gloved-box enclosure that has been designed and fabricated to allow this high pressure 7 MPa spray cleaning system to be safely implemented as a routine procedure for cleaning glass-laser hardware. The system includes a recirculation system to allow 90% recovery and reuse of the fluorocarbon solvent. An additional feature is the ability to pass the washing effluent through a membrane filter which after microscopic examination allows verification of cleanliness.

Irving F. Stowers, Howard G. Patton, and Sandra K. Guntrum, *The Need for a Contamination Control Textbook,* Lawrence Livermore National Laboratory, UCRL-84327 (1980). Prepared for the 26th Annual Techn. Meeting of the Inst. of Environmental Sciences, Philadelphia, PA, May 11–14, 1980.

Since the authors have become associated with contamination control technology they have repeatedly found themselves searching for technical information that was either never documented and therefore never reached a technical journal or was too specific to appear in a technical article. On countless occasions they have found other workers frustrated over the same lack of concise and up to date information in the relatively broad and interdisciplinary field of surface science, surface cleaning, and clean room operation and design. It is for these reasons that the authors wish to suggest formally that those engineers, chemists, technicians, and surface scientists working in this field collectively create a textbook that they may use as their first reference and teaching book.

The text of this paper suggests a topical outline for a book and gives examples of the kinds of information that it should contain and the types of questions it should address. Included is an extensive bibliography recently collected showing the diversity of disciplines that those working in contamination control must be knowledgeable of and the variety of publications and journals in which these reports and articles are generally found.

A textbook as proposed could be produced by a committee of authors skilled in each of the necessary disciplines working together under the auspices of the Institute of Environmental Sciences or other sponsoring organization.

J. C. Swingle, L. G. Schlitt, W. R. Rapoport, J. Goldhar, and J. J. Ewing, *An Efficient Narrowband Electron Beam Pumped KrF Laser for Pulse Compression Studies,* Lawrence Livermore National Laboratory, UCRL-84346 (1980). Prepared for the *Journal of Applied Physics.*

A 25 J, 50 ns laser pumped by opposed electron beams is described. Experiments with this device demonstrated a 9 percent intrinsic laser efficiency at power deposition rates of about 1 MW/cm^3. Parasitic control and narrowband output required for Raman compression experiments were demonstrated by injection locking the laser. Experiments showing an angle encoded extraction of the medium (pulse stacking) of a factor of three using a high gain three pass amplifier configuration are also described. The device utilizes triggering schemes of very low jitter suitable for synchronization to other components for optical pulse compression experiments.

Lloyd R. Tripp, *High Pressure Gas Metering Project,* Lawrence Livermore National Laboratory, UCID-18643 (1980).

This paper outlines the initial research and development of a system that uses high pressure helium gas to pressurize vessels over a wide range of pressurization rates, vessel volumes, and maximum test pressures. A method of controlling the mass flow rate in a test vessel has been developed by using the pressure difference across a capillary tube. The mass flow rate is related to the pressurization rate through a real gas equation of state. The resulting mass flow equation is then used in a control algorithm. Plots of two typical pressurization tests run on a manually operated system are included.

D. B. Tuft and M. J. Murphy, *Computer Design of a High Explosive Velocity Augmented Kinetic Energy Penetrator,* Lawrence Livermore National Laboratory, UCRL-83559 (1980). Prepared for the Symp. on Computational Methods in Nonlinear Structural and Solid Mechanics, Washington, D.C., October 6–8, 1980.

The results of a combined analytical experimental design of a high-explosive velocity augmented kinetic energy penetrator are presented. The objective of the analysis is the design of a velocity augmentor and main charge case. The augmentor design must conform to restrictive volume constraints and provide maximum impulse to the main charge which, in turn, must survive the augmentor loading and penetrate the target.

An explicit finite element hydrodynamic computer code, DYNA2D, employing arbitrary zoning, two-way sliding with gaps, and high explosive equation-of-state is employed as the analytical tool. High strain rate material models are used and predictions are compared to experimental deformations. Shock wave interactions in the main charge case are analyzed and a combination of shock attenuation and wave trapping is employed to reduce loads before failure limits.

The final design provides maximum velocity augmentation while staying within volume constraints and maintaining main charge case integrity. Computed deformations and velocities are experimentally verified. This design analysis method using state-of-the-art code and computer capabilities is shown to be an effective method of simplifying the design process as well as providing necessary design optimization data not previously available.

B. W. Weinstein, J. T. Weir, and D. L. Willenborg, *Interferometric Measurements of Multilayer and Double-Shell Inertial Fusion Targets,* Lawrence Livermore National Laboratory, UCRL-84477 (1980). Prepared for the 27th Natl. American Vacuum Soc. Symp., Detroit, MI, October 14–17, 1980.

Optical interference microscopy plays an important role in the measurement of targets for inertial confinement fusion experiments. We describe how these techniques are applied to the measurement of thickness and refractive index of multilayer films on both flat substrates and microsphere targets. We also discuss procedures for manipulating and examining microsphere targets to measure surface defects and wall thickness variations anywhere on the target. Finally, we describe the use of optical interferometry to measure the individual components and final assembled structure of double-shell targets. The accuracy of these measurements is from 0.03 to 0.5 μm, depending on the specific application.

Charles E. Witherell and Terry J. Ramos, *Laser Brazing*, Lawrence Livermore National Laboratory, UCRL-83862 (1980). Prepared for *Welding Journal*.

Conventional brazing frequently involves heating the entire part to the brazing temperature. This requirement prevents the use of this otherwise desirable joining process for parts having integral components of heat-sensitive materials or for very thin sections subject to distortion or attack by the brazing filler metal. This study explored the possibility of using commercial metalworking lasers as a heat source for brazing thin parts, microassemblies with tight dimensional tolerances, and components containing heat-sensitive materials near the braze region. A series of metals and alloys in thicknesses ranging from about 10 mils to 1 mil (0.25 to 0.025 mm) were evaluated in brazing experiments using standard filler metals. Most filler metals were in the form of alloy powders; a few were used as preplaced foils. Laser brazing was found to be a practical and effective method for producing high integrity joints in a wide variety of metals and alloys in thin sections. Rapid solidification, characteristic of the process, produces hardness increases in the deposits which, for some compositions, can approach those of splat-cooled glassy metals. This offers the possibility of significant increases in brazed joint strength.

R. L. Woerner, V. F. Draper, J. C. Koo, and C. D. Hendricks, *Fabrication of Glass Spheres for Laser Fusion Targets*, Lawrence Livermore National Laboratory, UCRL-83395 (1980). Prepared for the Topical Meeting on Inertial Confinement Fusion, San Diego, CA, February 26–28, 1980.

We have developed processes for mass producing the quality glass microspheres required for current laser fusion experiments. We describe the advances in the methods and materials used in our liquid droplet and dried gel systems.

G. Yanes, *TRAAP: A Computer Program for Acquisition and Analysis of Data from a Transient-Measurement System*, Lawrence Livermore National Laboratory, UCRL-52936 (1980).

TRAAP is a computer program that records, analyzes, and plots data gathered by a transient recorder. It controls data acquisition by allowing the user to check the transient recorder before taking data and offering the choice of using or not using a low-pass filter. It transfers data to and from floppy disks for storage and playback. It analyzes data in a variety of ways (including compressing, smoothing, simple mathematical operations, differentiating, integrating) and provides four options for graphic output. TRAAP is a flexible program whose capabilities can readily be increased, several new options are currently being developed.

George Yanes, *Pneumatic Controls for an LLL Hydrostatic Test Facility*, Lawrence Livermore National Laboratory, UCRL-52913 (1980).

Pneumatic controls were installed on the high-pressure valving system for one of LLL's hydrostatic test facilities. Pneumatic controls were used because they can be programmed to perform selected functions by remote control and do not introduce electrical interference into the acoustic-emission instrumentation used to monitor a test. The pneumatically controlled valving system is relatively simple to operate. It eliminates hazards to the operator and is fail-safe if control air pressure is lost. Circuit and component descriptions, plus photographs of the system, are included in this report.

RMD

U. S. Government Printing Office: 1981/4–789-002/5565